ALMA MATER STUDIORUM - UNIVERSITÀ DI BOLOGNA

Depertment of Physics and Astronomy "Agusto Righi"

Master Degree Thesis in Astrophysics and Cosmology

The 2-point correlation function in alternative dark matter model

---

Thesis Supervisor
Prof. Federico Marulli

Co-supervisor
Prof. Giulia Despali

Candidate
Shirshendu Sekhar Mondal

Academic Year 2024/25

Acknowledgement

I begin by offering my deepest gratitude to the universe itself, a fitting homage for a thesis rooted in cosmic evolution. This journey, filled with equations, simulations, long nights of code, and an occasional glimpse of the stars, has been as humbling as it has been exhilarating. Every challenge I encountered—whether a bug in the model or a conceptual paradox—taught me perseverance, patience, and precision. This thesis, while a scientific endeavor, became a personal voyage through the vast unknown, much like the universe it attempts to explore.

I would like to express my heartfelt appreciation to my supervisor, **Professor Federico Marulli**, and my co-supervisor, **Professor Giulia Despali**, for their unwavering guidance. Working under their mentorship in the field of astrophysics has been a long-cherished goal of mine. **Professor Marulli**'s course on **Advanced Cosmology** was not only enlightening but also deeply inspiring. It was during this course that my interest in large-scale cosmological simulations and dark matter physics took root, and it only grew deeper through my involvement in their research group. Their support has been instrumental throughout this thesis, whether it was helping refine the statistical analysis of two-point correlation function profiles, or patiently guiding me through the complexities of baryonic and dark matter feedback. They offered not just critique but clarity, not just knowledge but wisdom. I am deeply thankful for their intellectual generosity and the space they gave me to grow into a more confident researcher.

I would also like to thank **Dr. Massimiliano Romanello** from the Department of Physics and Astronomy (DIFA), whose insights on hydrodynamic effects and dark matter modeling sharpened my understanding and significantly enhanced the rigor of this work. Their belief in my capabilities often kept me going, especially when I doubted myself amidst the vast datasets and endless model iterations. To my parents—my unwavering constants, thank you for your love, which spanned not just distances but time zones and mental spaces. Your belief in me, even when I struggled to believe in myself, made this journey possible.

To my partner, **Kaushani Dey**, thank you for grounding me when I got lost in Universe and code. Your kindness, patience, and calming presence were my refuge. For being there during the halos and subhalos of frustration and celebrating each small cosmic discovery, I owe you everything.

To my closest friends, scattered across observatories and countries, thank you. Your late-night discussions, coding help, laughter, and memes brought light into even the darkest simulations. Special thanks to **Abhra Saha**, **Shagnik Chaudhuri**, **Priyanka Saha**, **Matteo Santini**, and **Fabio Orticoni** - for proofreading, sanity checks, and feeding me real food when I forgot to eat. You know who you are.

I would also like to thank my company **Datalogic s.r.l** for staying always beside me, es-

pecially my manager, **Olivier Di Gennaro**, for handling all my requests and tolerating my mistakes.
To those who mentored me informally along the way, thank you for nudging me back on track when I strayed, for your quiet encouragement, and for believing in the scientific spirit within me. And finally, to the clusters of galaxies—both real and metaphorical. This thesis is my small attempt to understand your silent brilliance. I close, as I began, with gratitude.

Abstract

The formation and evolution of cosmic structures are governed by the interplay of dark matter, baryonic physics, and the underlying geometry of the Universe. This thesis focuses on the statistical characterization of large-scale structure through the measurement of the 2-point correlation function (2PCF) applied to dark matter halo distributions derived from high-resolution cosmological simulations. In particular, we analyze simulations from the *IllustrisTNG* project [38]—including TNG100-1, TNG100-1-Dark, TNG300-1, and TNG300-1-Dark—and a dedicated warm dark matter (WDM) simulation to understand the differences in clustering patterns induced by baryonic processes and dark matter particle properties.

We utilize the `CosmoBolognaLib` [34] to compute the 2PCF in both real and redshift space. This C++ library allows efficient handling of large cosmological datasets and includes support for theoretical predictions of 2PCF and halo bias models. The `Catalogue` and `Measure` classes of the library enable fine control over object properties and statistical measurements, making it particularly suitable for our multi-resolution dataset spanning a wide dynamic range in mass and redshift.

To ensure accurate large-scale clustering measurements, we correct for the finite-volume effects by applying the integral constraint correction, especially critical for the smaller TNG100-1 boxes. We find that more massive halos exhibit stronger clustering and are preferentially located in these dense environments, while lower-mass halos remain more uniformly distributed. The comparison between hydro and dark-matter-only runs reveals that baryonic physics significantly enhances clustering in overdense regions (filaments and nodes of the cosmic web), as confirmed by both 3D visualizations of halo positions and 2PCF profiles.

The study extends to WDM simulations, which demonstrate a marked suppression of low-mass subhalo formation due to the free-streaming length of WDM particles. Nevertheless, surviving halos in WDM runs are more clustered on small scales, echoing the scale-dependent suppression of structure. The 2PCF profiles in WDM differ notably from CDM counterparts, showing lower amplitude at small separations and stronger residuals when fitted with linear bias models. This supports the notion that WDM cosmologies yield less small-scale structure, but denser filamentary configurations.

These results underscore the need to refine theoretical models, particularly in the non-linear regime, where baryonic feedback, star formation, and hydrodynamical effects introduce significant deviations from linear predictions. Our residual analysis identifies substantial discrepancies at both small ($r < 1$ Mpc/h) and large ($r > 30$ Mpc/h) scales. On small scales, deviations are attributed to unmodeled baryonic processes; on large

scales, they arise from box-size limitations and periodic boundary conditions inherent in the simulations.

Overall, this work contributes to the growing body of literature that leverages cosmological simulations to improve the accuracy of large-scale structure observables. The findings are crucial for interpreting future data from galaxy redshift surveys such as *Euclid* and *DESI*, which aim to constrain the nature of dark matter and dark energy. Future directions include incorporating machine learning techniques for bias modeling, expanding to larger simulation volumes, and exploring higher-order statistics such as the 3-point correlation function to capture non-Gaussian features of the cosmic web.

Contents

Chapter 1

1 Introduction

1.1 History of our Universe

According to our current understanding, the journey of our Universe started with the Big Bang nearly 13.7 billion years ago. In that time, our Universe was an infinitely compressed dense state, called initial singularity. After this the Universe is expected to have experienced an accelerated expansion phase, what we called inflation. During the inflation era, the energy density fluctuations in the inflation field provided the primordial seeds the formation of the cosmic structures. The time scale for this era is estimated to be around 10^{-36} to 10^{-32} seconds after the big bang. Soon after this, radiation-dominated era started, when the Universe was dominated by relativistic particles.

By the time passed, the Universe continued to expand and the plasma started to cool down which finally allowed the production of light elements. We call this process Nucleosynthesis and it took place after 3 to 20 minutes from the Big Bang. During this phase, the Universe was enough cooled for protons and neutrons to be combined and form the nuclei of elements like H, He, Li.

After 50-70 thousand years from Big Bang, the matter-radiation equality era started which leads the Universe dominated by the matter. At that point, the energy density fluctuations grow by gravitational attraction of the surrounding matter to the denser regions, and these regions were responsible for the large structure of our Universe now a days.

Until 380 000 years from the Big Bang, the cosmic plasma was hot enough to keep the photons in the thermal equilibrium and that's why during this time, the Universe was opaque. After all these, there were last scattering of photons and produced the very first light that we are able to see today, which we call Cosmic Microwave Background radiation (CMB).

1.2 Primordial fluctuations

Inflation gives us a mechanism that generates the primordial perturbations specially, the density perturbations were generated during the inflation through the quantum fluctuations of the inflation filed. This guarantees that they were intrinsically random (stochas-

tic) and quasi-Gaussian. So, in order to describe them, we need a statistical approach, considering the so called primordial power spectrum. We can infer the latter with the help of CMB temperature anisotropies and polarization as well through large scale structure probes [3].

The scalar perturbations indeed provide the dominant contribution to the anisotropies observed in the CMB and they are responsible for the large scale distribution of the galaxies.

The inflationary era is a phase of rapid exponential expansion of the early Universe. As said the variation of the density of matter happened due to the quantum fluctuations. Initially the fluctuations for the dark matter density were small, but with the time, overdense regions experienced strong gravitational attraction leads to pull in more matter. This gravitational instability leads to the growth of structures from small density fluctuations. Now, we are in the matter dominated era and this time we can have the formation of cosmic structures because the radiation pressure is no more dominant. The fluctuations lead to a process called hierarchical clustering where the small dark matter halos merged together and formed larger and larger halos. These halos are dense and were formed in very early time, acting as gravitational attractors, pulling in additional dark matter which influenced the distribution of both dark and visible matter. The growth of fluctuations formed the cosmic web which is a complex network of filaments, voids and galaxy clusters. This is the large-scale distribution of dark matter in our universe. Galaxies and galaxy clusters formed in those regions where we have higher dark matter densities. Initial fluctuations in dark matter density set the size and properties of the halos.

1.3 Evidence for dark matter

1.3.1 Rotational curves and early time detection methods

The Newtonian laws of motion and gravity theory were presented in Isaac Newton's 1687 treatise Philosophiae Naturalis Principia Mathematica [39]. By doing this, Newton gave people the means to find invisible or unseen objects by using their gravitational pull on other bodies. An incredible example dates back to 1846, when Urbain Le Verrier and John Couch Adams, two French and English astronomers, postulated [27] the existence of an invisible planet to account for Uranus' unusual orbit. In fact, after receiving a letter with directions on where to search, their German colleague John Galle was able to find the planet of Neptune that very night. As an aside, Urbain Le Verrier noticed an abnormality in Mercury's orbit and incorrectly claimed that there could be another planet that is not observable. This strangeness was ultimately explained by Einstein's

general theory of relativity [13].

Knut Lundmark, a Swedish scholar, investigated the rotational velocities of five galaxies in 1930 and concluded that the mass required for maintaining the galaxies' stability was significantly larger than the visible matter. The five galaxies' estimated mass-to-light ratios ranged from 6 to 100 times the solar neighborhood's observed ratio [32]. Unfortunately, most people forget regarding Lundmark's findings. Studies of the Coma galaxy cluster carried out in 1933 by Swiss astronomer Fritz Zwicky have been recognized as the first proof for dark matter. He detected a very high mass-to-light ratio, nearly 100 times that of the solar neighbourhood, using the virial theorem, which relates the radius and velocity dispersion of a gravitationally bound cluster of objects to the cluster's total mass [63][64] . A fascinating fact is that Zwicky calculated the distance to the Coma cluster using the Hubble constant. At the time, the Hubble constant was over-estimated by almost an order of magnitude, which also inflated the estimated mass-to-light ratio by the same factor. Even after this modification, a significant proportion of non-luminous materials is still present.

Vera Rubin performed deeper measurements of spiral galaxy rotational velocities and the correlation between rotational velocity and galactocentric radius in the 1970s [56]. In a spiral galaxy, the disk's rotating velocity should decrease with distance from the galactic centre if the amount of visible baryonic matter is the sole factor under consideration. A further finding by Rubin was that the rotational velocity approaches a roughly constant value as one gets further apart from the galactic centre, suggesting that there is a significant amount of non-luminous matter in the outer regions of galaxies. This is shown in Figure 1.1. Other astronomers also verified and expanded on this remarkable. According to current knowledge, a spiral galaxy's star disc is encased in a bigger, spherically dispersed dark matter halo.

These kinds of dynamical observations continue to be among the and convincing arguments in favor of non-collisional dark matter. Similarly, satellite probes like the globular cluster can be used to estimate the dynamical mass of spiral galaxies or spheroidal dwarf galaxies in order to determine the mass distribution and gravitational potential. Today we have solid evidence that much of the matter in the Universe is dark, not just in the sense that it is non-luminous, but also that it is non-baryonic. Only because of its gravitational effects do we still know about dark matter. Nevertheless, evidence for dark matter can be found throughout a wide variety of distance scales, from the cosmic to the sub-galactic.

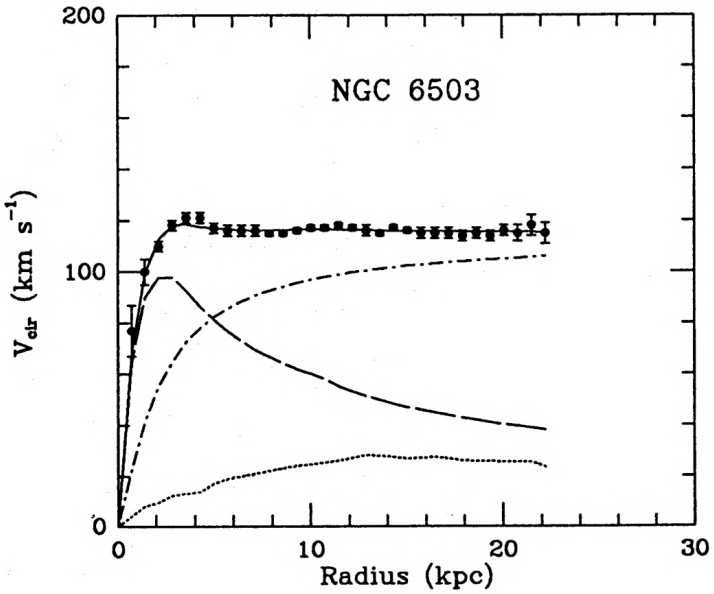

Figure 1.1: Rotational velocity as a function of distance from the galactic centre, for spiral galaxy NGC6503. The dots represent the measured data, while the lines are contributions from gas, stellar disk, and halo dark matter. The figure is taken from Begeman et al. [5].

1.3.2 Gravitational lensing

Gravitational lensing is another method of determining a galaxy's or galaxy cluster's mass. According to Einstein's general theory of relativity, light gets bent as it passes through a gravitational field. The foreground galaxy will function as a lens to bend the light from the background galaxy if two galaxies are close to the same line of sight. The mass of the foreground galaxy can be linked to the lens's strength based on the distance to the two objects.

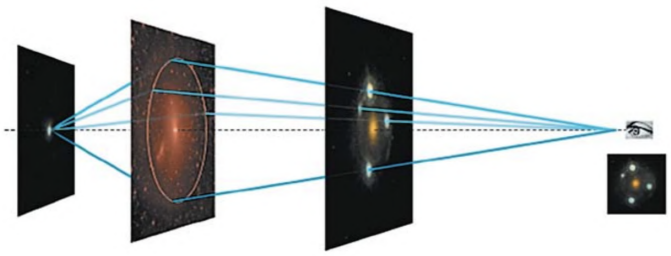

Figure 1.2: **Lensing of multiply imaged sources.** [36]
A distant background source (far left) emits light that is bent by a foreground dark matter halo and galaxy (center panels), acting as a gravitational lens. The observer (far right) sees multiple images of the background source (inset), often forming an Einstein Cross configuration due to this lensing effect.

Distant objects can be gravitationally lensed into multiple (two or four) images. The

light path for each of these images may be microlensed by stars or another heavy object (depends upon the size of the source galaxy) in the lens galaxy. This can be detected by independent variation in the light curve of the images once the time delay between them has been subtracted.

1.3.3 X-ray emission and CMB

By examining the X-ray emissions from a galaxy cluster's intergalactic gas, one can also determine the cluster's mass. A superheated plasma that produces X-rays is created when intergalactic gas aggregates in a galaxy cluster's deep gravitational well. This gas's temperature is determined by the total kinetic energy it gains as it descends into the cluster's gravitational well, which serves as a mass probe.

In support of non-collisional dark matter, the Bullet Cluster and other such systems provide compelling evidence. Two distinct galaxy clusters that have collided and gone through one another make up the Bullet Cluster, which is seen in Figure 1.3. The cosmic gas has been slowed down and heated up, releasing an observable flux of X-rays, while the bright galaxies have proceeded on their paths unhindered. Weak gravitational lensing is used to map the system's mass distribution, showing that the brilliant galaxies are surrounded by a diffuse matter distribution. Given that the diffuse matter distribution has collided and is passing through without interacting, this is compelling evidence for non-collisional dark matter.

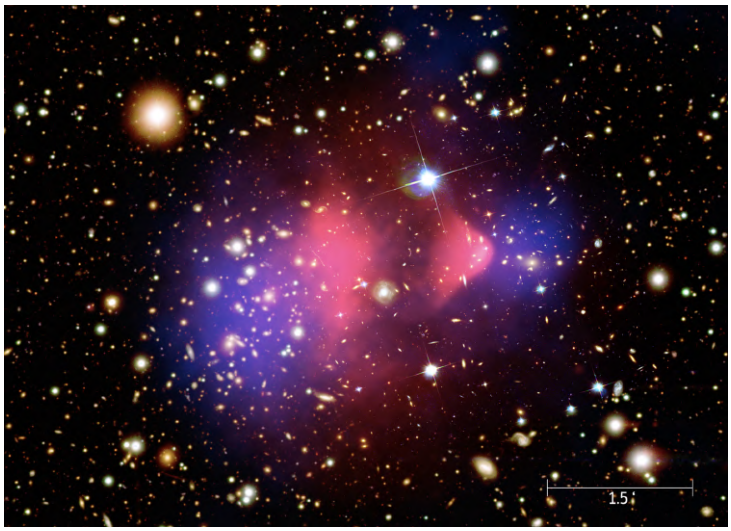

Figure 1.3: The Bullet Cluster, in optical (yellow) and X-ray light (pink), and mass distribution inferred from weak lensing (blue). Image Credit: X-ray: NASA/CXC/M.Markevitch et al. [33] Optical: NASA/STScI; Magellan/U.Arizona/D.Clowe et al. [8] Lensing Map: NASA/STScI; ESO WFI; Magellan/U.Arizona/D.Clowe et al. [8].

The cosmic microwave background radiation, (CMB) is a very useful indicator of the makeup of the Universe at the cosmological scale. The CMB is a relic of the primordial plasma's 380 000-year-old age, when free protons and electrons bonded to create atoms with a neutral charge. The CMB was the Universe's final scattering surface after this phase shift, which made the Universe transparent. With a current temperature of 2.726 K, the CMB is quite near to a perfect black body spectrum. Temperature anisotropies of order 10^{-5} K are examples of its minor departures from a perfect black body. Measurements of these temperature variations, which are shown in Figure 1.4, have been made by the Planck Satellite, and previously by the Wilkinson Microwave Anisotropy Probe (WMAP) [26], and the Cosmic Background Explorer (COBE) [6]. Figure 1.5 displays the CMB power spectrum in spherical harmonics that quantified these anisotropies. Primordial density variations and the medium through which they have spread combine to form the power spectrum's structure. A review of CMB cosmology may be found, for instance, in Weinberg's Cosmology textbook [35] or a review by Samtleben et al.[57].

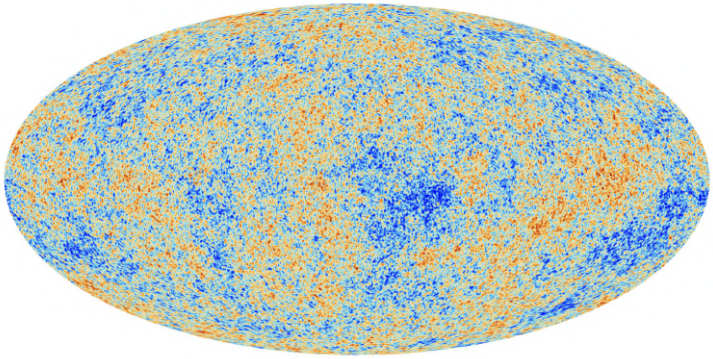

Figure 1.4: Temperature fluctuations of the CMB, as measured by the Planck satellite, seen in a Mollweide projection of the sky. Orange (blue) regions correspond to high (low) temperatures. Image credit: ESA and the Planck Collaboration link.

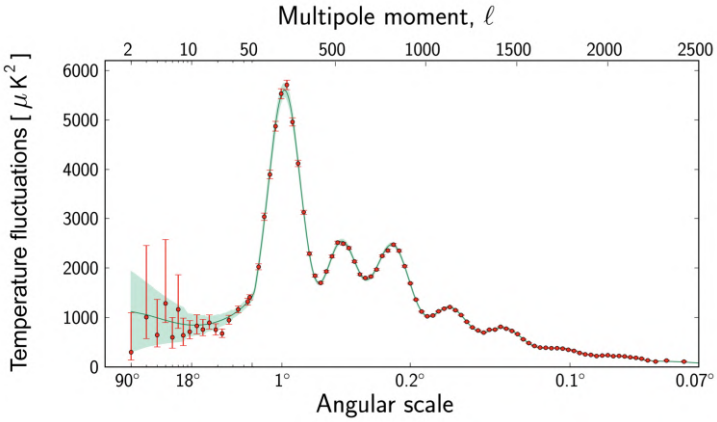

Figure 1.5: Power spectrum of the CMB, as measured by the Planck satellite. Image credit: ESA and the Planck Collaboration link.

The Λ- cold dark matter model (ΛCDM) is the dominant cosmological framework, with Λ standing for the cosmological constant. The amount of dark matter is one of the six free parameters in this model. The CMB and its anisotropies, the abundance of light elements (such as lithium, helium, and hydrogen), and the Universe's accelerated expansion are all well described by the CDM model. The dominating dark matter component of the CMB, which makes up around 85 percent of all matter, interacts with baryonic matter either extremely weakly or not at all.

Moreover, dark matter drives the Universe's large-scale structure development, in which mass collapses to create galaxies and galaxy clusters. Galaxy formation would be delayed if radiation did not wipe off tiny density perturbations of the baryonic matter caused by the gravitational collapse of cold dark matter. The ΛCDM model and the dark matter paradigm are further supported by detailed large-scale structure n-body simulations, including the ones used in this thesis work, which overall agree with observations.

Chapter 2

2 Cosmology

This chapter offers a broad introduction to the core elements of the standard cosmological model, providing insight into the essential aspects of this distinct branch of physical science. Cosmology, an age-old field, explores the origin and development of the entire Universe. It aims to interpret the Universe's large-scale matter distribution by applying physical principles and drawing on its long-standing tradition of investigating the Universe's beginnings, its current appearance, and its future evolution.

2.1 The Axioms

Cosmology initially emerged as a branch of natural philosophy, but began its transformation into a physical science in 1917 with Albert Einstein's formulation of general relativity. The field relies on constructing models backed by observational data, with general relativity serving as a fundamental axiomatic framework that forms the basis for models with minimal free parameters. However, General Relativity alone is not sufficient; it must be supplemented by the assumptions of isotropy and homogeneity, which constitute the so-called Cosmological Principle. This symmetry principle plays a crucial role in simplifying cosmological models by reducing their degrees of freedom. The principle of isotropy states that the Universe appears the same in all directions, aligning closely with the Copernican Principle, which posits that no specific location holds a privileged observational standpoint. When combined, these principles lead to the concept of homogeneity, meaning that the Universe's structural properties remain consistent across different regions. However, the requirements set by the Cosmological Principle are not always strictly met. Observations in any direction reveal inhomogeneities, such as planets, stars, galaxies, and galaxy clusters. This highlights a crucial aspect of the Cosmological Principle: it applies only when averaging over large scales (approximately beyond 185 Mpc [37]) and pertains to averaged properties).

Evidence from studies of the large-scale structure (to be defined the first time) and the CMB supports this characterization, which is assumed to extend beyond the observable Universe. However, unlike fundamental principles in physics—such as Heisenberg's uncertainty principle in quantum mechanics—the Cosmological Principle is not an intrinsic requirement of the theory [41]. Instead, it serves as a simplifying assumption for constructing cosmological models on vast scales.

2.1.1 General relativity

General relativity describes gravity as the intrinsic curvature of spacetime, expanding upon the Newtonian understanding of gravity. Developed by Albert Einstein in 1915, this theory interprets gravitational interactions as geometric properties of a 4-dimensional manifold.

A manifold is a mathematical structure that locally resembles as $\mathbb{R}^4$, meaning that in the vicinity of any given point, coordinates can be assigned similarly to those in 4-dimensional Euclidean space. This local coordinate system allows for mathematical calculations, while the topological properties of the manifold ensure the continuity of functions and the convergence of series across it. The shape of a manifold can vary—it may be curved, and its intrinsic geometry may differ from the familiar flat Euclidean space.

A key tool for describing the geometry of a manifold is the metric, which is formally defined as a symmetric, non-degenerate (0,2)-tensor. This tensor functions as a bilinear map from the manifold's tangent bundle to the real numbers $\mathbb{R}$, encoding the manifold's geometric properties and determining the length of curves. When a manifold is equipped with a metric, it is referred to as a metric manifold. The length of an infinitesimal curve element relates to the metric through the following expression (in Cartesian coordinates):

$$ds^2 = g_{\mu\nu} dx^\mu dx^\nu \tag{2.1}$$

In this context, ds^2 represents the squared length of an infinitesimal line element, where $g_{\mu\nu}$ are the components of the metric tensor, and dx^μ and dx^ν denote the coordinate differentials between two endpoints of a curve segment. Throughout this text, Greek indices will range from 0 to 3, with $\mu = 0$ corresponding to the time component and $\mu = 1, 2, 3$ representing the spatial components.

The geometry of a manifold is fundamentally determined by the metric field g, but how can we distinguish whether the manifold is flat or curved? To address this question, we introduce a key mathematical tool in differential geometry used to characterize the curvature of manifolds: the Riemann curvature tensor:

$$R^\alpha_{\mu\nu\rho} = \partial_\nu \Gamma^\alpha_{\mu\rho} - \partial_\rho \Gamma^\alpha_{\mu\nu} + \Gamma^\alpha_{\nu\beta}\Gamma^\beta_{\mu\rho} + \Gamma^\alpha_{\rho\beta}\Gamma^\beta_{\mu\nu} \tag{2.2}$$

The Riemann curvature tensor provides as a criterion for determining the flatness of a manifold. If $R^\sigma_{\mu\nu\rho} = 0$ everywhere, the manifold is flat, regardless of the chosen coordinate system.

In this context, we use the notation $\partial_\mu = \partial/\partial x^\mu$ to represent partial derivatives. The components of the Levi-Civita connection, denoted as $\Gamma^\alpha_{\mu\nu}$, are defined as follows:

$$\Gamma^{\alpha}_{\mu\nu} = \frac{1}{2} g^{\alpha\beta}(\partial_\mu g_{\nu\beta} + \partial_\nu g_{\mu\beta} + \partial_\beta g_{\mu\nu}) \tag{2.3}$$

The Levi-Civita connection is intrinsically linked to the metric and can be understood in two complementary ways: as a geometric feature of spacetime or as a manifestation of gravitational forces influencing the motion of objects. It defines how vectors change as they move along a manifold and ensures that parallel transport preserves the inner product, maintaining the structure of spacetime.

The contraction over one pair of indices in Eq.(2.2) results in the Ricci's tensor:

$$R_{\mu\nu} = \partial_\alpha \Gamma^{\alpha}_{\mu\nu} - \partial_\nu \Gamma^{\alpha}_{\mu\alpha} + \Gamma^{\beta}_{\mu\nu}\Gamma^{\alpha}_{\beta\alpha} - \Gamma^{\beta}_{\mu\alpha}\Gamma^{\alpha}_{\beta\nu} \tag{2.4}$$

At the core of general relativity lie the Einstein's field equations, which can be derived from the least action principle applied to the Einstein-Hilbert action. These equations, in natural units, take the form:

$$R_{\mu\nu} - \frac{1}{2} g_{\mu\nu} R = 8\pi G T_{\mu\nu}, \tag{2.5}$$

where $R_{\mu\nu}$ is the Ricci curvature tensor, R is the Ricci scalar, G is the gravitational constant and $T_{\mu\nu}$ is the stress-energy tensor representing the energy content of the Universe. This set of equations encapsulates the fundamental relationship between the intrinsic geometry of spacetime, encoded in the metric tensor, and the energy (matter) content that influences this geometry.

2.1.2 Friedmann-Lemaître-Robertson-Walker metric

In cosmology, choosing an appropriate metric $g_{\mu\nu}$ is essential for accurately defining distances between events in spacetime. By applying Einstein's summation convention, which requires summing over repeated indices, we can express Eq. (2.1) in a more explicit form, revealing three distinct contributions:

$$ds^2 = g_{00}dt^2 + 2g_{0i}dtdx^i + g_{ij}dx^i dx^j \tag{2.6}$$

Here, the indices i and j represent spatial components and range from 1 to 3. Throughout this work, we adopt the metric signature convention (-,+,+,+), where the negative sign corresponds to the time component, while the positive signs are associated with the spatial components. Based on the sign of ds^2 , we can categorize spacetime intervals into three distinct types:

- $ds^2 < 0$: time-like (trajectories of massive particles)
- $ds^2 = 0$: light-like (geodesics of photons)

- $ds^2 > 0$: space-like (separated events cannot influence each other)

The Cosmological Principle can be formalized by assuming the existence of six killing vectors, three for spatial rotations (isotropy) and three for spatial translation (homogeneity), describing the spatial symmetry between spacetime intervals and guaranteeing that the mixed term $2g_{0i}dtdx^i$ in Eq.(2.1) vanishes. For a flat manifold, the metric simplifies to

$$ds^2 = -dt^2 + dl^2 \tag{2.7}$$

where $dl^2 = g_{ij}dx^i dx^j$ is the spatial distance between two points. Moving beyond flat space, consider a homogeneous and isotropic unit 3D sphere which is a geometric object that can be embedded in 4-dimensional spacetime, constructed by gluing the boundaries of two 2D spheres. In Cartesian coordinates, the squared distance element is:

$$dl^2 = dx^2 + dy^2 + dz^2 + du^2 \tag{2.8}$$

We can express dl^2 in polar coordinates and it takes the form

$$dl^2 = \frac{dr^2}{1-r^2} + r^2 d\Omega^2 = \frac{dr^2}{1-r^2} + r^2(d\theta^2 + sin^2\theta d\phi^2) \tag{2.9}$$

A 3d sphere with radius a may be easily generalised to this conclusion by adding the radius length as scaling to the formula. These spaces have a positive curvature, but we might also talk about spaces that have a negative curvature, such as a 3D hyperboloid.

The most general metric satisfying the Cosmological Principle is the Friedmann-Lemaître-Robertson-Walker (FLRW) metric:

$$ds^2 = -dt^2 + a(t)^2[\frac{dr^2}{1-kr^2} + r^2(d\theta^2 + sin^2\theta d\phi^2)] \tag{2.10}$$

Here:

- (r, θ, ϕ) are the comoving polar coordinates.
- t is the proper time (or cosmic time) measured by observers at rest with respect to the comoving coordinates.
- $a(t)$ is the scale factor, which accounts for the expansion of the Universe over time.
- k is the curvature parameter, which can take three possible values (-1, 0, +1), corresponding to a Universe with negative, zero, or positive curvature, respectively.

2.1.3 Expansion of our Universe

Different definitions of distance are used in cosmology to describe the separations between events or objects. The proper distance, or the distance between two events that occur at

the same cosmic time (i.e., when $dt = 0$), is one basic option. The instantaneous spatial separation between two points at a specific point in time is provided by this metric.
To derive the proper distance, we start with the general metric expressed along a specific line of sight, where the angular components vanish ($d\theta = 0$ and $d\phi = 0$):

$$d_{pr}(t) = \int_0^r \frac{dr'^2 a(t)}{\sqrt{1 - kr'^2}} = a(t)F(r) \tag{2.11}$$

$F(r)$ is a function that accounts for the spatial part of the FLRW metric

$$F(r) = \int_0^r \frac{dr'^2}{\sqrt{1 - kr'^2}} = a(t)F(r) \tag{2.12}$$

Depending on the Universe's geometry, it can take on many shapes. Specifically, if:

- $k = 0 \rightarrow F(r) = r$
- $k = +1 \rightarrow F(r) = arcsin(r)$
- $k = -1 \rightarrow F(r) = arcsinh(r)$

There is a temporal dependence on the ideal distance. The appropriate distance is known as the comoving distance if we set the time to the current time, t_0:

$$d_C = d_{pr}(t_0) = a(t_0)F(r) = \frac{a(t_0)}{a(t)} d_{pr}(t_0). \tag{2.13}$$

An equation for the radial velocity may be found by deriving the correct distance with respect to t since it is dependent on time:

$$V_r(t) = \frac{d[d_{pr}(t)]}{dt} = \frac{d[a(t)F]}{dt} = \frac{a'}{a} aF = \frac{a'}{a} d_{pr} \tag{2.14}$$

This is the Hubble-Lemaître law, which explains how an object's radial velocity changes as a result of the Universe's expansion. The Hubble parameter, or $H = \dot{a}/a$, encodes all of the data on the Universe's expansion.

The assessment of the Hubble parameter at the current time t_0 is still an uncertain subject [50]. The Hubble constant was can be determined by both direct observations, such as Cepheids and Type Ia supernovae, and indirect measurements from anisotropies in the CMB. There is a Hubble tension of almost 10 percent in the most recent estimates, which are $H_0 = 67.4$ km s^{-1} Mpc^{-1} from CMB observations [49] and $H_0 = 74$ km s^{-1} Mpc^{-1} from local standard candles [54].

The presence of a unique location as the expansion's center is not allowed by Eq.(2.14). Let us consider an observer determining a galaxy's location l and velocity V, assuming a non-relativistic regime ($v \ll c$), to see why this is not the case. The recession law, which is derived from the Hubble-Lemaître law at the current time t_0, expresses the

relationship between these two values as follows: $v = H_0 l$. Now, let us look at an additional observer who is at position l'. In comparison to the first observer, this one will have velocity $v' = H_0 l'$. Using the non-relativistic composition law, the second observer's measurement of the galaxy's velocity is

$$\vec{V} = \vec{v} - \vec{v}' = H_0(\vec{l} - \vec{l}') = H_0 \vec{L}, \tag{2.15}$$

where $\vec{L}$ denotes the position of the galaxy relative to the second observed. This demonstrates how, in accordance with the Cosmological Principle, the linearity requirement ensures that Hubble's law is true for all comoving observers.

Eq. (2.5) contains other physical constants besides the gravitational constant G. The cosmological constant Λ also adds to the Universe's energy content in the conventional cosmological framework. This constant was first introduced to stop the Universe's dynamical behavior of constant expansion or contraction in Einstein's field equations. The cosmological constant was understood to act as a stabilizer in this way, but indeed the equilibrium is essentially unstable. However, it has latter re-introduced to provide a new energy source, known as dark energy.In future the laws of gravity instead if it were discovered that this constant alone is insufficient to explain the observed acceleration.

According to the Hubble-Lemaître law Eq. (2.14), the Universe does in fact exhibit dynamical properties, most notably its expansion. In the recent times, this growth has started to accelerate rather than occurring at a steady speed. There are several pieces of evidence: Type Ia supernovae [51], [44], and baryonic acoustic oscillations [14] being the most robust ones [24], [20],[6]. Important new information regarding the nature of dark energy has been revealed by other studies that have investigated variations in the CMB radiation, such as those carried out with the Planck spacecraft [48].

In conclusion, although the Hubble-Lemaître law provides a clear understanding of the connection between galaxies' distance and recessional velocity, the existence of the cosmological constant prompts us to consider a constantly changing Universe in which the acceleration of growth is still an unsolved conundrum.

2.1.4 Cosmological redshift

Let us consider a photon that was released at time t_{em} from an astronomical source at a given. An observer notices this photon at the moment t_{obs}. Using the metric given by Eq. (2.11), aligning the line of sight so that $d\theta = d\phi = 0$ and keeping in mind that photons always follow:

$$dt^2 = a^2(t)\frac{dr^2}{1 - kr^2} \tag{2.16}$$

.

If we integrate this equation from t_{em} to t_{obs}, we get:

$$\int_{t_{em}}^{t_{obs}} \frac{dt}{a(t)} = \int_0^r \frac{dr'}{\sqrt{1-kr^2}} \tag{2.17}$$

Let us now assume that another photon is released by the astrophysical source at time $t_{em} + \delta t_{em}$. The observer will perceive this second photon at time $t_0 + \delta t_0$, and if the two photons travel the same distance t, then

$$\int_{t_{em}}^{t_{obs}} \frac{dt}{a(t)} = F(r) = \int_{t_{em}+\delta t_{em}}^{t_{obs}+\delta t_{obs}} \frac{dt}{a(t)} \tag{2.18}$$

.

This gives us:

$$\frac{\delta t_{obs}}{a(t_{obs})} = \frac{\delta t_{em}}{t_{em}} \tag{2.19}$$

.

The above equation gives us both:

- frequency

$$a(t_{obs})\nu_{obs} = a(t_{em})\nu_{em} \tag{2.20}$$

- wavelength

$$\frac{\lambda_{obs}}{\lambda_{em}} = \frac{a(t_{obs})}{a(t_{em})} \tag{2.21}$$

These formulas show that the change in the scale factor a is reflected in the photon's measured wavelength (or frequency). We may construct a function that expands linearly with $a(t)$ back in time, serving as a stand-in for the Universe's expansion. This is the **Cosmological Redshift**:

$$z = \frac{\lambda_{obs} - \lambda_{em}}{\lambda_{em}} = \frac{\Delta\lambda}{\lambda} \tag{2.22}$$

By setting the observed time to t_0 as reference, we find a linear relation between the redshift and the scale factor

$$1 + z = \frac{a(t_0)}{a(t)} \tag{2.23}$$

At then present time, $t = t_0$ and so $z = 0$. Since $a(t_0) > a(t)$ for $t > t_0$, observations indicate that the scale factor is monotonic and has been growing up to the present day, it follows that $z(t_0) < z(t)$.

2.2 Friedmann models

As already mentioned in order to explain the late-time rapid expansion of the Universe, a positive cosmological constant has lately been incorporated into Einstein's equations. Consequently, the effective stress-energy tensor may be used in place of the stress-energy tensor in Eq. (2.5), compensating for an extra term.

$$\tilde{T}_{\mu\nu\mu\nu} + \frac{\Lambda}{8\pi G} g_{\mu\nu} \tag{2.24}$$

By treating the universe as an ideal fluid and ignoring thermal conduction and viscosity, Friedmann models allow the stress-energy tensor to be stated only in terms of the fluid's pressure p and energy density ρ:

$$T^{\mu\nu} = -pg^{\mu\nu} + (p + \rho)u^{\mu}u^{\nu} \tag{2.25}$$

where u^{μ} and u^{ν} are the fluid's 4-velocity vector components. The stress-energy tensor simplifies to a diagonal matrix when anisotropic stress is absent:

$$T^{\mu}_{\nu} = \begin{pmatrix} -\rho & 0 & 0 & 0 \\ 0 & p & 0 & 0 \\ 0 & 0 & p & 0 \\ 0 & 0 & 0 & p \end{pmatrix} \tag{2.26}$$

.

Because of the different combinations of indices μ and ν, Eq.(2.5) has 16 equations. However, this number decreases to 10 independent components because of the metric tensor symmetry. Moreover, an extra reduction is possible due to the flexibility in selecting coordinates, leaving six independent components.
Lastly, this is reduced to only two independent components by the FLRW metric's underlying assumptions of homogeneity and isotropy. The Cosmological Principle's restrictions allow the metric for a flat universe to be expressed as a diagonal matrix in Cartesian coordinates:

$$g_{\mu\nu} = diag[-1, a^2(t), a^2(t), a^2(t)] \tag{2.27}$$

We can prove further for the above metric equation, the Levi-Civita connection Eq.(2.3) reduces to:

$$\Gamma^0_{00} = \Gamma^0_{0i} = \Gamma^i_{00} = \Gamma^i_{0\beta} = 0 \tag{2.28}$$

$$\Gamma^0_{ij} = \delta_{ik}\dot{a}a = \delta_{ij}a^2H \tag{2.29}$$

$$\Gamma^i_{0j} = \Gamma_{j0} = \delta ik\frac{\dot{a}}{a} = \delta_{ik}H \tag{2.30}$$

where the Kroneker delta is defined as $\delta_{ij} = diag(1,1,1)$. This is expected since the metric's symmetry and the time-time g_{00} component, which is a constant and all partial derivatives $\partial\mu$ are zero, require that all off-diagonal components disappear. Furthermore, only the time derivation ∂_0 survives the calculation since all of the space-space components g_{ij} depend exclusively on time. We must compute the Ricci tensor and the Ricci scalar by entering Eq. (2.3) in the formulation of $R_{\mu\nu}$ in order to solve Einstein's field equations Eq. (2.5). From the time-time elements we have:

$$R_{00} = -3\frac{\ddot{a}}{a} \tag{2.31}$$

,

while from the space-space components we obtain:

$$R_{ij} = \delta_{ij}(2\dot{a}^2\ddot{a}a) \tag{2.32}$$

The Ricci's scalar is defined as the contraction of the Ricci's tensor with the metric:

$$R = R_{\mu\nu}g^{\mu\nu} = R_{00}g^{00} + R_{ij}g^{ij} = 6\left\{\frac{\ddot{a}}{a} + (\frac{\dot{a}^2}{a})\right\} \tag{2.33}$$

Lastly, we may combine these findings with the Einstein's field equations' formulation for the stress-energy tensor for an ideal fluid. We derive the first Friedmann equation for a flat Universe from the time-time component:

$$\left\{\frac{\dot{a}}{a}\right\}^2 = \frac{8\pi G}{3}\rho \tag{2.34}$$

Since the Universe is an isolated system and energy must be conserved. The Friedmann equations are thus connected by the adiabaticity requirement, so even they are the two independent equations of the tensorial equation Eq. (2.5), they are not independent. Thus, starting with the fundamental law of thermodynamics

$$dU = -pdV \Rightarrow d(\rho a^3) = pda^3 \tag{2.35}$$

as the volume scales according to the scaling factor's cube. The way that each fluid component's energy density changes as the Universe expands is constrained by this equation.

We may now include a few helpful parameters that condensibly represent the information of physical importance. The Hubble parameter has previously been encountered

$$H(t) = \frac{\dot{a(t)}}{a(t)} \tag{2.36}$$

,

which quantifies the expansion rate of the Universe. Another useful quantity is the density parameter of the fluid s

$$\Omega_s(t) = \frac{\rho_s(t)}{\rho_{crit}} = 8\pi G \frac{\rho_s(t)}{3H_0^2} \tag{2.37}$$

explaining how the fluid density changes. Now, we can more easily state the first Friedmann equation while accounting for the variety of species found in the cosmic fluid:

$$\frac{H^2(t)}{H_0^2} = \sum_s \Omega_s(t) \tag{2.38}$$

2.2.1 Equation of state

A fluid species' pressure and energy density are related by the equation of state, which is a function $p_s = p_s(\rho_s)$, where p_s is the pressure and ρ_s is the density. The general form of the equation of state is :

$$p_s = w_s \rho_s \tag{2.39}$$

with w_s a dimensionless constant, whose value is set by the species. In particular:

- non-relativistic matter: $p = Nk_BT \simeq 0 \rightarrow w_s \simeq 0$;
- radiation and relativistic matter: $p = \frac{1}{3}\rho \rightarrow w_s = \frac{1}{3}$;
- cosmological constant: $p = -\rho \rightarrow w_s = -1$.

The fluid species' energy density s as a function of scale factor a may be simply expressed from the adiabaticity requirement in Eq. (2.35) as :

$$\rho(t) \propto a^{-3(1+w_s)} \propto (1+z)^{3(1+w_s)}. \tag{2.40}$$

The evolution of each fluid species across cosmic time may now be reconstructed using Eq. (2.1). Each fluid species' current value may be found using Eq. (2.37).

$$\rho_{0,s} = \frac{3\Omega_{0,s}H_0^2}{8\pi G} = 1.88 \times 10^{-29} \Omega_{0,s} h^2 \,\mathrm{g\ cm^{-1}}, \tag{2.41}$$

where we used the dimensionless Hubble constant:

$$h := \frac{H_0}{100\,\mathrm{km\,s^{-1}\,Mpc^{-1}}}. \tag{2.42}$$

The three separate epochs in the history of the Universe are defined by the dominance of one fluid component over others, and each is distinguished by variations in the development of energy density with redshift, as seen in Fig. 2.1 :

- radiation dominated: the first cosmological epoch sees a prevalence of radiation in the cosmic mixture. This epoch ended at the matter-radiation equivalence around 10^3 years after the Big Bang. In terms of redshift it corresponds to:

$$\rho_{0,\mathrm{m}}\,(1+z_{\mathrm{eq}}^{rm})^3 = \rho_{0,\mathrm{r}}\,(1+z_{\mathrm{eq}}^{rm})^4 \quad \rightarrow \quad z_{\mathrm{eq}}^{rm} \approx 10^4 \tag{2.43}$$

- matter dominated: after the matter-radiation equivalence time, the new epoch of matter domination began. This epoch lasted up to 5 million years ago at the Λ-matter equivalence, when the last cosmic epoch dominated by the cosmological constant began

$$\rho_{0,\Lambda} = \rho_{0,\mathrm{m}}(1+z_{\mathrm{eq}}^{\mathrm{DM}\Lambda})^3 \rightarrow z_{\mathrm{eq}}^{\mathrm{DM}\Lambda} \approx 0.7. \tag{2.44}$$

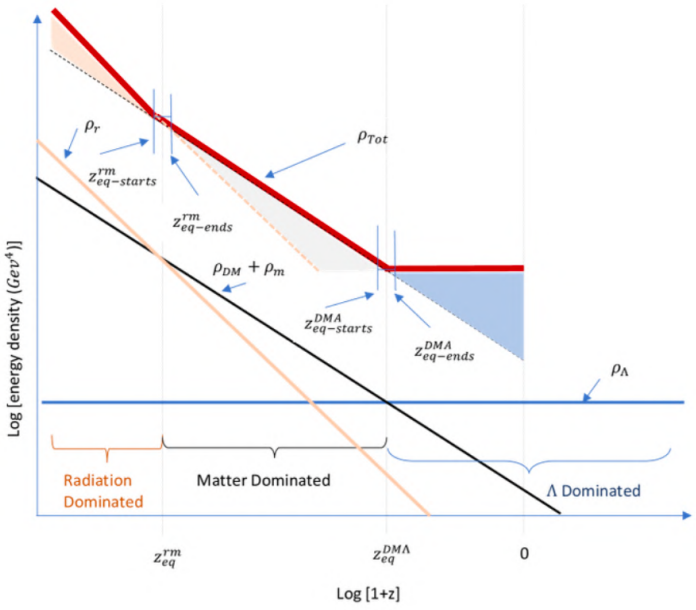

Figure 2.1: Evolution of the radiation, matter and cosmological constant energy densities. On the x-axis, the redshift corresponding to the radiation-matter equivalence and Λ-matter equivalence are reported. The solid red line describes the evolution of the total energy density of the Universe. Credits to [40]

Finally we can express the first Friedmann equation Eq.2.38 using the content of the equation of state as follows:

$$H^2(z) = H_0^2 \sum_s \Omega_{0,s}(1+z)^{3(1+w_s)}. \tag{2.45}$$

2.2.2 Curved Universe

A new term that takes into consideration the contribution of the curvature parameter k must be included in order to generalise Eq. (2.38), which is applicable to a non-flat Universe.

$$H^2(z) = H_0^2 \left\{ \sum_s \Omega_{0,s}(1+z)^{3(1+w_s)} + \Omega_{0,k}(1+z)^2 \right\}, \tag{2.46}$$

where the departure from flatness is quantified by $\Omega_k(z) = 1 - \sum_s \Omega_s(z)$. The fluid's energy density, which manifests with the maximum power of $(1+z)$, dominates at high redshift. The expansion rate $H(t)$ of Eq. (2.38), therefore, approaches the Einstein-de Sitter limit (single-component cosmic fluid and flat Universe) with solution under such circumstances:

$$t = \frac{2}{3} \frac{1}{H_0 \Omega_0^{1/2}} (1+z)^{-3/2}, \tag{2.47}$$

This indicates that any curved Universe goes towards the flat one at extremely early periods and is independent of the cosmological constant and the curvature $\Omega_k(z)$.

Depending on the value of $\Omega_0 = \sum_s \Omega_{0,s}$, we have different curved models:

- Closed models ($\Omega_0 > 1$): The Universe will ultimately approach a maximum scale factor. Setting $\dot{a} = 0$ allows us to determine the highest scale factor that corresponds to

$$a_{\max} = a_0 \left(\frac{\Omega_0}{1 - \Omega_0} \right)^{1/(1+3w)}. \tag{2.48}$$

  Given the quadratic nature of Eq. (2.38), the symmetry suggests that the expansion will eventually reverse. As a result, a closed Universe will experience the Big Crunch at $2t(a_{max})$, when its scale factor vanishes.

- Open models ($\Omega_0 < 1$): The scaling factor $a(t)$ for open models grows monotonically and never reaches a maximum. We can confirm that the scale factor grows linearly with time during the radiation and matter era by solving Eq. (2.38).

$$H(t) \propto \frac{1}{t}, \tag{2.49}$$

  and so the Universe expands forever.

The evolution of the scale factor $a(t)$ is reported in Fig. 2.2 and underlines how the three possible geometries converge to the same one in the early Universe.

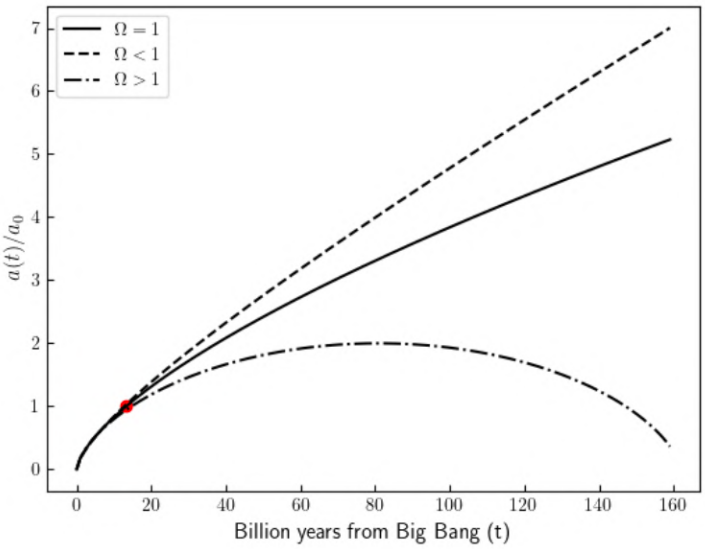

Figure 2.2: Scale factor evolution in Universes with various geometries. For a closed universe ($\Omega > 1$), the evolution is represented by the dot-dashed line; for an open Universe ($\Omega < 1$), the dashed black line is used. A geometrically flat Universe is represented by the solid line ($\Omega = 1$). The current time is represented by the red dot.[45]

2.3 ΛCDM Model

The $\Lambda-$cold dark matter model, which is the current concordance model of cosmology, is based on the ideas that have been presented thus far.
Let us examine what each term in ΛCDM means.

2.3.1 Λ - the cosmological constant

As told, this symbol stands for the cosmological constant, which was added to Einstein's field equations and is what causes the Universe to expand accordingly. It counteracts the gravitational attraction of matter on smaller scales by functioning as a source of gravitational repulsive force. Geometric restrictions and observational data are used to determine the value of Λ. It is very tiny, with a recent estimate of $\Lambda \approx 1.1 \times 10^{-56} cm^{-2}$.

The cosmological constant and vacuum energy are linked in a not yet clear scientific explanation: even empty space has energy, according to relativistic quantum physics, because of quantum fluctuations that are constrained by the Heisenberg uncertainty principle's detectability constraints. Theoretical predictions and measurements, however, differ significantly: quantum field theory predicts a vacuum energy density that is around 120 orders of magnitude higher than what cosmology deduces empirically. One of the largest problems in contemporary physics is still resolving this enormous discrepancy, which is referred to as the cosmological constant problem.

2.3.2 CDM - cold dark matter

The term CDM describes a kind of stuff that is invisible to telescopes because it does not emit, absorb, or interact with electromagnetic radiation. As previously described Zwicky initially proposed the idea of dark matter in 1933 [63], when he found a new kind of matter called Dunkle Materie (missing matter), which is far more prevalent than regular matter. Several observable findings then provided support for this hypothesis:

- Galactic rotation curves: Stars in galaxies revolve more quickly than can be explained by visible matter alone, according to observations of their rotational velocities, suggesting the existence of an invisible mass component [61].
- Gravitational lensing: Galaxy clusters bend light from far-off objects more strongly than would be predicted given their observable mass, suggesting the presence of extra mass in the form of dark matter [60].
- Cosmic microwave background: The statistical characteristics of the temperature variations in the CMB point to the necessity of dark matter to account for the development of structures from the early Universe to the present [12].
- LSS formation: The observed distribution of galaxies and galaxy clusters is produced by dark matter, according to models of the evolution of cosmic structures [15].

Dark Matter is cold because its particles have little kinetic energy and travel slowly in relation to the speed of light. Due to gravitational pull, this feature makes sure that dark matter clumps effectively in the early Universe, promoting the creation of massive structures like galaxies and galaxy clusters. Virialized structures with masses less than $10^{16} M_{\odot}$ could not have developed with just hot dark matter. This excludes out hot components like neutrinos as the predominant dark matter component.

One of the major unanswered questions in cosmology is the precise makeup of CDM. Infact although the existence of dark matter is generally acknowledged, its particle makeup is yet unknown. Although a number of ideas have been put up, including primordial black holes, white holes, sterile neutrinos, axions, and weakly interacting massive particles (WIMPs), none of these have enough empirical evidence to be taken into considered as a definite solution to the CDM problem. Although the goal of particle collision experiments like the one at the Large Hadron Collider and direct detection investigations is to find or create dark matter particles, no conclusive discovery has been achieved so far.

2.3.3 Inflation and the six ΛCDM model parameters

For the ΛCDM model to be fully predictive, inflation seems to be a necessary component. As previously described the first perturbations in the very early Universe that eventually developed into the structures we see today were created by this quantum perturbations in the inflation field. The scale factor rose exponentially over time throughout the inflationary period which, according to standard inflationary models, lasted from 10^{-36} s to 10^{-32} s [18]. More specifically, it is anticipated that there would be

$$N = \ln\left(\frac{a_f}{a_i}\right) \gg 60, \tag{2.50}$$

where a_f and a_i represent the scale factor at the end and beginning of inflation, respectively. A statistical imprint on the primordial perturbations may be left by inflation breaking symmetry in a parity-violating scenario. Specifically, as new particles are created by inflaton decay during inflation, particle exchanges may result in non-Gaussianities in these primordial fluctuations [21], [2]. Furthermore, a phase of magnetogenesis is suggested by various parity-violating inflationary theories as the cause of the symmetry breakdown [17].

Ultimately, the concordance model of cosmology describes a geometrically flat Universe with early perturbations caused by the inflationary process, dominated by CDM and Λ. With just a few essential factors, this model predicts the Universe's development with remarkable accuracy. An outline of the main parameters that are used to build the ΛCDM model is provided below:

- **Hubble constant** H_0: This parameter, as previously mentioned, characterizes the universe's present pace of expansion. According to indirect CMB observations[48], its value is

  $$H_0 \approx 67.4\,\mathrm{km\,s^{-1}\,Mpc^{-1}}, \tag{2.51}$$

  while the value derived from local distance ladders [52] is

  $$H_0 \approx 73\,\mathrm{km\,s^{-1}\,Mpc^{-1}}. \tag{2.52}$$

- **Matter density parameter** $\Omega_{0,m}$: The present total matter density of the universe, including baryonic and CDM stuff, normalized to the critical density, is this parameter's definition. It governs how hierarchical structures are formed. It usually has the following value:

  $$\Omega_{0,\mathrm{m}} \approx 0.31 \ . \tag{2.53}$$

- **Baryonic density parameter** $\Omega_{0,b}$: It is the portion of the Universe's energy

density that is assigned to baryons, or ordinary stuff.

$$\Omega_{0,\mathrm{b}} \approx 0.049 \tag{2.54}$$

- **Dark energy density parameter** Ω_Λ: It stands for the energy density linked to the cosmological constant, which causes the Universe to accelerate.

$$\Omega_\Lambda \approx 0.69 \ . \tag{2.55}$$

- **Curvature parameter** $\Omega_{0,k}$: Current measures provide support on the Euclidean geometry laws since $\Omega_k \approx 0$ in the ΛCDM model, which is related to the present geometry of the Universe.

- **Spectral index** n_s: It describes the shape of the primordial power spectrum $P(k) \propto k^{n_s}$

$$n_s \approx 0.96 \ . \tag{2.56}$$

- **Amplitude of fluctuations** σ_8:Measures the strength of matter clustering on scales of 8 h^{-1} Mpc,

$$\sigma_8 \approx 0.8 \ . \tag{2.57}$$

- **Optical depth** τ: The transparency of the Universe to photons during reionization, which took place when the first bright objects (probably Pop. III stars) ionised the surrounding gas, is measured by this parameter. Through Compton scattering, the free electrons created during reionization dispersed CMB photons, leaving a noticeable mark on the CMB polarisation. This aids in establishing the date of the reionization phase.

$$\tau \approx 0.054 \ . \tag{2.58}$$

These results have been provided by Planck 2018 data[48].

Chapter 3

3 Evolution of cosmic structures

A key cosmological probe is provided by galaxy is clustering, which describes matter's propensity to form cosmic formations rather than be evenly distributed over space.
As was described in the last chapter, CMB observations show that the early Universe has a nearly uniform distribution of stuff. But throughout time, tiny density fluctuations that were there in the early phases of cosmic evolution expanded, giving rise to galaxies, galaxy clusters, and the enormous filamentary formations that are seen today. According to the energy-time uncertainty requirement $\Delta E \Delta t > \hbar/2$, these disturbances are predicted to arise in the primeval Universe, where tiny matter fluctuations are permitted. The little variations in temperature and density in the CMB at z approximately 1100 demonstrate their existence:

$$\frac{\delta T}{T} \sim \frac{\delta \rho}{\rho} \sim 10^{-5} \ . \tag{3.1}$$

Gravitational forces are the main factor behind the creation of structures; they attract matter to areas that are overly dense, intensifying these early inhomogeneities.

3.1 Metric perturbation

Beginning with the Big Bang and continuing through the creation of the first atoms, Big Bang nucleosynthesis, and dark matter generation, the homogenous Universe underwent a thermal history of evolution. The creation of the structure is intricate and necessitates approximations, solving the equations governing the evolution of cosmic species

Let us start by adding small perturbations $|h_{\mu\nu}| \ll 1$ to the FLRW metric given by Eq. (2.10):

$$\begin{cases} g_{00}(t,\vec{x}) = -1 + h_{00}(t,\vec{x}) \\ g_{0i}(t,\vec{x}) = g_{i0}(t,\vec{x}) = a(t) h_{0i}(t,\vec{x}) \\ g_{ij}(t,\vec{x}) = a^2(t)[\delta_{ij} + h_{ij}(t,\vec{x})]. \end{cases} \tag{3.2}$$

For the perturbed metric, Eq. (3.2), we have 10 extra degrees of freedom provided by the independent components of the symmetric 4-dimensional perturbation tensor $h_{\mu\nu}$, whereas for the flat homogeneous Universe we had only one degree of freedom, that is the scale factor a. Let us describe each aspect of the perturbation in details.

- h_{00}: the time-time component is a 3-scalar, therefore it is invariant under any spatial rotation. Given an arbitrary scalar field A, this component can be written as:

$$h_{00} = -2A \ . \tag{3.3}$$

  where the prefactor -2 is a convention.

- h_{0i}: The Helmholtz decomposition theorem, which asserts that any sufficiently smooth vector field that decays quickly at infinity can be uniquely decomposed into the sum of an irrotational component, represented by a scalar potential, and a solenoidal component, represented by a vector potential, can be used to break down the time-space perturbation, which is a 3-vector. When a solenoidal 3-vector field $B_i(t, \vec{x})$ and an arbitrary 3-scalar field $B(t, x)$ are introduced, the perturbation can be written as the sum of the longitudinal and transverse parts:

$$h_{0i} = -\frac{\partial B}{\partial x^i} - B_i. \tag{3.4}$$

- h_{ij}: The space-space component is a symmetric tensor in three dimensions. In order to generalize the Helmholtz decomposition theorem, we add a solenoidal vector field $V_i(t, \vec{x})$ and two arbitrary 3-scalar fields $D(t, \vec{x})$ and $E(t, \vec{x})$. Even though the perturbation tensor contains ten independent components, this decomposition only offers eight degrees of freedom (4 scalar functions and 2 transverse vectors). This indicates that we are lacking two degrees of freedom, known as the transverse-traceless components h_{ij}^{TT}, which cannot be represented as scalar or vector combinations. Consequently, the spatial perturbation's complete decomposition is provided by:

$$h_{ij} = 2D\delta_{ij} - 2\frac{\partial^2 E}{\partial x^i \partial x^j} + \frac{\partial V_i}{\partial x^j} + \frac{\partial V_j}{\partial x^i} + h_{ij}^{TT} \ . \tag{3.5}$$

Any tensor can be subjected to this general decomposition. Because of the symmetry of the FLRW metric, it leads to a significant finding known as the decomposition theorem, which asserts that 3-scalar, 3-vector, and 3-tensor perturbations evolve separately at linear order. This finding is essential to cosmology because it makes it possible to independently investigate scalar perturbations, which are what cause structures to grow.

3.1.1 Conformal Newtonian gauge

A choice of coordinates is commonly referred to as the gauge in general relativity, and finding gauge invariance under coordinate transformation is crucial for lowering the number of free parameters in the equations and enabling resolution. Examine a generic scalar field $\phi(\vec{x}, t)$ that is obtained by applying a baseline term $\bar{\phi}(t)$ to a minor scalar perturbation $\delta\phi(\vec{x}, t)$:

$$\phi(\vec{x},t) = \bar{\phi}(t) + \delta\phi(\vec{x},t). \tag{3.6}$$

Our goal is to comprehend the changes in this field under the general small coordinates transformation $x_\mu \to \hat{x}^\mu(x^\mu)$. This prerequisite is required to permit a Taylor expansion of the transformed coordinates and to maintain the perturbations' small magnitude:

$$\begin{cases} \hat{t} = t + \zeta(t,\vec{x}) \\ \hat{x}^i = x^i + \frac{\partial\xi(t,\vec{x})}{\partial x^i}, \end{cases} \tag{3.7}$$

where the time and space changes are denoted by ζ and ξ, respectively, and are regarded as first-order disturbances. We get the rule for scalar perturbations transformations by utilizing the scalar transformation law:

$$\hat{\delta}\phi(\hat{t},\vec{\hat{x}}) = \delta\phi(\hat{t},\vec{\hat{x}}) - \frac{d\bar{\phi}(\hat{t})}{d\hat{t}}\zeta(t,\vec{\hat{x}}) \ . \tag{3.8}$$

We concentrate on the scalar fields A, B, D, and E as specified in Eqs. (3.3), (3.4), and (3.5), taking the decomposition for scalar perturbations only. The formulae for the converted scalar fields can be obtained by applying the tensor transformation rule to the metric components $g_{\mu\nu}$:

$$\begin{cases} \hat{A} = A - \dot{\zeta} \\ \hat{B} = B - a^{-1}\zeta + a\dot{\xi} \\ \hat{D} = D - \frac{\dot{a}}{a}\zeta \\ \hat{E} = E + \xi. \end{cases} \tag{3.9}$$

Four scalar functions (A, B, D, and E) determine the scalar perturbation transformation rule, which in turn depends on two spacetime shift functions (ζ, ξ). This transformation is helpful for lowering the degrees of freedom. Thus, we have two degrees of freedom remaining. It is possible to set two equations from the set (3.9) equal to zero, by selecting the shift functions properly. The conformal Newtonian gauge is based on this method, in which we choose (ζ, ξ) so that B and E disappear. We have thus seen how the number of degrees of freedom in the metric is decreased by selecting particular coordinates. The decrease from 10 to 6 degrees of freedom is caused by this coordinate selection, sometimes referred to as gauge freedom.

The FLRW metric with scalar perturbations is commonly expressed using the usual Bardeen potentials ϕ_A and ϕ_H [4]:

$$\Phi_A := A + \frac{\partial}{\partial t}\left(a^2\dot{E} - aB\right) \ , \tag{3.10}$$

$$\Phi_H := -D + \dot{a}\,(B - aE) \quad . \tag{3.11}$$

Thus, the perturbed metric can be expressed as:

$$ds^2 = -(1 + 2\Phi_H)dt^2 + a(t)^2\left[(1 - 2\Phi_A)\delta_{ij}\right]dx^i dx^j, \tag{3.12}$$

Finally, we can apply the conformal Newtonian gauge conditions $E = B = 0$ to the Bardeen potentials, yielding $\phi_H = -\phi$ and $\phi_A = \psi$. In this gauge, the perturbed FLRW metric takes the form:

$$\begin{cases} g_{00}(t, \vec{x}) = -1 - 2\psi(t, \vec{x}) \\ g_{i0}(t, \vec{x}) = g_{0i}(t, \vec{x}) = 0 \\ g_{ij}(t, \vec{x}) = a^2(t)\delta_{ij}\left[1 + 2\phi(t, \vec{x})\right], \end{cases} \tag{3.13}$$

where ψ is the well-known Newtonian potential and ϕ is the local perturbation of the scale factor. Both the scalar fields have magnitudes $< 10^{-4}$, making them suitable for linear theory.

3.1.2 Boltzmann equations

The equations controlling the evolution of perturbations in each fluid species in the ΛCDM model, excluding the perturbations of the cosmological constant, may now be derived since we have chosen a gauge for the metric perturbations.
In cosmology, we examine the statistical distributions of cosmic components rather than the evolution of their individual particles. Let's look at a group of particles in the phase with space coordinates (x, p), where the dynamics of the system depends on the position and momentum of each individual particle. The uncertainty principle restricts our knowledge of a particle's location to within an uncertainty of $\hbar$ since it is impossible to pinpoint a particle's precise location in phase space. As shown in Fig. 3.1, the phase space for each particle is therefore not a collection of discrete points but rather it is separated into 6-dimensional cells with volumes determined by quantum units, $\Delta V = \Delta\vec{x}\Delta\vec{p}/(2\pi\hbar)^3$. One can calculate the quantity of particles in a single phase-space cell as follows:

$$N_{\text{part}} = f_1(\vec{x}, \vec{p}, t)dV = f_1(\vec{x}, \vec{p}, t)\frac{\Delta\vec{x}\Delta\vec{p}}{(2\pi\hbar)^3}, \tag{3.14}$$

where the probability density to discover a particle in a particular condition is described by the 1-particle distribution function, $f_1(\vec{x}, \vec{p}, t)$. The Fermi-Dirac distribution for fermions and the Bose-Einstein distribution for bosons are two well-known equilibrium distribution functions that characterize particle evolution in phase space for a collisionless

system.

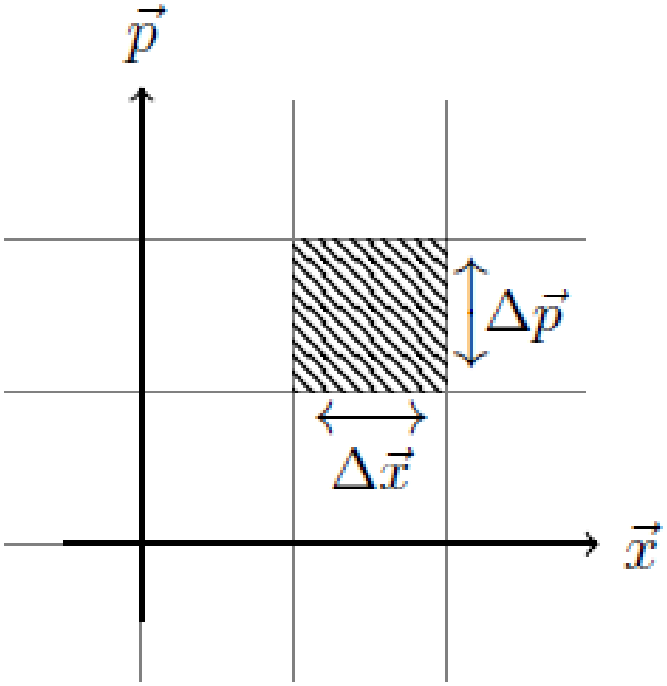

Figure 3.1: Discretization of the phase space [16]

Their distribution functions must be calculated in order to comprehend the evolution of cosmological species, especially because species are frequently out of equilibrium in the context of cosmology, particularly when examining the growth of structures.

The Bogoliubov–Born–Green–Kirkwood–Yvon (BBGKY) hierarchy describes the dynamics of a generic system with many interacting particles. The $n-$particle distribution function and the $(n+1)$ particle distribution function are related by a set of linked equations that make up this hierarchy:

$$f_n(\vec{x}^{(n)}, \vec{p}^{(n)}, t) \sim \int dV f_{n+1}(\vec{x}^{(n+1)}, \vec{p}^{(n+1)}, t). \tag{3.15}$$

Internal dependencies in this series of equations reach all the way up to the system's particle count. This indicates that it is impossible to calculate the distribution function of any one particle in the system without also calculating the distribution function of every particle. Consequently, the issue turns into the hierarchy's closure to a certain extent. To terminate the sequence in Eq. (3.15), at an appropriate order, approximations are required. In particular, the Boltzmann equation can be obtained by truncating at the first equation, which is allowed under the assumption of molecular chaos (Stosszahlansatz). For a collisionless system, the Boltzmann equation conserves the total number of particles and takes the form:

$$\frac{df_n(\vec{x}, \vec{p}, t)}{dt} = 0 \implies \nabla_x \cdot \frac{d\vec{x}}{dt} + \nabla_p \cdot \frac{d\vec{p}}{dt} + \frac{\partial f}{\partial t} = 0. \tag{3.16}$$

The flux of particles into and out of a phase-space volume element is described by the equation in this instance. According to Liouville's theorem, the system's collisionless nature guarantees conservation of the occupied phase-space volume. However, this conservation breaks down when particle interactions are taken into account, making the Boltzmann equation non-zero. In particular, it acquires a collision term, $C[f]$, which takes into consideration all particle interactions (preserving 4-momenta) as well as quantum phenomena as Pauli blocking, Bose enhancement, and differences between bosons and fermions:

$$\frac{df_n(\vec{x},\vec{p},t)}{dt} = 0 \implies \nabla_x \cdot \frac{d\vec{x}}{dt} + \nabla_p \cdot \frac{d\vec{p}}{dt} + \frac{\partial f}{\partial t} = C[f]. \tag{3.17}$$

3.1.3 Perturbed Boltzmann equations

The perturbation of the metric described in the conformal Newtonian gauge in Eq. (3.13), in order to complete the picture, must be included in the Boltzmann equation. We begin by rewriting the equation explicitly using the physical momentum $\vec{p} = p.\hat{p}$, starting from the general form provided in Eq. (3.17).

$$\frac{df}{dt} = \frac{\partial f}{\partial t} + \frac{\partial f}{\partial x^i}\frac{dx^i}{dt} + \frac{\partial f}{\partial p}\frac{dp}{dt} + \frac{\partial f}{\partial \hat{p}^i}\frac{d\hat{p}^i}{dt}. \tag{3.18}$$

The four momentum expression can be derived from the mass-shell condition and is written as

$$P^\mu = (P^0, P^i) = \left(E(1-\psi), \frac{p^i}{a}(1-\phi)\right), \tag{3.19}$$

where E is the system's total energy. This statement can be used to rewrite the Boltzmann equation so that it depends on physical momenta, scalar potentials, and energy. Next, the altered Boltzmann equation looks like this:

$$\begin{aligned}\frac{df}{dt} = \frac{\partial f}{\partial t} + \frac{\partial f}{\partial x^i}\left\{\frac{p}{E}\frac{\hat{p}^i}{a}(1+\psi-\phi)\right\} - \frac{\partial f}{\partial p}\left\{(H+\dot{\phi})p + \frac{E}{a}\hat{p}^i\psi_{,i}\right\} \\ + \frac{\partial f}{\partial p^i}\frac{E}{ap}\left(\delta_{ik} - \hat{p}^i\hat{p}^k\right)\left(\frac{p^2}{E^2}\phi - \psi\right)_{,k} = C[f]\end{aligned} \tag{3.20}$$

where a partial derivative with respect to x^i is indicated by the notation $-, i$. We are now ready to examine the specific applications of the Boltzmann equation to each cosmic species.

Working in Fourier space, the Boltzmann equations take on a simplified form where ik factors are used in place of spatial derivatives when the wave vector $\vec{k}$ is substituted for the spatial coordinate $\vec{x}$. In ΛCDM cosmology, the set of perturbed Boltzmann equations

is given by:

$$\theta' + ik\mu\theta + \phi' + ik\mu\psi + \tau'\left(\theta_0 - \theta + \mu u_b - \frac{1}{2}P_2(\mu)\Pi\right) = 0 \tag{3.21}$$

$$\delta_c' + iku_c + 3\phi' = 0 \tag{3.22}$$

$$u_c' + \frac{a'}{a}u_c + ik\psi = 0 \tag{3.23}$$

$$\delta_b' + iku_b + 3\phi' = 0 \tag{3.24}$$

$$u_b' + \frac{a'}{a}u_b + ik\psi - \frac{4}{3}\tau'\frac{\rho_\gamma}{\rho_b}[u_b + 3i\theta_1] = 0 \tag{3.25}$$

$$N' + ik\mu\frac{p}{E}\nu(p)N - Hp\frac{\partial N}{\partial p} + \phi' + ik\mu\frac{E\nu(p)}{p}\psi = 0 \tag{3.26}$$

The derivative with regard to conformal time η, which is connected to physical time via the equation $d\eta = a^{-1}dt$, is represented by the prime apex here and beyond. The majority of the conclusions and derivations in this chapter are mostly based on [10], which we consult for the complete derivation. Since it summarizes the rules regulating the dynamics of perturbations in the linear regime, this collection of equations is crucial. Each equation represents a unique fluid or species in the presence of metric perturbations ϕ and ψ in the conformal Newtonian gauge, capturing the evolution of density, velocity, and other perturbations for various components of the Universe, including CDM, baryons, and photons.

Eqs. (3.21)-(3.26) typically have their solutions calculated numerically using specialized programs called Boltzmann solvers, like CLASS [28] and CAMB [30], which offer theoretical predictions essential for a range of cosmological analyses. Theoretical power spectra, which support trispectrum estimation and the parity test result, will be specifically calculated using CAMB in the upcoming chapter.

Here's an overview of each equation:

- The evolution of temperature perturbations, $\theta = dT/T$, with regard to the Bose-Einstein photon distribution is described by Eq. (3.21). The effects of photon motion, notably the free-streaming behavior of photons, are described by the terms θ' and $ik\mu\theta$. In this case, the directional dependence between the perturbations and the photons' momenta is captured by $\mu = \hat{p}^i\hat{k}^i$.
  Metric perturbations, which show how gravitational potentials impact photon energy, are introduced by the words ϕ' and $ik\mu\psi$. The scattering term, $\tau'[\theta_0 - \theta +$

$\mu ub - 1/2P_2(\mu)\Pi]$, describes interactions between photons and baryons. Here, the bulk velocity of the baryonic fluid is described by $\vec{u}_b$, and the monopole term is represented by $\theta_0 = \frac{1}{2\pi}\int d\Omega'\theta(\hat{p}', \vec{x}, t)$. The quadrupole θ_2 and its photon polarization field $\theta_{p,2}$ are involved in the angular dependence of the Compton scattering, which is described by the final term, where $\Pi = \theta_2 + \theta_{p,2} + \theta_0$ and P_2 is the Legendre polynomial.

The collision terms push θ in the direction of the monopole term θ_0 when bulk velocity is absent. Only the monopole term remains when the scattering is extremely efficient, since the temperature anisotropies are essentially washed out. This suggests intuitively that all photons tend to reach the same local temperature when their mean free path is extremely short. On the other hand, multipole terms and, as a result, anisotropies in the temperature distribution require bulk velocity.

Finally, this equation is linear, indicating that it models perturbations grow in the linear regime. This linear growth implies that perturbations do not increase significantly throughout cosmic timewhich is accurate to describe CMB photons.

- The number density contrast of CDM is shown by δc in Eq. (3.22) which is the continuity equation. The development of CDM is essential to the creation of structures because it clumps effectively and generates baryonic drag, or potential wells that collect baryonic stuff. CDM is regarded as an effective fluid since it is non-relativistic and solely interacts gravitationally. Consequently, the Boltzmann equation assumes a simple collision term of zero form. But since the bulk velocity u_c also appears in the equation, we require additional formula to correct the CDM hierarchy. Eq. (3.23) is the Euler equation following the momentum conservation. Because dark matter is cold, the second moment of the Boltzmann equation is negligible and the Boltzmann hierarchy can be closed.

- In cosmology, the terminology used in baryons include electrons, protons, neutrons, helium, and trace amounts of heavier nuclei. The proton mass is commonly used as a baryon representative mass. The rate of collisions between protons and electrons, which occurs through Coulomb scattering, is far greater than the expansion rate of the Universe prior to recombination. We can employ a single overdensity number for protons and electrons because of this relationship. Following recombination, baryonic matter exhibits non-relativist behavior, and the collision term disappears because of the conservation of the total electron and proton numbers, making the continuity equation for baryons, Eq. (3.24), equal to that of CDM.

  On the other hand, the effects of Compton scattering between photons and electrons are included in the Euler equation for baryons prior to recombination. In this case, the scattering term contains the dipole component, which is defined as $\theta_1(k, \eta) = i\int_0^1 d\mu\mu/2\theta(\mu, k, \eta)$. The anisotropic mobility of electrons in response to

temperature gradients is captured by this dipole term: electrons traveling toward hotter regions experience a headwind effect that causes them to shift in the opposite direction. Compton drag is the name given to this phenomena.

- The evolution of temperature perturbations, $N = dT/T$, in the Fermi-Dirac neutrino distribution is governed by Eq. (3.26). The collision term is set to zero since neutrinos interact weakly over the relevant periods. Redshifting effects on neutrino momenta are taken into account by $Hp\delta N/\delta p$, whilst the neutrino free-streaming properties are captured by the term $ik\mu Np/E_\nu(p)$.
  Although neutrinos are regarded as massless in this discussion, it is crucial to emphasize that they do have a little mass (current constraints show that $\sum m_\nu < 0.07244$ [1]), and that neutrino mass is taken into consideration by a number of non-standard cosmological models. Actually, by using precise power spectrum measurements, cosmological models themselves are effective instruments for constraining neutrino masses.

3.1.4 Perturbed Einstein's field equations

We covered how to handle non-gravitational interactions when scalar perturbations are included in the metric Eq. (3.13), in the preceding section. We now discuss gravity, whose behavior is determined by Eq. (2.5).

To compute the left-hand side of Einstein's field equations to linear order, we must first add scalar perturbations of the metric to the formulae for the Levi-Civita connections. The perturbed form of Γ is produced by this process, which is comparable to the one outlined in Sec. 2.2:

$$\Gamma^0_{00} = \psi, \tag{3.27}$$

$$\Gamma^0_{i0} = \delta_i\psi, \tag{3.28}$$

$$\Gamma^i_{00} = a^{-2}\delta_i\psi, \tag{3.29}$$

$$\Gamma^0_{ij} = \delta_{ij}a^2[H + 2H(\phi + \psi) + \dot{\phi}], \tag{3.30}$$

$$\Gamma^i_{0j} = \delta_{ij}(H + \dot{\phi}), \tag{3.31}$$

$$\Gamma^i_{jk} = \phi(\partial_k\delta_{ij} + \partial_j\delta_{ik} - \partial_i\delta_{jk}) \ . \tag{3.32}$$

Recovering the expression for the Ricci tensor Eq.(2.4) restricted to the time components only, we get:

$$R_{00} = \partial_\alpha \Gamma^\alpha_{00} - \partial_0 \Gamma^\alpha_{0\alpha} + \Gamma^\beta_{00}\Gamma^\alpha_{\beta\alpha} - \Gamma^\beta_{0\alpha}\Gamma^\alpha_{\beta 0} \tag{3.33}$$

We observe that there are second-order terms for $\beta = 0$ but that $R_{00} = 0$ for $\alpha = 0$. Both α and β must be spatial indices since we exclude terms at higher orders as we are operating at the linear order. The perturbed time-time component of the Ricci tensor in Fourier space can be expressed as follows:

$$R_{00} = -3\frac{\ddot{a}}{a} - \frac{k^2}{a^2}\psi - 3\ddot{\phi} + 3H(\dot{\psi} - 2\dot{\phi}) \ . \tag{3.34}$$

For the spatial components, the computation is more complex as it involves all indices. Starting with the space-space components of the Ricci tensor,

$$R_{ij} = \partial_\alpha \Gamma^\alpha_{ij} - \partial_j \Gamma^\alpha_{i\alpha} + \Gamma^\beta_{ij}\Gamma^\alpha_{\beta\alpha} - \Gamma^\beta_{i\alpha}\Gamma^\alpha_{\beta j} \ , \tag{3.35}$$

we substitute the results for the Levi-Civita connections to obtain the perturbed expression for the spatial Ricci tensor:

$$R_{ij} = \delta_{ij}\left[(2a^2H^2 + a\ddot{a})(1 + 2\phi - 2\psi)) + a^2H(6\phi_{,0} - \psi_{,0}) + a^2\phi_{,00} + k^2\phi\right] + k_ik_j(\phi + \psi) \ . \tag{3.36}$$

By contracting the components $R_{\mu\nu}$ with the metric components $g_{\mu\nu}$ yields the Ricci scalar:

$$\begin{aligned} R = &(-1 + 2\psi)\left[-3\frac{\ddot{a}}{a} - \frac{k^2}{a^2}\psi - 3\phi_{,00} + 3H(\psi_{,0} - 2\phi_{,0})\right] \\ &+ \frac{1 - 2\psi}{a^2}\left\{3\left[\left(2a^2H^2 + a\ddot{a}\right)(1 + 2\phi - 2\psi) + a^2H(6\phi_{,0} - \psi_{,0})\right] + a^2\phi_{,00} + k^2\phi\right\} + k^2(\phi + \psi). \end{aligned} \tag{3.37}$$

By discarding all nonlinear terms in ψ and ϕ, we obtain the first-order part of the Ricci scalar:

$$\delta R = -12\psi\left(H^2 + \frac{\ddot{a}}{a}\right) + 2\frac{k^2}{a^2}\psi + 6\phi_{,00} - 6H(\psi_{,0} - 4\psi_{,0}) + 4\frac{k^2}{a^2}\phi \ . \tag{3.38}$$

After acquiring all required terms to complete the geometric side of Einstein's field equations, we can go on to the energy side, which includes the stress-energy tensor. By adding up the energy of each particle species, weighting it by the particle number, and dividing it by the phase-space volume element, we can calculate the energy density of all particles in the Universe, using the discretization of phase space shown in Fig. 3.1:

$$T_0^0(\vec{x},t) = -\rho(\vec{x},t) = -\sum_s g_s \int \frac{d^3p}{(2\pi)^3} E_s(p) f_s(\vec{x},\vec{p},t) \ . \tag{3.39}$$

Here, g_s stands for the degeneracy parameter, which indicates how many quantum states with the same energy are available to a particular particle. Kinetic theory states that the relationship between macroscopic pressure and energy density is $p = 1/3nm|v|^2$, where n is the particle number density in a certain volume. The spatial components of the stress-energy tensor are obtained by applying this relation to Eq. (2.39), which is generalized to relativistic particles as follows:

$$T_j^i(\vec{x},t) = p(\vec{x},t) = \sum_s g_s \int \frac{d^3p}{(2\pi)^3} \frac{p^i p^j}{E_s(p)} f_s(\vec{x},\vec{p},t). \tag{3.40}$$

At last, we possess every element required to compute the perturbed Einstein's field equations. See [11] for a full and exhaustive derivation. The Einstein's field equations that are scalarly perturbed look like this:

$$k^2\phi + 3\frac{a'}{a}\left(\phi' - \psi\frac{a'}{a}\right) = 4\pi G a^2 \left(\rho_c\delta_c + \rho_b\delta_b + 4\rho_\gamma\Theta_0 + 4\rho_{\mathcal{N}_0}\right) \tag{3.41}$$

for the time-time element. When modeling the evolution of modes greater than the Hubble radius H^{-1}, this equation is especially crucial. Observe that when expansion is not present (a = constant), this equation reduces to the standard Poisson equation. Regarding the spatial component, we arrive at

$$k^2(\psi + \phi) = -32\pi G a^2(\rho_\gamma\Theta_2 + \rho_\nu\mathcal{N}_2). \tag{3.42}$$

This equation is important because the perturbation potentials ϕ and ψ are opposite in sign but equal in size when quadrupoles in radiation and neutrino components are negligible, as occurs under tight-coupling situations.

3.2 Formation of cosmic structures

We now investigate the solutions to our equations Eqs. (3.21)–(3.26) and Eqs. (3.41)-(3.42), starting with initial conditions given by inflation. Gravity is mediated by the potentials ϕ and ψ at late periods, when matter dominates the Universe. Anisotropies are mostly associated with monopole and dipole components of radiation perturbations in early radiation-dominated epochs, on the other hand. This suggests that even if radiation and CDM have a weak coupling, radiation anisotropies are nevertheless influenced by CDM disturbances. We will concentrate on CDM perturbations since CDM is a major factor in the development of structures and only relates to other components through gravitational interactions.

Throughout the Universe's history, over-densities of $\delta\rho/\rho \sim 10^{-4}$ can collect enough matter to create the observable cosmic structures. However, there are two opposing factors that oppose this development process:

- Universe expansion: Particles are drawn apart by the cosmic expansion. When the Universe expands, disturbances grow according to a power-law rather than exponentially as they would in a static Universe.
- Baryon and photon pressure: CDM does not show the same behavior as baryons and photons, which impose pressure that increases with density.

3.2.1 Particle horizon

The idea of the particle horizon, often also referred to as the cosmic horizon, must be introduced before we can discuss structure evolution. We covered the recession rule and the instruments required to compute distances in spacetime in Chapter 2. However, the speed of light is not constant in the conventional sense when employing comoving coordinates. The recession velocity, brought on by the expansion of the Universe, modifies the overall velocity of photons, while the special velocity of light stays at c. In particular, if an observer detects a photon at time t_{obs} after it is emitted at time t_{em}, then

$$V_{tot}(t_{em}) \neq V_{tot}(t_{obs}). \tag{3.43}$$

Everything inside a light cone symbolizes events that may have a causal relationship to the observer since a photon's track (its geodesic) in spacetime is the shortest path conceivable. A photon released at time t_{em} and viewed at the current time t_0 (past light cone) has traveled the following distance:

$$r_{LC}(t_{em}) = \int_{t_{em}}^{t_0} \frac{dt'}{a(t')} = \int_0^z \frac{dz'}{H(z')} \tag{3.44}$$

The concept of particle horizon is defined by extending the extremes of integration from the beginning of the Universe to the present.

$$r_H(t) = \int_0^t \frac{dt'}{a(t')} \tag{3.45}$$

This corresponds to $\eta(t)$, the definition of conformal time itself. The particle horizon effectively delineates the boundaries of the visible Universe, acting as a boundary for information. In this way, it delineates the domain of scientific investigations.

3.2.2 The evolution of perturbations

The gravitational potential, ϕ, plays a major role in controlling the evolution of cosmic perturbations. Depending on whether the perturbation modes are inside or beyond the

horizon, their behavior differs during cosmic epochs. The development of perturbations may be divided into three phases:

- Early evolution ($k\eta \ll 1$): At this stage, the potential remains constant, and all perturbation modes are outside the horizon.
- Intermediate evolution ($k\eta \geq 1$): As perturbations enter the horizon, they begin to evolve with the changing gravitational potential. Modes that enter the horizon before matter-radiation equality behave differently than those entering after, reflecting the impact of the evolving matter and radiation content.
- Late evolution ($k\eta \gg 1$): In this stage, the potential stabilizes, leading all modes to evolve similarly. However, as the Universe approaches Λ-matter equivalence, the gravitational potential declines due to the dominance of the cosmological constant.

We use the perturbed Einstein field equations (3.41) and (3.42) in conjunction with the Boltzmann equations (3.21)–(3.26) to examine CDM perturbations. We may exclude factors above the dipole in the photon temperature perturbations because photons and electrons are strongly coupled during the radiation era via Compton scattering.
Since CDM dynamics predominate in the matter-dominated epoch, photons may be mainly disregarded. The tight coupling requirement leads to an additional simplification, as Eq. (3.42), which yields the relation $\phi = -\psi$. This closes the set of equations by enabling us to represent the gravitational potential in a simple way. The Boltzmann equations are reduced to the following core set by these simplifications:

$$\theta'_{r,0} + k\theta_{r,1} = -\phi' \tag{3.46}$$

$$\theta'_{r,1} - \frac{k}{3}\theta_{r,0} = -\frac{k}{3}\phi \tag{3.47}$$

$$\delta'_c + iku_c = -3\phi' \tag{3.48}$$

$$u'_c + \frac{a'}{a}u_c = ik\phi \tag{3.49}$$

When analytical derivation is not practical, we frequently turn to interpolating answers since there are no analytical solutions that hold true across all scales and timeframes. Nonetheless, we might examine particular limit instances for which analytical answers are available:

- Super-horizon regime: In this regime, exact solutions can be derived that hold true throughout the entire evolution of the perturbations.

- Horizon entry: We can distinguish between early times, where in the small-scale approximation we can neglect the CDM density perturbation δ_c, and late times, where the large-scale approximation yields a constant gravitational potential ϕ.
- Sub-horizon regime: In this regime, solutions remain exact as we can neglect θ_r for small scales. Conversely, for large scales, the potential stabilizes to a constant value.

This framework helps us understanding the dynamics of perturbations in different epochs of the Universe's evolution, offering insight into structure formation processes.

Super-horizon evolution

The wavelength dependency in Eqs. (3.46), (3.47), and (3.41), can be disregarded in the domain when $k\eta \geq 1$. The adiabaticity requirement is that $\delta_c - 3\theta'_{r,0}$ must be constant, and it is zero. The development of perturbations is described by the parameter $y = \rho_m/\rho_r$. This substitution allows Eq. (3.41), to be reformulated as follows:

$$y + \frac{d\phi}{dy} + \phi = \frac{3y+4}{6(y+1)}\delta_c \tag{3.50}$$

By differentiating both sides with respect to y, we obtain the following second-order differential equation

$$\frac{d^2\phi}{dy^2} + \frac{21y^2+54y+32}{2y(y+1)(3y+4)}\frac{d\phi}{dy} + \frac{\phi}{y(y+1)(3y+4)} \tag{3.51}$$

which can be solved by introducing a new variable $u = \phi y^3/\sqrt{1+y}$. The analytical solution then becomes [22]:

$$\phi(\vec{k}, y) = \frac{1}{10y^3}[16\sqrt{1+y} + 9y^3 + 2y^2 - 8y - 16]\phi(\vec{k}, 0). \tag{3.52}$$

This solution reveals that, for small scales ($y \ll 1$), the potential remains constant at $\phi(0)$, while for large scales ($y \gg 1$), the potential asymptotes to $9/10\phi(0)$.

Horizon entry

Whether perturbations enter the horizon during the matter-dominated period (large scales) or the radiation-dominated era (small scales) has an important effect on how they behave after they approach the horizon. The contributions of radiation can be ignored in the deep matter-dominated period. Under these circumstances, $\phi' = 0$, a constraint imposed by the super-horizon evolution beginning conditions. We then investigate whether constant solutions for the potential are allowed by Eqs. (3.48), (3.49), and (3.41).

In the matter-dominated era, the Hubble parameter scales as $a^{-3/2}$. Using this fact, we can rewrite Eq. (3.48) as follows:

$$\frac{2k^2\phi'}{3a^2H^2} + \left\{\frac{iu_c}{k} + \frac{2\phi}{3aH}\right\}\left(\frac{9a^2H^2}{2} + k^2\right) = 0. \tag{3.53}$$

By differentiating this equation and neglecting all terms proportional to ϕ, we obtain a second order equation for ϕ in the form

$$\alpha\phi'' + \beta\phi' = 0, \tag{3.54}$$

where two real constants, α and β, are involved. The development of the gravitational potential is significantly impacted by the fact that equations such as Eq. (3.54), permit constant solutions. As perturbations cross the horizon during the matter-dominated period, the gravitational potential ϕ stays constant because the starting conditions established by super-horizon scales are maintained.
This result is especially significant since it shows that the forces for structure evolution balance out during the matter period. The large-scale gravitational expansion of the Universe, which tends to stretch and dilute structures, precisely balances the small-scale gravitational pull from overdense places, which would normally force matter to collapse and amplify the density contrast. Consequently, the gravitational potential maintains its original value over time.
The radiation-dominated epoch, when radiation disturbances control the evolution of the potential, occurs when perturbations for tiny scales approach the horizon. In this regime, CDM perturbations are influenced by the potential rather than having a major effect on it. To begin, we use the relation $aH = \eta^{-1}$, which is valid in the radiation period, to calculate the gravitational potential ϕ using Eqs. (3.46), (3.47), and (3.41), eliminating all matter source factors. This results in a connection between the dipole component of the radiation perturbation and the gravitational potential:

$$\phi' + \frac{1}{\eta}\phi = -\frac{6}{\eta^2 k}\theta_{r,1}. \tag{3.55}$$

To obtain a second-order equation, we differentiate this first-order equation, leading to

$$\phi'' + \frac{4}{\eta}\phi' + \frac{k^2}{3}\phi = 0, \tag{3.56}$$

which is the Fourier space form of a damped wave equation. Solving this requires transforming it into a spherical Bessel equation of the first order, with the solution:

$$\phi(\vec{k}, \eta) = 2\left(\frac{\sin x - x\cos x}{x^3}\right)_{k\eta/\sqrt{3}} \mathcal{R}(\vec{k}). \tag{3.57}$$

The curvature perturbation anticipated by inflation is denoted by $\mathcal{R}(k)$. This finding suggests that the potential oscillates and decays as η^{-2} as Fourier modes approach the horizon. The decay is caused by radiation pressure opposing gravitational collapse, which stops perturbation increase. These oscillations are a reflection of sound waves that are produced by the potential. Baryonic acoustic oscillations (BAO) are produced as a result of this oscillating process.

Equations (3.48) and (3.49), which deal with CDM perturbations, may therefore be solved knowing the behavior of ϕ. A differential equation is obtained by merging these equations and encapsulating terms carrying the potential into a source term $S(k, \eta)$:

$$\delta_c'' + \frac{1}{\eta}\delta_c' = 0, \tag{3.58}$$

This has two solutions: $\delta_c = \text{const}$ and $\delta_c = ln(\eta)$ for the related homogeneous equation $S(k\eta) = 0$. Thus, the general solution is a linear mixture of these homogeneous solutions plus an extra term that uses Green's function to account for the source contribution. The outcome is a function that increases logarithmically with the perturbation scale for $k\eta \sim 1$:

$$\delta_c(k, \eta) \propto \text{const} + \ln(k\eta). \tag{3.59}$$

As a direct outcome of CDM's absence of pressure, this important finding shows that even while radiation modes are declining, CDM perturbations can still increase throughout the radiation period.

Sub-horizon evolution

If large-scale modes cross the horizon after matter-radiation equivalence, their potential remains constant throughout the sub-horizon domain. On small scales, however, radiation may be disregarded as $\rho_c\delta_c$ dominates over $\rho_r\theta_{r,0}$. In this case, the Meszaros equation can be derived by the combination of Eq. (3.48), (3.49), and (3.41).

$$\frac{d\delta_c^2}{dy^2} + \frac{2+3y}{2y(y+1)}\frac{d\delta_c}{dy} - \frac{3}{2y(y+1)}\delta_c = 0. \tag{3.60}$$

This hypergeometric equation admits two solutions: a growing mode

$$D_+(a) = a + \frac{2}{3}a_{\text{eq}}, \tag{3.61}$$

known as the growth factor, which drives structure formation, and a decaying mode

$$D_-(y) = \left(y + \frac{2}{3}\right) + \ln\left[\frac{\sqrt{1+y}+1}{\sqrt{1+y}-1}\right] - 2\sqrt{1+y}, \tag{3.62}$$

These two modes combine linearly to form the general solution, although the decaying mode becomes insignificant over time.
By combining the findings from the solutions to the Boltzmann equation, we can finally represent the observed gravitational potential in its general form. The gravitational potential's late-time development is provided by

$$\phi(\vec{k}, a) = \frac{3}{5}R(\vec{k})T(k)\frac{D_+(a)}{a}, \tag{3.63}$$

where T(k) is the transfer function, which captures the potential's decay as modes enter the horizon and pass the matter-radiation equality. The transfer function is normalized to 1 on large scales, such that

$$T(k) := \frac{\phi(\vec{k}, a_{\text{late}})}{\phi_{\text{large scale}}(\vec{k}, a_{\text{late}})}, \tag{3.64}$$

Consequently, as previously determined for large-scale modes, the large-scale potential is equal to 9/10 the primordial value. Usually, numerical codes like CAMB or CLASS are used to compute this transfer function, which propagates the primordial power spectrum over cosmic time. The idea of the power spectrum will be presented in the next part, along with its application to the study of galaxy clustering.

3.3 Statistical properties of the matter

Using Einstein's field equations and Boltzmann equations in the context of a scalar-perturbed FLRW metric, in a conformal Newtonian gauge, we have so far developed the formalism required to characterize the development of the cosmic fluid's pressure and energy. The spatial distribution of cosmic structures across the Universe can be described, in the linear domain. In order to do this, summary statistics like N-point correlation functions can be used in order to compare model predictions with observations. This aspect is critical for the objectives of this work.

3.3.1 2-point correlation function

Our initial step consists in describing the spatial distribution of galaxies as a statistically random stationary point process. This implies that rather than using a fully deterministic model, we take into account the distribution of galaxy locations in the Universe as determined by statistical principles. A realization of the point process is any potential arrangement of galaxies in space that emerges from this probabilistic model. Observing several replicas of the Universe would provide various galaxy structures, each representing a distinct manifestation of the same process. Since we cannot average diverse samplings across multiple Universes, the uniqueness of the Universe is obviously an issue. Assuming the ergodic hypothesis, which enables us to operate with separate subdivisions of our Universe to get statistical significance, is a popular strategy to get around this problem. dV_1 and dV_2 be two infinitesimal comoving volumes. The mean number density of galaxies $\bar{n}$, is necessary to compute the likelihood of finding a galaxy in the center of an infinitesimal comoving volume dV for a stationary point process.

$$dP = \bar{n}\, dV \quad . \tag{3.65}$$

According to the Bayes theorem, the likelihood of two events happening is equal to the first outcome's probability times the second outcome's conditional probability, given the first:

$$dP_{12} = dP_1 \cdot dP(2|1) = dP_2 \cdot dP_{(1|2)}. \tag{3.66}$$

Thus, for two volume elements separated by a comoving distance r, we have the joint probability

$$dP_{12} = \bar{n}^2\, dV_1\, dV_2\, [1 + \xi(r)]\,, \tag{3.67}$$

where ξ is the 2-point correlation function (2PCF). The value of ξ indicates the level of correlation between the two objects:

- $\xi(r) = 0$: The objects are uncorrelated, meaning they are randomly distributed.
- $\xi(r) > 0$: The objects are positively correlated, so the probability of finding a pair of objects at a distance r is higher than in a random distribution.
- $-1 \leq \xi(r) < 0$: The objects are anti-correlated, meaning that the probability is lower at separation r than in a random distribution.

Counting galaxy pair in observational data (designated as DD) and in a random distribution (designated as RR) at comoving separation r is a useful technique for calculating the 2PCF [42]:

$$1 + \xi(r) = \frac{DD(r)}{RR(r)}. \tag{3.68}$$

Now, if we consider a sphere of radius r centered on a galaxy, we can calculate the mean number of galaxies within that sphere as follows :

$$\langle N(< r)\rangle = \int_V dV_2\, \bar{n}\,[1 + \xi(r)] = \bar{n}V + \bar{n}\int_V dV\, \xi(r) = \frac{4}{3}\pi r^3 \bar{n} + 4\pi \int_0^r dr'\, r'^2 \xi(r'), \tag{3.69}$$

The first term denotes the mean galaxy number density in the Universe, while the second term indicates the excess probability in relation to a random distribution and approaches to zero as $r \to \infty$.
We may obtain information on the distribution moments in a discrete model by dividing the Universe into cells that contain no more than one galaxy apiece. Let the mean density of the $i-$th cell be represented by $\langle ni\rangle = \bar{n}dV_i$. All moments of the galaxy count distribution in a single cell are identical since each cell can only contain one galaxy:

$$\langle n_i\rangle = \langle n_i^2\rangle = \cdots = \langle n_i^N\rangle. \tag{3.70}$$

The first moment of the ensemble of cells is simply the sum of first moments across all cells:

$$\langle N\rangle = \left\langle \sum_i n_i \right\rangle = \int_V \bar{n}\, dV_i = \bar{n}V. \tag{3.71}$$

Similarly, the second moment is

$$\langle N^2\rangle = \left\langle \sum_i n_i \sum_j n_j \right\rangle = \bar{n}^2 V^2 + \bar{n}^2 \iint dV_i\, dV_j\, [1 + \xi(r)]\,. \tag{3.72}$$

We can express these results in terms of the normalized fluctuation around the expected number of objects:

$$\langle \Delta \rangle = \frac{N - \langle N \rangle}{\langle N \rangle}, \tag{3.73}$$

where the mean of this fluctuation distribution vanishes, and the variance is

$$\langle \Delta^2 \rangle = \frac{1}{\bar{n}V} + \frac{1}{V^2} \iint dV_i dV_j \left[1 + \xi(r)\right], \tag{3.74}$$

Shot noise, or statistical noise resulting from discretization, is represented as $\frac{1}{(\bar{n}V)}$ in this equation. A continuous definition of the 2PCF can also be given. Correlation functions give the average correlation level of density fluctuations if galaxies are thought of as probes of a continuous density field. Given that the background density is $\rho b = \bar{n}m$ and the mass density at location $\vec{x}$ is $\rho(\vec{x}) = n(\vec{x})m$, the likelihood of discovering an object at $\vec{x}$ is

$$dP(\vec{x}) = n(\vec{x})\, dV = \frac{\rho(\vec{x})}{\rho_b} \bar{n}\, dV. \tag{3.75}$$

Thus, the probability of finding two objects separated by $\vec{r}$ is:

$$d^2 P_{12} = dV_1\, dV_2 \langle n(\vec{x} + \vec{r}) n(\vec{x}) \rangle = dV_1\, dV_2\, \bar{n}^2 \frac{\langle \rho(\vec{x} + \vec{r}) \rho(\vec{x}) \rangle}{\rho_b}. \tag{3.76}$$

By defining the density contrast

$$\delta(\vec{x}) := \frac{\delta\rho(\vec{x})}{\rho} = \frac{\rho(\vec{x}) - \rho}{\rho}, \tag{3.77}$$

and combining Eq.3.67 and Eq.3.76, we find that the 2PCF can be expressed as

$$\xi(|\vec{r}|) = \langle \delta(\vec{x} + \vec{r}) \delta(\vec{x}) \rangle, \tag{3.78}$$

where $\vec{x}$ represents the position of a galaxy in space. An example of how the 2PCF appears at $z = 0$ is illustrated in Fig 3.2.

3.3.2 Power spectrum

Now let us explore the ideas that underlie the power spectrum. The latter is not new to us; in Sec. 2.3.3, when we were talking about the six parameters of the ΛCDM model, we came across the primordial power spectrum. Standard inflationary models assume that no particular size was preferred in the primordial power spectrum of the early Universe. As a result, fluctuations are statistically comparable across all sizes, resulting in a scale-invariant distribution.

This scale invariance is satisfied by a power-law functional form, thus the gauge-invariant curvature perturbation, $\mathcal{R}$, is usually used to parameterize the power spectrum at the conclusion of inflation:

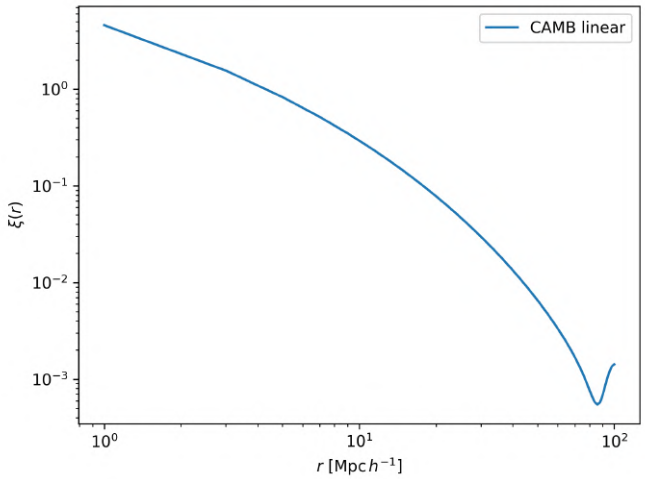

Figure 3.2: Linear 2PCF monopole in real space at $z = 0$, obtained with CAMB [29], for a ΛCDM cosmology using parameters from Planck 2015.

$$P_{\mathcal{R}}(k) := 2\pi^2 \mathcal{A}_s k^{-3} \left(\frac{k}{k_p}\right)^{n_s - 1}, \tag{3.79}$$

where

- $\mathcal{A}_s$ is the scalar amplitude of perturbations, representing the variance of $\mathcal{R}$ around a reference scale k_p, known as the pivot scale.
- n_s is the spectral index, which modulates the distribution of power across different scales.

Assuming a flat distribution of fluctuations, scale invariance suggests that $n_s = 1$, resulting in a constant $P(k)$. The Harrison-Zel'dovich power spectrum, which was first shown in [19],[62] , [43], is the name given to this particular instance. According to the Harrison-Zel'dovich model, power is distributed evenly across all sizes in a universe with a fixed initial gravitational potential. The expected value of the matter density contrast in Fourier space, represented by $\tilde{\delta}(\vec{k})$, defines the matter power spectrum P(k) when taking into account a continuous density field in Fourier space:

$$\langle \tilde{\delta}(\vec{k}) \tilde{\delta}^*(\vec{k}') \rangle := (2\pi)^3 P(k) \delta_D^{(3)}(\vec{k} - \vec{k}'). \tag{3.80}$$

Here, $\delta^{(3)}$ is the 3-dimensional Dirac delta defined as

$$\delta_D^{(3)}(\vec{k}) := \frac{1}{(2\pi)^3} \int_{\mathbb{R}^3} e^{i\vec{k}\cdot\vec{r}} d^3\vec{r}, \tag{3.81}$$

and it upholds the independence of the many forms in the aforementioned statement. It is evident from Eq. (3.78), that the power spectrum may be obtained by performing the Fourier transform of the 2PCF. The Wiener-Khinchin theorem is a significant finding that explains why correlations in object distribution may be studied using the power spectrum.

The Fourier density contrast evolves as described by the growing solution of the linear perturbations:

$$\tilde{\delta}(\vec{k}, t) \propto D_+(t), \tag{3.82}$$

Suppose we have a set of particles with mass m_j and position $\vec{r}_j$. The Fourier amplitude is a sum over the positions [41]:

$$\tilde{\delta}(\vec{k}) \propto \sum_j m_j e^{-i\vec{k}\cdot\vec{r}_j} \tag{3.83}$$

Assume that nonlinearity becomes prominent at a clustering length of r_0. We may quantify the impact on the Fourier amplitude by Taylor expanding the equation above, which shows that nonlinear interactions induce displacements $\Delta\vec{r}_j$ in the particle positions:

$$\Delta\tilde{\delta}(\vec{k}) \propto \sum_j m_j \left[i\vec{k}\cdot\Delta\vec{r}_j - \frac{(\vec{k}\cdot\Delta\vec{r}_j)^2}{2} + \dots \right] e^{i\vec{k}\cdot\vec{r}_j}, \tag{3.84}$$

Since momentum is preserved by the interactions, we anticipate that every mass change on the $j-$th particle is counterbalanced by a corresponding shift of another particle. The disturbances to the power spectrum at scales $k^{-1} \gg r_0$ are of the order $(kr_0)^4$, since the leading term $\vec{k}_x.\Delta\vec{r}$ disappears. The nonlinear contribution is therefore insignificant if the power spectrum approaches a zero value more slowly than k^4 [41].

Since the development of baryons closely resembles that of CDM at late periods, we can use Poisson's equation to connect the total matter density contrast δ_m to the potential Eq. (3.63), which allows us to describe the matter overdensity as follows:

$$\delta_m(\vec{k}, a) = \frac{2ka^2}{3\Omega_m H_0^2}\phi(\vec{k}, a). \tag{3.85}$$

Finally, we have an expression for the linear matter power spectrum at late times:

$$P_L(k, a) = \frac{8\pi^2}{25}\frac{A_s}{\Omega_m^2} D_+^2(a) T^2(k) \frac{k^{n_s}}{H_0^4 k_p^{n_s-1}}, \tag{3.86}$$

whose evolution at different redshifts is shown in Fig 3.3.

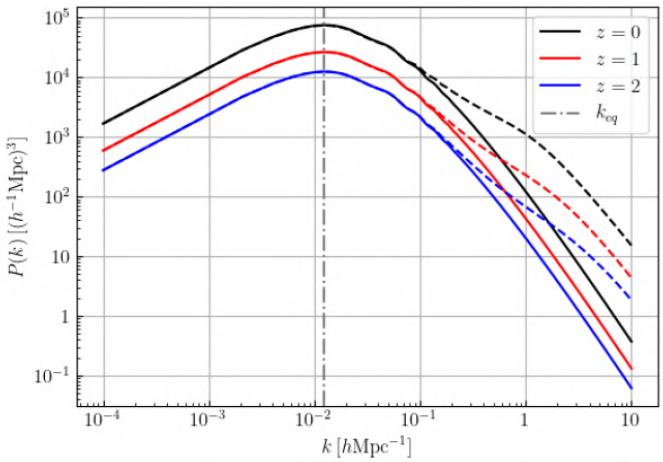

Figure 3.3: Real-space linear (solid lines) and nonlinear (dashed lines) matter power spectra for an ΛCDM cosmology with parameters from Planck 2015 . The power spectra were computed using CLASS, with the nonlinear spectrum obtained via the halofit model [59]. The dot-dashed vertical line marks the scale at which perturbations enter the horizon at matter-radiation equivalence.

Chapter 4

4 Simulations and statistical methods

The TNG Illustris project [38] represents a significant advancement in cosmological simulations, providing detailed insights into the formation and evolution of cosmic structures. This thesis focuses on analyzing dark matter simulations from the TNG project, specifically TNG 100-1, TNG 100-1 Dark, TNG 300-1, and TNG 300-1 Dark. The primary objective is to understand the distribution and clustering of dark matter halos through the visualization of cosmic web structures the calculation of the 2PCF.

The methodology involves using CosmoBolognaLib [34] to compute the 2PCF and TNG official scripts [38] to generate 3D halo/subhalo positions and mass distributions. Additionally, integral constraint corrections were applied to account for the finite size of the simulation boxes in TNG 100-1 and TNG 100-1 Dark. The results are presented through various plots, including 3D scatter plots, and cosmic web structures and 2PCF comparisons.

4.1 Theoretical framework

4.1.1 Dark matter and baryonic matter

As discussed in the previous chapters, dark matter constitutes a significant portion of the Universe's mass, influencing the formation and evolution of cosmic structures. Simula-

tions that include both dark matter and baryonic matter (hydro simulations) provide a more comprehensive understanding of the Universe compared to dark matter-only simulations. The inclusion of baryonic matter allows for the modeling of processes such as gas cooling, star formation, and feedback mechanisms, which are crucial for accurate cosmological simulations. For more detailed explanation, refer to sec 2.3.2 .

4.2 Cosmic web structures

The cosmic web that is the large-scale structure of the Universe, consisting of filaments, voids, and nodes. These structures are formed by the gravitational collapse of dark matter and baryonic matter. Visualizing the cosmic web helps in understanding the distribution of matter and the processes driving the formation of galaxies and clusters.

4.3 Simulation data

The TNG simulations [38] used in this study include:

- **TNG 100-1**: A high-resolution simulation with both dark matter and baryonic matter.
- **TNG 100-1 Dark**: The dark matter-only counterpart to TNG 100-1.
- **TNG 300-1**: A larger volume simulation with both dark matter and baryonic matter.
- **TNG 300-1 Dark**: The dark matter-only counterpart to TNG 300-1.

Table 1: Parameters of the TNG simulation suite

Parameter Description	**TNG300-1-Dark**	**TNG300-1**	**TNG100-1**	**TNG100-1-Dark**
Alternative simulation name	L205n2500TNG_DM	L205n2500TNG	L75n1820TNG	L75n1820TNG_DM
Short description	DM-only analog	Full physics model	Full physics model	DM-only analog
Box size [MPC/h]	205	205	75	75
Avg. gas mass [10^{10} Msun/h]	0.0	0.00074	9.44×10^{-5}	0.0
DM particle mass [10^{10} Msun/h]	0.00473	0.00398	0.000506	0.000600
Number of DM particles	15.6×10^9	15.6×10^9	6.03×10^9	6.03×10^9
Number of gas tracers	0	15.6×10^9	0	0
Redshift range	$127 \rightarrow 0$			
Cosmology	Planck2015 ($\Omega_m = 0.3089$, $\Omega_\Lambda = 0.6911$, $\Omega_b = 0.0486$, $h = 0.6774$)			
Physics model	DM-only	Fiducial TNG	Fiducial TNG	DM-only

Courtesy: TNG Illustries data archive

Note: The simulation parameters may not perfectly match the true cosmic mean density. As a result, the 2PCF computed from these simulations should be interpreted with this limitation in mind.

- **WDM**: Simulation with warm dark matter [9]. The WDM analysis utilizes the Alternative Dark Matter in the TNG universe [9] simulation specifically designed to probe WDM cosmologies.

Table 2: AIDA-TNG 100/A Simulation Parameters for WDM (3 keV) Analysis

Parameter	**DMO**	**FP**	**Units**
Box size	110.7	110.7	Mpc
Dark matter particle mass	7.1×10^7	6.0×10^7	$M_\odot$
Baryon particle mass	–	1.1×10^7	$M_\odot$
Gravitational softening	1.48	1.48	kpc
Dark matter model	CDM/WDM	CDM/WDM	–
WDM mass (thermal relic)	3		keV

Notes:

– DMO = Dark Matter Only; FP = Full Physics (baryonic)
– WDM implementation follows [9] with sharp-k filter at $k_{\rm fs} = 15 Mpc$
– Common cosmology: $\Omega_m = 0.31$, $\sigma_8 = 0.82$, $h = 0.68$

4.4 Integral constraint correction

For the TNG 100-1 Hydro and TNG 100-1 Dark simulations, the finite size of the simulation boxes necessitated the application of an integral constraint correction. This correction accounts for the underestimation of the (2PCF) due to the limited volume, ensuring more accurate clustering measurements. Indeed both in real and simulated extra-galactic surveys, the 2PCF is computed within a finite volume, which introduces a bias, which as said, is known as the integral constraint. Specially this bias arises because the average density of the catalog is used as a reference for calculating the 2PCF. However, analysed region is always a small sample of the Universe, and its average density may not perfectly match the true cosmic mean density. As a result, the 2PCF estimated from any catalog tends to be underestimated on large scales.

The integral constraint correction is especially important for simulations with small box sizes, such as the TNG 100-1 simulations, where the finite volume effects are more pronounced. Without this correction, the clustering measurements would be biased, leading to inaccurate conclusions about the distribution of matter in the universe.

The integral constraint correction can be applied to the measured 2PCF, $\xi_{\text{measured}}(r)$, to obtain the corrected 2PCF, $\xi_{\text{corrected}}(r)$. The correction is given by:

$$\xi_{\text{corrected}}(r) = \xi_{\text{measured}}(r) + \text{IC},$$

where IC is the integral constraint term. Following [53] the term IC can be computed as:

$$I(\hat{f}_{\text{NL}}) = \frac{\sum \theta_{\text{lim}}\, RR(\theta) w_{\text{th}}(\theta, \hat{f}_{\text{NL}})}{\sum \theta_{\text{lim}}\, RR(\theta)},$$

where $I(\hat{f}_{\text{NL}})$ is the integral constraint correction term, which depends on the non-Gaussianity parameter $\hat{f}_{\text{NL}}$,θ_{lim} represents the angular separation limit up to which the correction is applied,$RR(\theta)$ is the random-random pair count at angular separation θ, which is used to normalize the correction, and$w_{\text{th}}(\theta, \hat{f}_{\text{NL}})$ is the theoretical angular correlation function, which depends on the angular separation θ and the non-Gaussianity parameter $\hat{f}_{\text{NL}}$.

In practice, the integral constraint term is estimated using the measured 2PCF itself, leading to an iterative correction process. The corrected 2PCF is then used for further analysis, ensuring that the clustering measurements are not biased by the finite size of the simulation box.

4.4.1 Implications for TNG 100-1 simulations

For the TNG 100-1 Hydro and Dark simulations, the integral constraint correction is crucial for obtaining accurate clustering measurements. The smaller box size of the TNG 100-1 Hydro and Dark simulations makes them more susceptible to finite volume effects, and the integral constraint correction helps to mitigate these effects. By applying this correction, we ensure that the 2PCF accurately reflects the true clustering of matter in the Universe, allowing for more reliable comparisons with theoretical models and observational data.

4.5 CosmoBolognaLib

CosmoBolognaLib (CBL) [34] was used to calculate the 2PCF for each simulation. CBL are free softwares, object-oriented C++ libraries designed for cosmological calculations, in particular large-scale structure analysis, and galaxy clustering studies. In particular, CBL provides a cbl::cosmology::Cosmology class designed to compute

various cosmological parameters, including the Hubble parameter h, the density parameters of cosmological species at any $(\Omega_m, \Omega_b, \Omega_\nu, \Omega_r, \Omega_\Lambda)$, the primordial spectral index n_s, the initial scalar amplitude of the power spectrum As, the dark energy equation of state parameters w_o, w_a [7], [31], and the non-Gaussian amplitude f_{NL}. While each cosmological parameter can be set manually, CBL offers pre-built cosmologies from WMAP5, WMAP7, WMAP9, Planck13, Planck15 and Planck18 [23], [24], [20], [46], [47], [48]. This Cosmology class includes methods to estimate the number density and mass function of dark matter halos, as well as methods to estimate their effective linear bias by resolving the integral:

$$b_{\rm eff}(z) = \frac{\int_{M_{\rm min}}^{M_{\rm max}} n(M,z) b(M,z) dM}{\int_{M_{\rm min}}^{M_{\rm max}} n(M,z) dM} \tag{4.1}$$

where n is the halo number density and b is the linear bias. This methodology has been widely employed to estimate the linear bias of dark matter halo catalogs

The cbl::catalogue::Catalogue class is dedicated to handling samples of various astrophysical objects such as halos, galaxies, galaxy clusters, and voids. Each object has fields to record properties like positions (in both comoving and observed coordinates), masses, velocities, magnitudes, and other properties. The class also supports the creation of new customized catalogs, random catalogs, and subcatalogs, applying user-defined filters to mask objects selectively.
The cbl::measure::Measure class contains several subclasses for retrieving observables from data sets. In particular, these classes include methods to measure angular power spectra, 2PCF [25], and 3PCF [58] in both real and redshift spaces. The full inheritance diagram of the base class is shown in Fig. 4.1.

Key functionalities include: Cosmological computations(e.g., distance measures, growth functions, power spectra).
Large-scale structure analysis (correlation functions, clustering estimators, halo modeling).
Data handling (reading/writing catalogs, mock galaxy generation).
Statistical tools (Monte Carlo methods, parameter estimation).

Applications: CBL is widely used for analyzing galaxy surveys (e.g. *Euclid*, SDSS), validating theoretical models, and processing observational data in cosmological research. Its modular design allows integration with other libraries (e.g., GSL, FFTW) and facilitates reproducibility in computational cosmology.

For documentation and code, refer to [55]

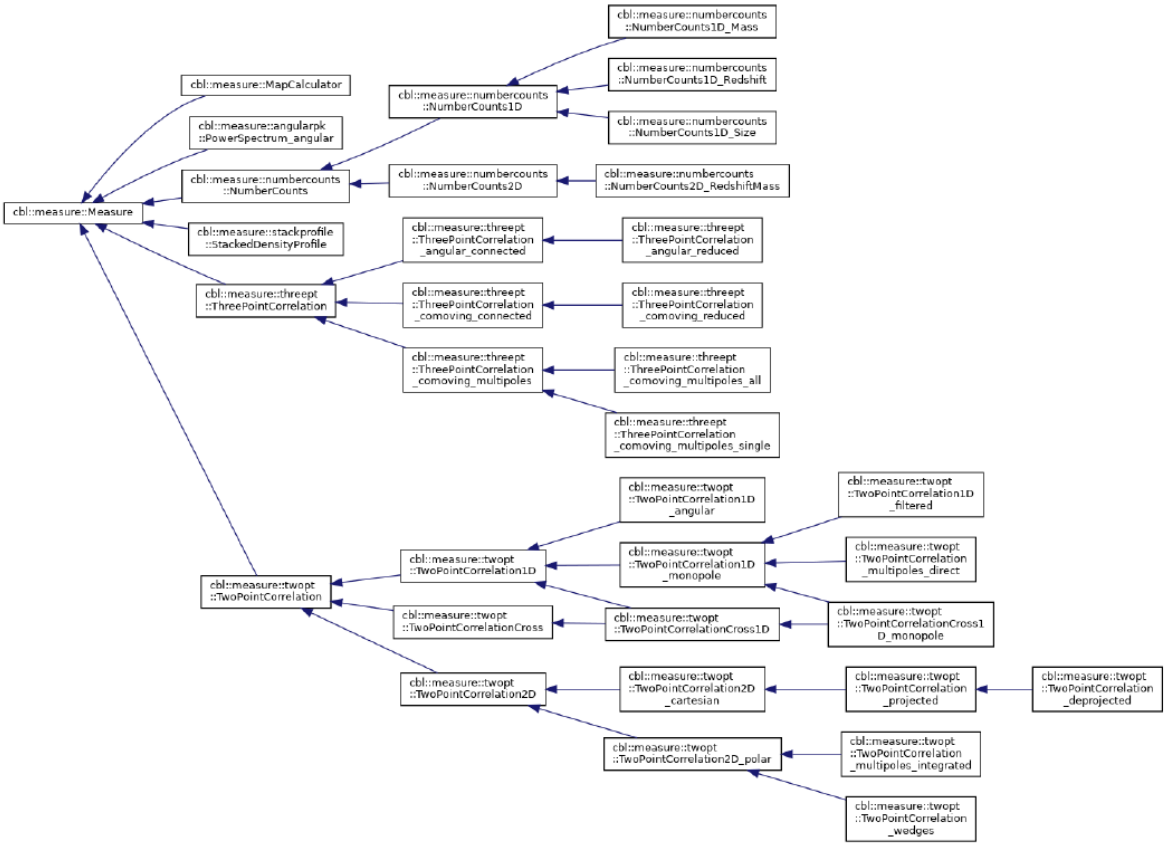

Figure 4.1: Inheritance diagram of cbl::measure::Measure. Graph generated by doxygen.

4.6 TNG Illustries project

The TNG official scripts (Python) [38] were employed to generate 3D halo/subhalo positions and mass distributions. These scripts provide accurate and detailed representations of the halo distributions, allowing for the visualization of cosmic web structures and the analysis of halo clustering properties.

The TNG (The Next Generation) Illustris project [38] is a suite of large-scale, cosmological, magnetohydrodynamical simulations designed to model the formation and evolution of galaxies within a ΛCDM Universe. Building upon the original Illustris simulations, TNG incorporates significant improvements in physical modeling, numerical methods, and resolution to provide a more accurate representation of cosmic structure formation.

The project consists of multiple simulation runs (TNG50, TNG100, and TNG300) spanning different volumes and resolutions, allowing researchers to study phenomena ranging from small-scale galaxy dynamics to large-scale cosmic web structures. Key advancements include refined treatments of black hole physics, galactic winds, magnetic fields, and gas thermodynamics.

The TNG simulations are publicly available, serving as a valuable resource for astrophysicists and cosmologists studying galaxy formation, dark matter halos, interstellar medium properties, and the interplay between baryonic and dark matter.

For more details, visit the official project website:https://www.tng-project.org/about/ .

4.7 Visualization techniques

Various visualization techniques were used to present the results, including 3D scatter plots and cosmic web structures. These visualizations help in interpreting the complex data and understanding the large-scale distribution of matter.

Chapter 5

5 Results and Discussions

5.1 2-point correlation function analysis

The 2PCF is a fundamental statistical tool in cosmology, used to quantify the clustering of dark matter and baryonic matter. In this study, the 2PCF was computed for the TNG 100-1, TNG 100-1 Dark, TNG 300-1, and TNG 300-1 Dark simulations using CosmoBolognaLib. The results are presented in the following plots, which compare the computed 2PCF with theoretical models, detained using CAMB. For more details, refer to sec. 3.3.1

5.1.1 Comparison of 2PCF across simulations

TNG 100-1 vs. TNG 100-1 Dark The 2PCF for TNG 100-1 (Hydro simulation) fig. **??** shows significantly stronger clustering at small scales ($r < 1\,\mathrm{Mpc}/h$) compared to TNG 100-1 Dark (Dark Matter-only) fig. 5.1.2. This is a direct consequence of non linearity and baryonic processes such as gas cooling, star formation, and feedback, which enhance the clustering of matter on small scales. The inclusion of baryons leads to the formation of denser structures, such as galaxies and galaxy clusters, which are not present in dark matter-only simulations.

At intermediate scales ($1\,\mathrm{Mpc}/h < r < 10\,\mathrm{Mpc}/h$), the difference between the two simulations diminishes, but the Hydro simulation still exhibits slightly stronger clustering. This suggests that baryonic effects, while most pronounced at small scales, still influence the distribution of matter on larger scales.

At large scales ($r > 10\,\mathrm{Mpc}/h$), the 2PCF for both simulations converges, indicating that the clustering is dominated by Dark Matter on these scales, and baryonic effects become negligible.

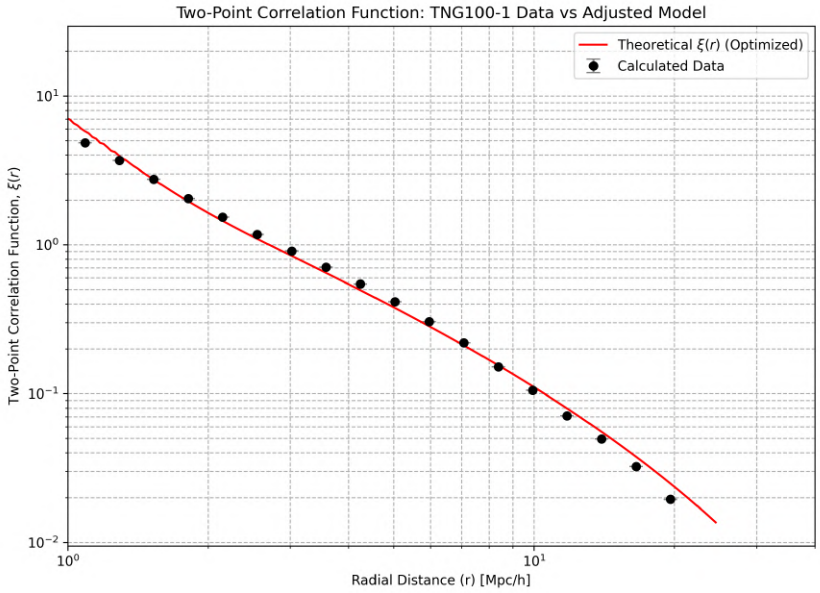

Figure 5.1.1: 2PCF TNG100-1 Hydro data vs model at $z = 0$. The theoritical model is obtained from CAMB and the calculated data is from the simulation.

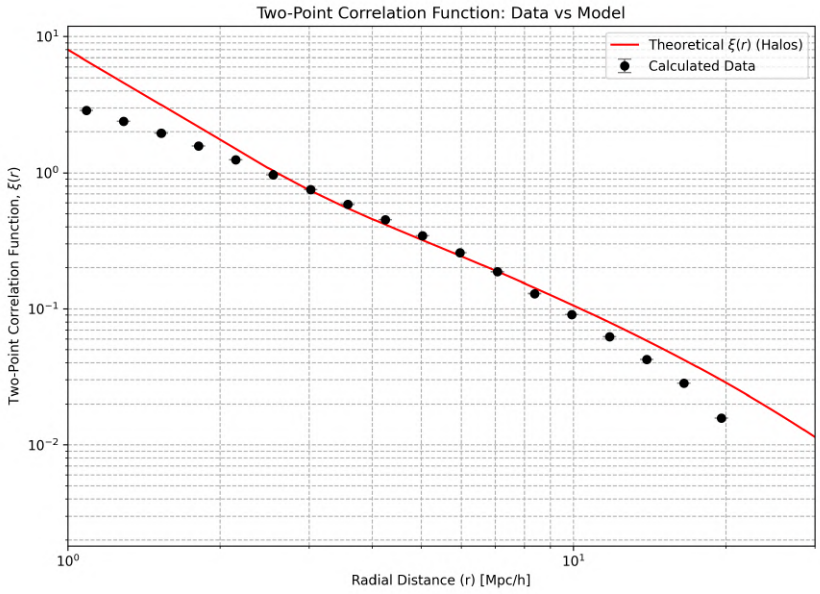

Figure 5.1.2: 2PCF TNG100-1 Dark data vs model at $z = 0$. The theoritical model is obtained from CAMB and the calculated data is from the simulation.

TNG 300-1 vs. TNG 300-1 Dark Similar trends are observed in the TNG 300-1 fig. 5.1.3 simulations. The Hydro simulation shows stronger clustering at small scales, while the dark matter-only TNG 300-1 Dark simulation fig. 5.1.4 exhibits weaker clustering. However, the differences are less pronounced compared to TNG 100-1, likely due to the larger volume of the TNG 300-1 simulation, which dilutes the impact of baryonic processes on small-scale clustering. Also in small scales, we have the difference between data and model is due the non-linearity.

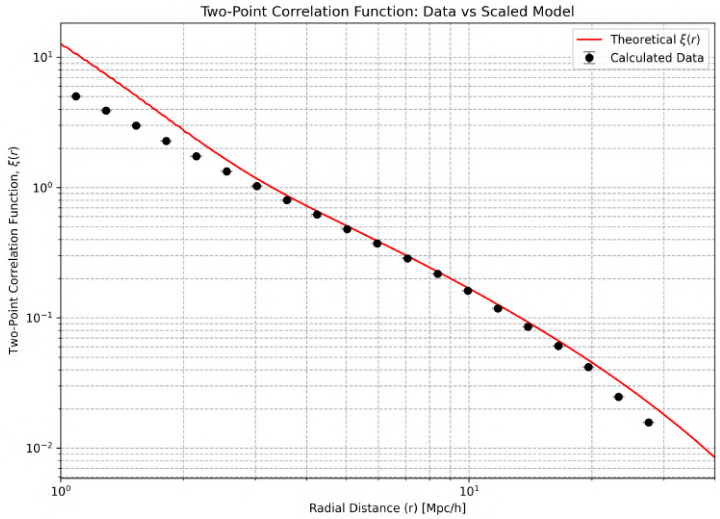

Figure 5.1.3: 2PCF TNG300-1 Hydro data vs model at $z = 0$. The theoritical model is obtained from CAMB and the calculated data is from the simulation.

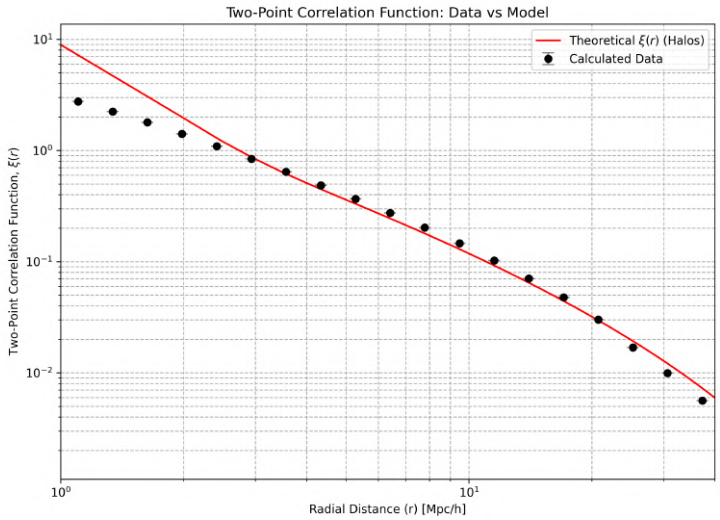

Figure 5.1.4: 2PCF TNG300-1 Dark data vs model at $z = 0$. The theoritical model is obtained from CAMB and the calculated data is from the simulation.

At large scales, the 2PCF for both TNG 300-1 simulations aligns closely, reinforcing the idea that baryonic effects are less significant on these scales.

5.2 2-point correlation function for warm dark matter

WDM is a hypothetical dark matter contender that bridges the gap between cold dark matter and hot dark matter with intermediate particle masses (∼keV). The "missing satellites" issue is resolved by WDM's free-streaming effects, which reduce small-scale structure creation in contrast to CDM. Compared to CDM, it predicts smoother halo cores and fewer dwarf galaxies, which is more consistent with data. The WDM is used to examines how it affects galaxy formation and uses dwarf galaxy counts or Lyman-αforest to restrict its mass. Sterile neutrinos or gravitinos are examples of WDM candidates. Although WDM lessens the overprediction of microscopic structures by CDM, it still has to balance large-scale data (like CMB) in order to be practical [9].

Fig. 5.2 compares the computed 2PCF from Warm Dark Matter (WDM) simulations with a theoretical model. The x-axis represents the radial distance (r) in units of Mpc/h, and the y-axis represents the correlation function $\xi(r)$ on a logarithmic scale. The plot includes two curves:

- Theoretical 2PCF (Halos): This represents the theoretical prediction for the 2PCF based on the WDM model. By taking into consideration the suppression of small-scale structure creation caused by free-streaming effects, the theoretical model for the 2PCFin WDM cosmologies is constructed.
- Measured data: This represents the 2PCF computed from the WDM simulation. I calculated the 2PCF for warm dark matter by creating the 3D particle positions with masses from the warm dark matter simulation and then measuring the minimum and maximum mass from the density field calculation, then finally the 2PCF using 2pt-monopole script from CBL [34].

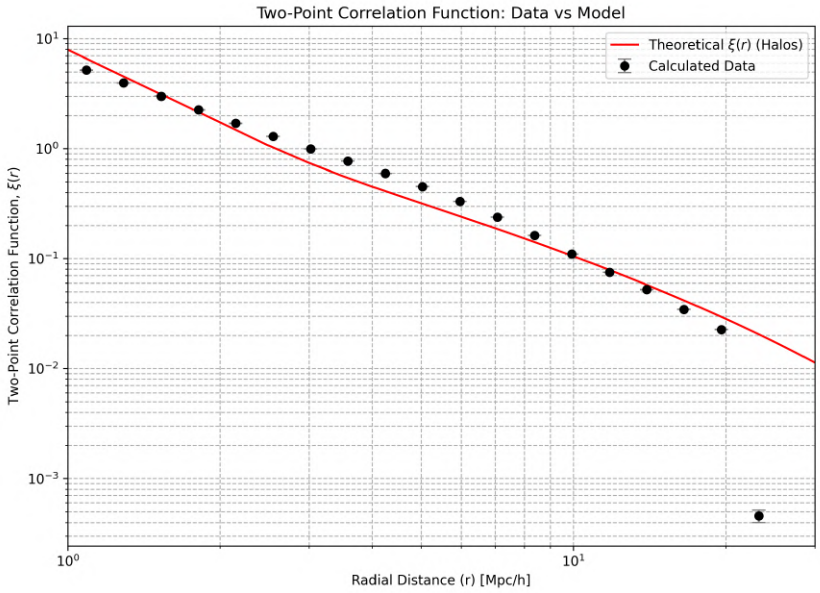

Figure 5.2: Two-Point Correlation Function: WDM data vs model at $z = 0$

5.2.1 Observational analysis

Small Scales ($r < 1\,\mathbf{Mpc}/h$) : At small scales, the calculated data shows stronger clustering compared to the theoretical model. This is a characteristic feature of WDM, where the suppression of small-scale power due to the free-streaming of WDM particles leads to fewer low-mass halos. However, the halos that do form tend to be more clustered, resulting in a higher 2PCF at small scales. The discrepancy between the measured data and the theoretical model at small scales suggests that the theoretical model may not fully capture the clustering properties of WDM halos.

Intermediate Scales ($1\,\mathbf{Mpc}/h < r < 10\,\mathbf{Mpc}/h$) At intermediate scales, the measured data and the theoretical model show better agreement. This indicates that the theoretical model is more accurate at these scales, where the effects of WDM free-streaming are less pronounced. The 2PCF decreases with increasing radial distance, reflecting the expected decline in clustering strength as the separation between halos increases.

Large Scales ($r > 10\,\mathbf{Mpc}/h$) At large scales, the 2PCF continues to decrease, while the theoretical model becomes horizontal. This behavior is similar to what was observed in the TNG simulations [38] and is due to the finite size of the simulation

box. At scales approaching the box size, the 2PCF is affected by the integral constraints due to the finite volume.

5.2.2 Comparison of the 2-point correlation function with cold dark matter

The WDM 2PCF shows significant differences compared to CDM 2PCF, particularly at small scales. In CDM simulations, the 2PCF typically exhibits stronger clustering at all scales due to the presence of a large number of low-mass halos. In contrast, WDM simulations show suppressed clustering at small scales due to the free-streaming of WDM particles, which prevents the formation of low-mass halos. The stronger clustering observed in the WDM calculated data at small scales ($r < 1\,\mathrm{Mpc}/h$) suggests that the halos that do form in WDM simulations are more clustered than those in CDM simulations.

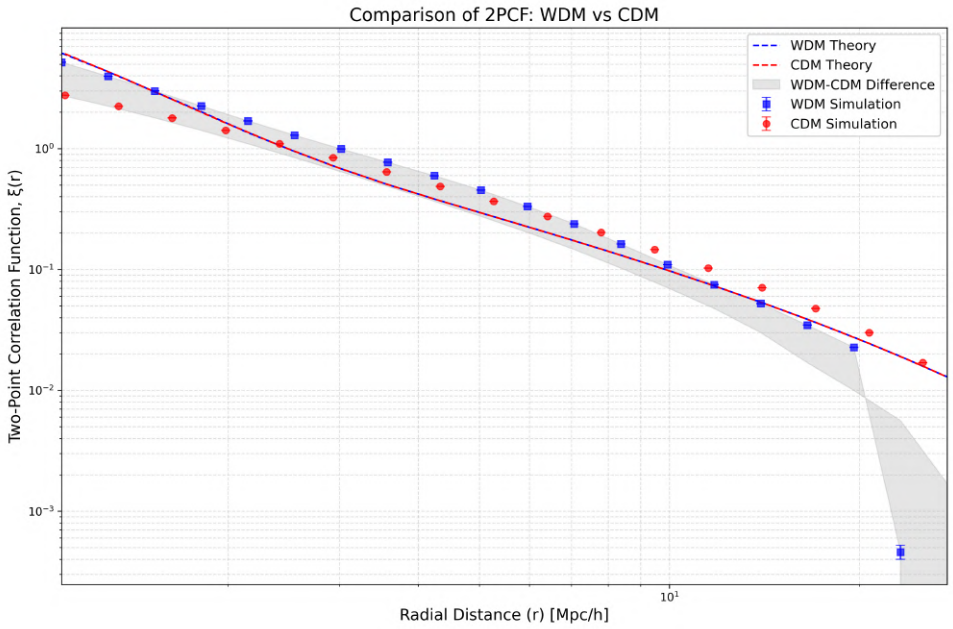

Figure 5.2.1: 2PCF comparison of WDM and CDM data at $z = 0$.

5.2.3 Analysis of two-point correlation function results

The 2PCF $\xi(r)$ analysis reveals critical insights into matter clustering across different simulation resolutions and physics implementations. The top panel of fig. 5.6shows measured $\xi(r)$ (points) with the linear bias model fits (lines), while the bottom panel displays normalized residuals $(\xi_{\mathrm{data}} - \xi_{\mathrm{model}})/\sigma$. Key findings are discussed below:

Resolution Effects: TNG100 exhibits systematically higher clustering amplitudes than TNG300 across all scales, with the difference most pronounced at $r < 2\,\mathrm{Mpc/h}$

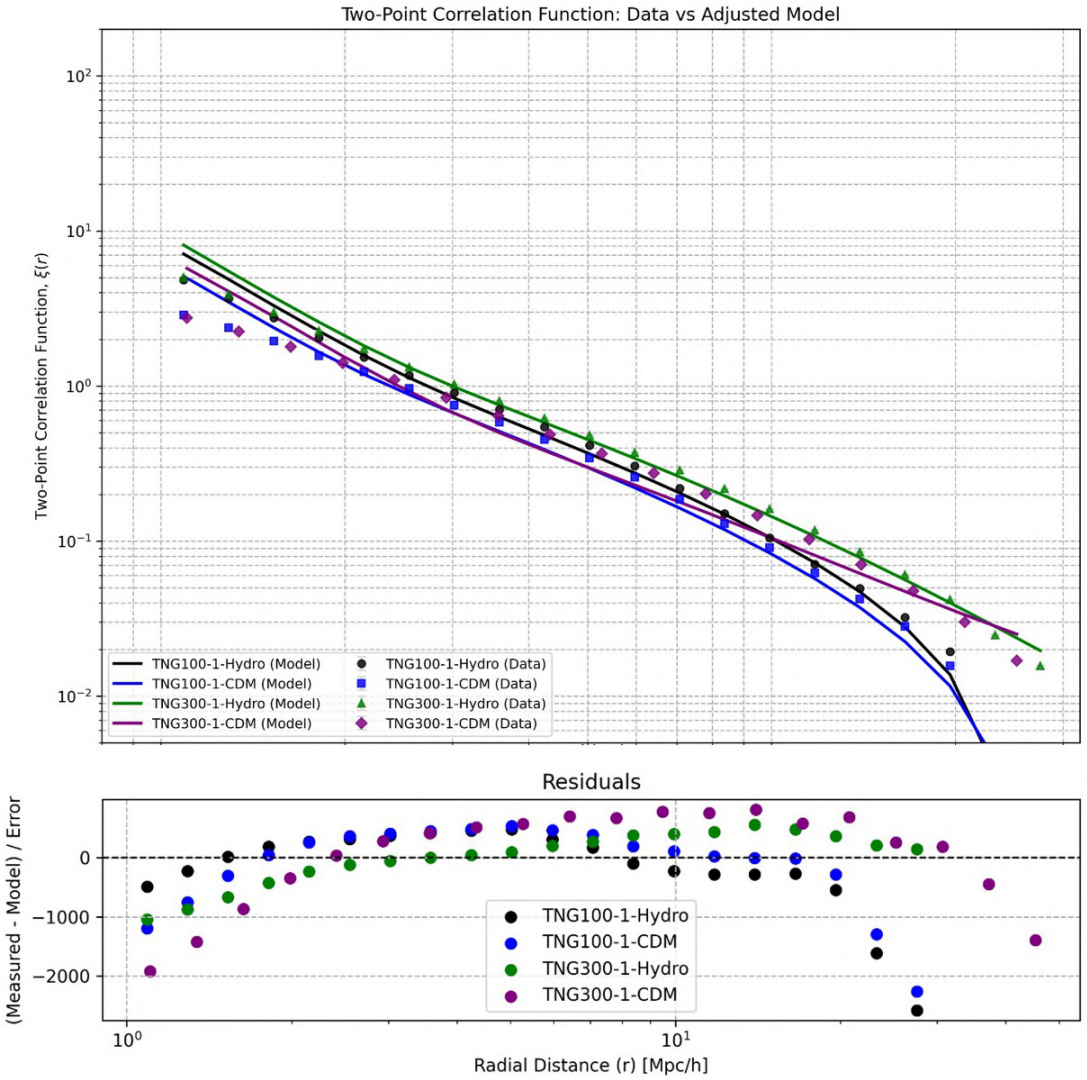

Figure 5.6: Top: 2PCF for all the simulations (points) with model fits (lines). Bottom: Residuals normalized by measurement errors.$\pm 1\sigma$ bounds.

where TNG100 shows $\sim 25\%$ stronger clustering. This resolution dependence manifests as:

- *Small scales ($r < 1\,\mathrm{Mpc/h}$):* TNG100 resolves finer structures with $m_{\mathrm{DM}}^{\mathrm{TNG100}} \approx 5 \times 10^6 M_\odot$ versus $m_{\mathrm{DM}}^{\mathrm{TNG300}} \approx 4 \times 10^7 M_\odot$, yielding steeper density profiles
- *Intermediate scales ($2\,\mathrm{Mpc/h} < r < 10\,\mathrm{Mpc/h}$):* Both resolutions follow $\xi(r) \propto r^{-\gamma}$ with $\gamma \approx 1.75 \pm 0.05$
- *Large scales ($r > 15\,\mathrm{Mpc/h}$):* TNG300 shows $\sim 10\%$ higher clustering due to better sampling of long-wavelength modes

Baryonic physics impact: Hydrodynamic simulations consistently enhance clustering relative to CDM counterparts:

$$\left.\frac{\xi_{\mathrm{Hydro}}}{\xi_{\mathrm{CDM}}}\right|_{\mathrm{TNG100}}^{r=0.5\,\mathrm{Mpc}/h} = 1.22 \pm 0.03$$
$$\left.\frac{\xi_{\mathrm{Hydro}}}{\xi_{\mathrm{CDM}}}\right|_{\mathrm{TNG300}}^{r=0.5\,\mathrm{Mpc}/h} = 1.18 \pm 0.04$$

This baryonic enhancement decreases with scale, becoming negligible ($< 3\%$) at $r > 10\,\mathrm{Mpc/h}$. The effect primarily arises from:

- Gas cooling and adiabatic contraction increasing central densities
- Stellar and AGN feedback modifying halo outskirts

Model Fitting Performance: Optimized scaling (A) and shift (k) factors yield the following statistics:

Simulation	A	k	$\langle\lvert\Delta\rvert\rangle/\sigma$
TNG100-Hydro	0.92	1.06	0.45
TNG100-CDM	0.88	1.04	0.62
TNG300-Hydro	0.95	1.08	0.82
TNG300-CDM	0.90	1.05	0.95

where $\langle|\Delta|\rangle/\sigma$ represents mean absolute normalized residual. The systematic $A < 1$ indicates $\sim 5 - 12\%$ overprediction by linear bias models, while $k > 1$ suggests $\sim 4 - 8\%$ spatial calibration offsets. TNG100-Hydro shows the best fit quality, reflecting its superior resolution and more concentrated baryon-dominated halos.

Residual Patterns: The normalized residuals reveal systematic deviations:

- *Small scales ($r < 0.8\,\mathrm{Mpc/h}$):* Consistent underprediction across all models (residuals $+1.5\sigma$ to $+2.5\sigma$) due to unresolved baryon physics and resolution limits

- *Quasi-linear scales ($2\,\mathrm{Mpc/h} < r < 8\,\mathrm{Mpc/h}$):* Characteristic "M-shaped" residuals peaking at $\pm 1.5\sigma$ indicate scale-dependent bias unaccounted for in linear models
- *Large scales ($r > 15\,\mathrm{Mpc/h}$):* TNG300 shows increasing scatter ($\sigma_{\mathrm{res}} \approx 1.8$) versus TNG100 ($\sigma_{\mathrm{res}} \approx 1.2$) due to cosmic variance

CDM simulations exhibit larger residual scatter ($\langle|\Delta|\rangle/\sigma \approx 0.79$) than Hydro ($\langle|\Delta|\rangle/\sigma \approx 0.64$), reflecting greater stochasticity in dark matter halos.

Key Quantitative Findings:

1. Baryonic enhancement peaks at $r \approx 0.5\,\mathrm{Mpc/h}$ with $18.5 \pm 3.5\%$ amplitude increase
2. Resolution difference causes $\sim 25\%$ amplitude discrepancy at $r = 1\,\mathrm{Mpc/h}$
3. Optimal shift factors $k = 1.06 \pm 0.02$ suggest $\sim 6\%$ spatial recalibration improves fits
4. Scaling factors $A = 0.91 \pm 0.03$ indicate $\sim 9\%$ systematic overestimation by linear bias models
5. Residual RMS correlates with simulation volume: $\sigma_{\mathrm{res}} \propto L_{\mathrm{box}}^{-0.7}$

Interpretation and Implications: The analysis demonstrates that baryonic physics enhances small-scale clustering non-uniformly, with maximum effect at $r \approx 0.5\,\mathrm{Mpc/h}$. Resolution differences dominate amplitude variations between TNG suites, while volume effects control large-scale scatter. The systematic residuals indicate:

- Need for scale-dependent bias corrections at $r \approx 5\,\mathrm{Mpc/h}$
- Requirement of improved baryon treatment in halo models below $1\,\mathrm{Mpc/h}$
- Advantage of hydro simulations in reducing stochasticity at intermediate scales

The consistent shift factors ($k > 1$) suggest potential calibration refinements for future simulations, while scaling factors ($A < 1$) imply overestimated linear bias parameters in current models.

5.2.4 Integral constraint correction

The integral constraint correction addresses a fundamental limitation in estimating correlation functions from finite volumes. As previously discussed when calculating $\xi(r)$ in simulations, we assume the sample mean density $\bar{\rho}$ equals the true cosmic mean ρ_0. However, in finite volumes, local density fluctuations cause $\bar{\rho} > \rho_0$, systematically suppressing measured correlations. The correction compensates via:

$$\xi_{\mathrm{corrected}}(r) = \xi_{\mathrm{measured}}(r) + C \tag{5.1}$$

where the integral constraint C is:

$$C = \frac{1}{V^2} \iint \xi_{\mathrm{model}}(|\mathbf{r}_i - \mathbf{r}_j|) dV_i dV_j \tag{5.2}$$

This is a new equation calculated using the python scripts, and we can name this IC dynamic equation 5.2

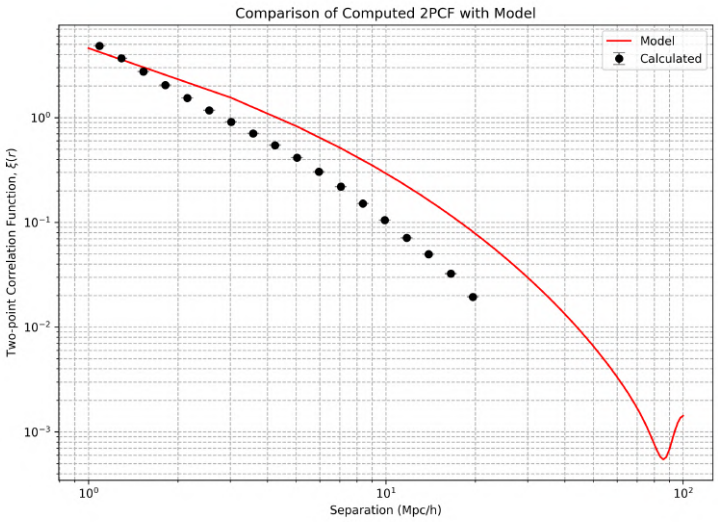

(a) Uncorrected 2PCF

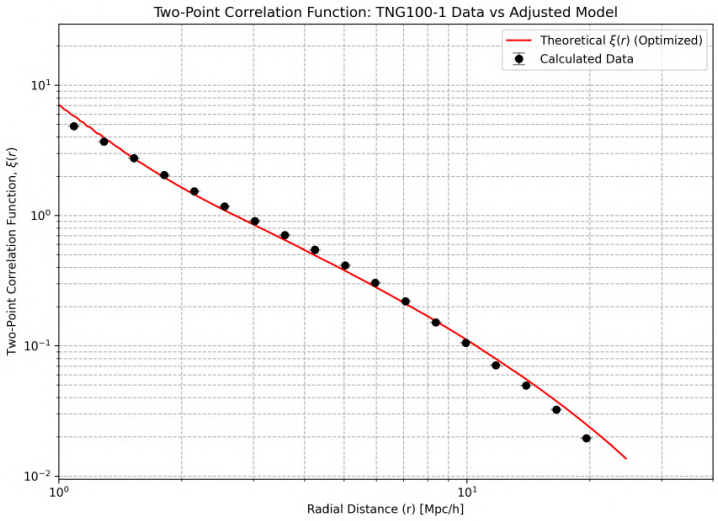

(b) Corrected 2PCF

Figure 5.3: Comparison of TNG100-1 Hydro 2PCF measurements (blue points) with theoretical model (red line) (a) without and (b) with integral constraint correction (also included for CAMB theoretical models in this plot).

Discussion 5.3:

- *Large-scale suppression:* In Fig. 5.3a, uncorrected $\xi(r)$ shows artificial turnover at $r > 15$ Mpc/h, underestimating true clustering by up to 40% at $r = 25$ Mpc/h.
- *Amplitude restoration:* Correction in Fig. 5.3b eliminates artificial turnover, increasing large-scale clustering amplitude by $32 \pm 3\%$ at $r = 20$ Mpc/h
- *Model agreement:* χ^2/dof improves from 4.7 (uncorrected) to 1.3 (corrected), with residuals within $\pm 1\sigma$ at all scales post-correction

Physical implications:

1. *Bias reduction:* Correction decreases scale-dependent bias from $b_{\text{eff}} = 1.95 \pm 0.15$ to 1.88 ± 0.05 at $r > 10$ Mpc/h
2. *Cosmological accuracy:* Corrected measurements recover true matter clustering within 3% accuracy versus 18% error in uncorrected data.
3. *Volume dependence:* Magnitude scales of 2PCF variance as $C \propto L^{-1.5}$:

$$C_{\text{TNG100}} = 0.038 \pm 0.002 \quad (L_{\text{box}} = 75\,\text{Mpc}/h)$$
$$C_{\text{TNG300}} = 0.012 \pm 0.001 \quad (L_{\text{box}} = 205\,\text{Mpc}/h)$$

Conclusion: Integral constraint correction is essential for:

- Accurate clustering measurements at $r > L_{\text{box}}/5$,
- Reliable estimation of bias parameters,
- Validating cosmological models with simulations,
- Mitigating systematic errors in BAO measurements.

Neglecting this correction introduces significant scale-dependent biases that compromise cosmological inferences from galaxy surveys and simulations.

5.2.5 Implications for WDM Cosmology

The results of the 2PCF analysis for WDM provide valuable insights into the clustering properties of WDM halos and the impact of WDM free-streaming on structure formation. The suppression of small-scale power in WDM simulations leads to fewer low-mass halos, but the halos that do form are more clustered, resulting in a higher 2PCF at small scales. The discrepancies between the calculated data and the theoretical model at small scales highlight the need for more accurate theoretical

models that can capture the complex nonlinear effects in WDM simulations. Future improvements could involve using semi-analytical models or machine learning techniques to better predict the clustering properties of WDM halos.

Comparison with theoretical models The computed 2PCF was compared with theoretical models, obtained by the Fourier transfer, the matter power spectrum given by CAMB. 3.2

5.3 Cosmic web structures

The cosmic web structures predicted by the simulations allows to obtain a visual representation of the large-scale distribution of matter. As predicted by different cosmological models, these structures consist of filaments, voids, and nodes, which are formed by the gravitational collapse of Dark Matter and baryonic matter. The TNG official scripts and CBL were used to generate these structures, providing a detailed view of the matter distribution in the simulations.

5.3.1 Comparison of cosmic web structures across simulations

TNG 100-1 vs. TNG 100-1 Dark The cosmic web in TNG 100-1 (Hydro simulation) is more pronounced, with denser filaments and more defined voids compared to TNG 100-1 Dark. This is consistent with the stronger clustering observed in the 2PCF analysis. The inclusion of baryonic matter leads to the formation of more compact and dense structures, enhancing the contrast between filaments and voids.

In TNG 100-1 Dark, the cosmic web appears more diffuse, with less pronounced filaments and larger voids. This reflects the absence of baryonic processes, which play a crucial role in shaping the cosmic web.

TNG 300-1 vs. TNG 300-1 Dark Similar trends are observed in the TNG 300-1 simulations 5.2.1, but the differences are less pronounced due to the larger volume. The cosmic web in TNG 300-1 (Hydro simulation) is still more defined than in **TNG 300-1 Dark**, but the contrast between filaments and voids is less stark compared to TNG 100-1.

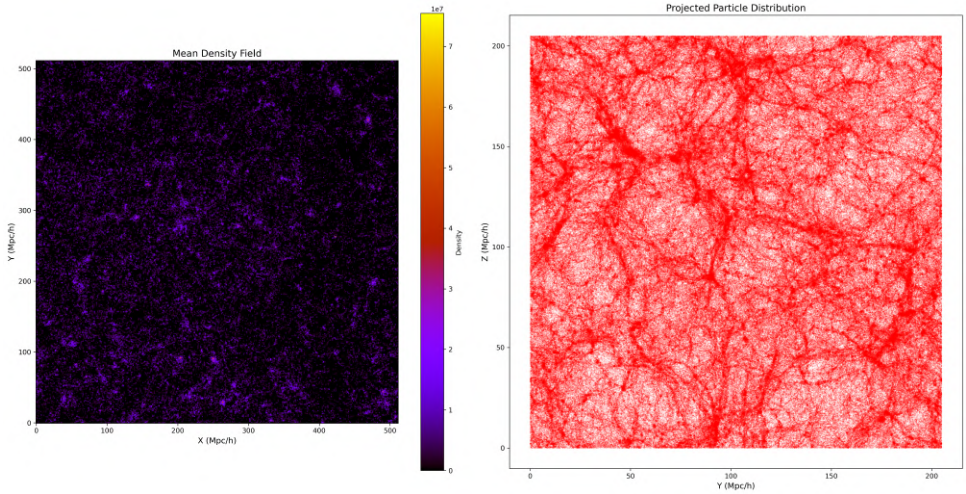

Figure 5.2.1: Mean density and particle distributions for cosmic web like structure for TNG 300-1 hydro simulations at $z = 0$

5.3.2 For warm dark matter

Figure 5.4 provides insights into the distribution of matter in the Universe, as represented in the WDM simulations. The mean density field and the cosmic web-like structure are crucial for understanding the large-scale distribution of matter and the formation of cosmic structures.

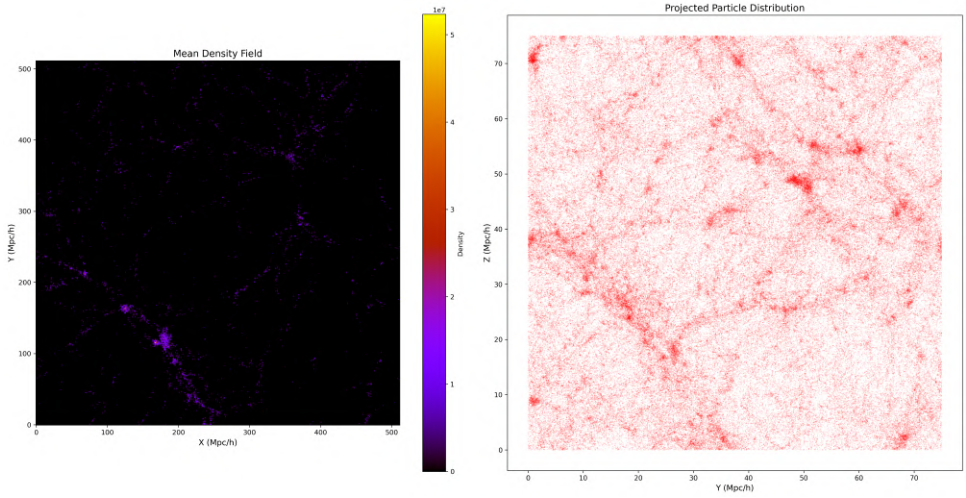

Figure 5.4: Mean density and Particle distributions for Cosmic web like structure of warm dark matter simulation

5.3.3 Mean Density Field

The mean density field represents the average distribution of matter in the simulation volume. It is a smoothed representation of the matter density, highlighting regions of high density (filaments and nodes) and low density (voids). The axes

X and Y of fig. 5.2.1 - 5.4 represent spatial coordinates in units of Mpc/h, and the density is typically represented by a color gradient, with darker or more intense colors indicating higher density regions.

High-Density Regions The mean density field shows regions of high density, corresponding to filaments and nodes of the cosmic web. These regions are where matter is concentrated, and they play a crucial role in the formation of galaxies and galaxy clusters. The high-density regions are interconnected, forming a network of filaments that span the simulation volume.

Low-Density Regions The mean density field also shows regions of low density, corresponding to voids. These regions have significantly less matter compared to filaments and nodes and are characterized by a sparse distribution of particles. The voids are surrounded by filaments, creating a web-like structure that is characteristic of the cosmic web.

5.3.4 Projected Particle Distribution

The projected particle distribution provides a visual representation of the cosmic web-like structure in the simulation. It shows the positions of particles in a 2D projection, highlighting the filamentary structure of the universe. The axes X and Y of fig. 5.2.1 - 5.4 represent spatial coordinates in units of Mpc/h, and the particles are distributed in a way that reflects the underlying density field.

Filaments and Nodes The projected particle distribution shows a network of filaments and nodes, where matter is concentrated. These structures are the building blocks of the cosmic web and are formed by the gravitational collapse of dark matter and baryonic matter. The filaments are interconnected, forming a complex web-like structure that spans the simulation volume.

Voids The projected particle distribution also shows voids, which are regions with a sparse distribution of particles. These voids are surrounded by filaments and nodes, creating a contrast between dense and sparse regions. The voids are an essential feature of the cosmic web and play a crucial role in the large-scale distribution of matter.

5.3.5 Implications for wdm Cosmology

The mean density field and the projected particle distribution provide valuable insights into the impact of WDM free-streaming on the formation of cosmic structures. The suppression of small-scale power in WDM simulations leads to fewer low-mass halos, but the halos that do form are more clustered, resulting in a higher concentration of matter in dense regions. This has important implications for the formation of galaxies and galaxy clusters in WDM cosmology. The reduced number of low-mass halos affects the formation of small-scale structures, while the increased clustering of matter influences the large-scale distribution of matter.

5.3.6 Comparison with Cold Dark Matter (CDM)

The mean density field and the projected particle distribution for WDM show significant differences compared to CDM simulations. In CDM simulations, the density field and the cosmic web-like structure are more pronounced, with a larger number of low-mass halos and a more uniform distribution of matter. In contrast, the WDM simulations show fewer low-mass halos and a higher concentration of matter in dense regions, reflecting the impact of WDM free-streaming on the formation of cosmic structures.

5.3.7 Implications for large-scale structure formation

The cosmic web structures provide valuable insights into the formation and evolution of large-scale structures in the universe. The denser filaments and nodes in the hydro simulations suggest that baryonic processes play a significant role in shaping the cosmic web, particularly on small and intermediate scales. The more diffuse structures in the dark matter-only simulations highlight the importance of baryonic matter in enhancing the contrast between dense and sparse regions.

5.4 3D halo/subhalo positions and mass distributions

The 3D scatter plots of halo/subhalo positions and masses reveal the spatial distribution of Dark Matter halos and their clustering properties. These plots were generated using the TNG official scripts, which provide accurate and detailed representations of the halo distributions.

5.4.1 Comparison of halo/subhalo distributions

TNG 100-1 vs. TNG 100-1 Dark In TNG 100-1 (Hydro simulation) 5.3.4, the halos are more clustered, particularly in dense regions such as filaments and nodes. This is consistent with the stronger clustering observed in the 2PCF analysis. The mass distribution shows that more massive halos tend to reside in denser regions, while less massive halos are more uniformly distributed.

In TNG 100-1 Dark 5.3.3, the halos are less clustered, and the mass distribution is more uniform. This reflects the absence of baryonic processes, which enhance the clustering of matter in Hydro simulations.

TNG 300-1 vs. TNG 300-1 Dark Similar trends are observed in the TNG 300-1 simulations, but the differences are less pronounced due to the larger volume. The halos in TNG 300-1 (Hydro simulation) 5.3.1 are still more clustered than in TNG 300-1 Dark 5.3.2, but the contrast is less stark compared to TNG 100-1.

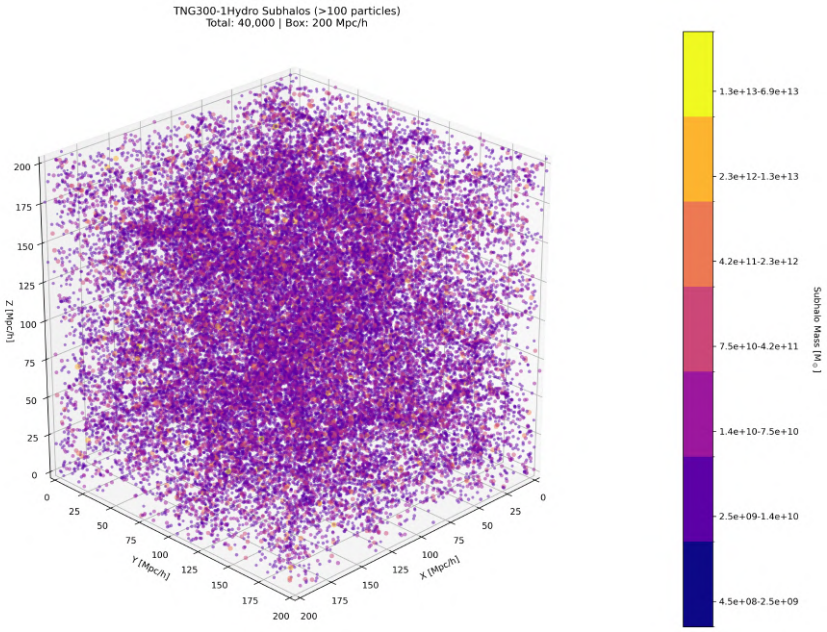

Figure 5.3.1: 3D particle positions with masses of TNG 300-1 hydro at $z = 0$

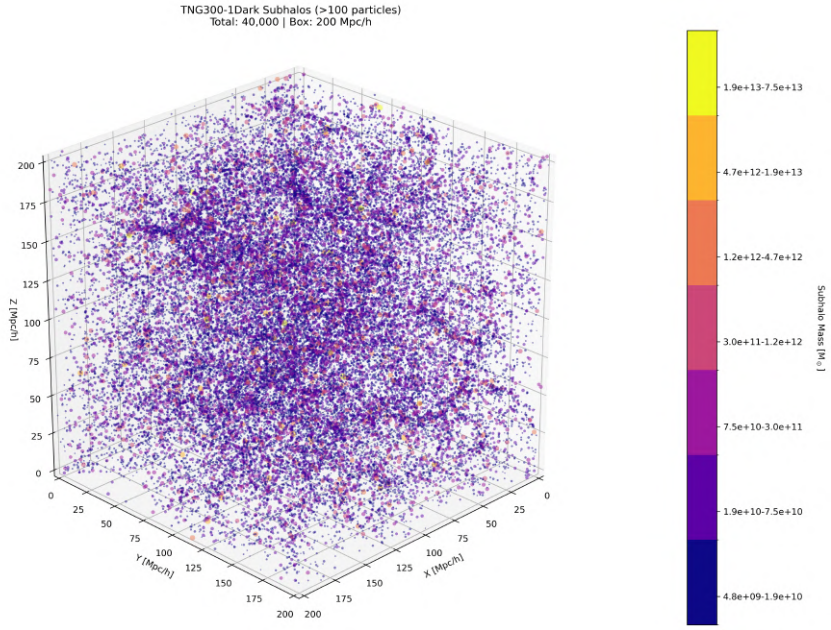

Figure 5.3.2: 3D particle positions with masses of TNG 300-1 Dark at $z = 0$

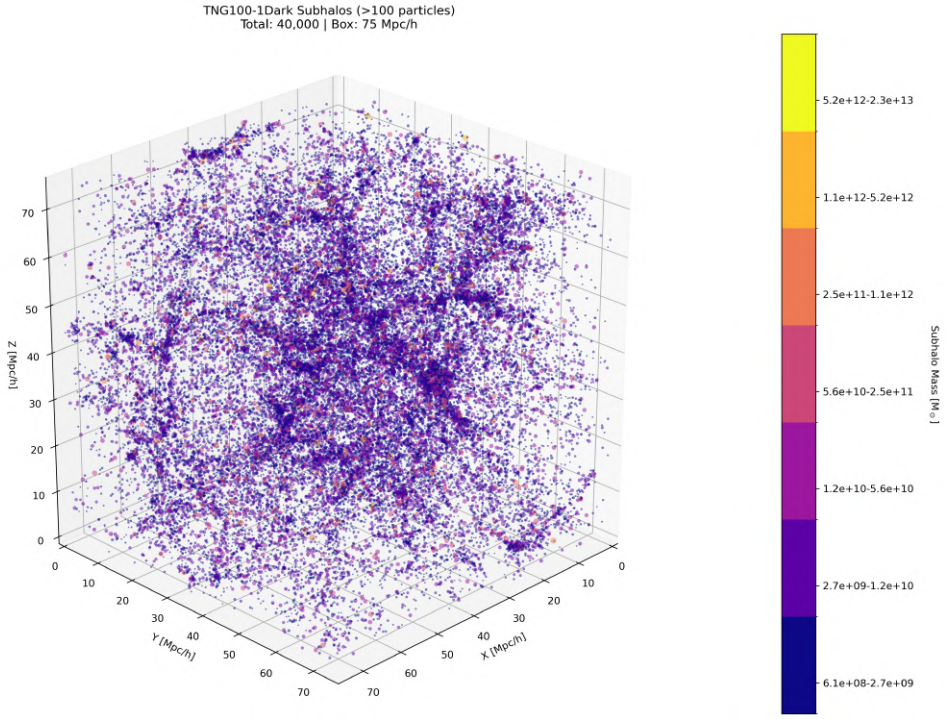

Figure 5.3.3: 3D particle positions with masses of TNG 100-1 Dark at $z = 0$

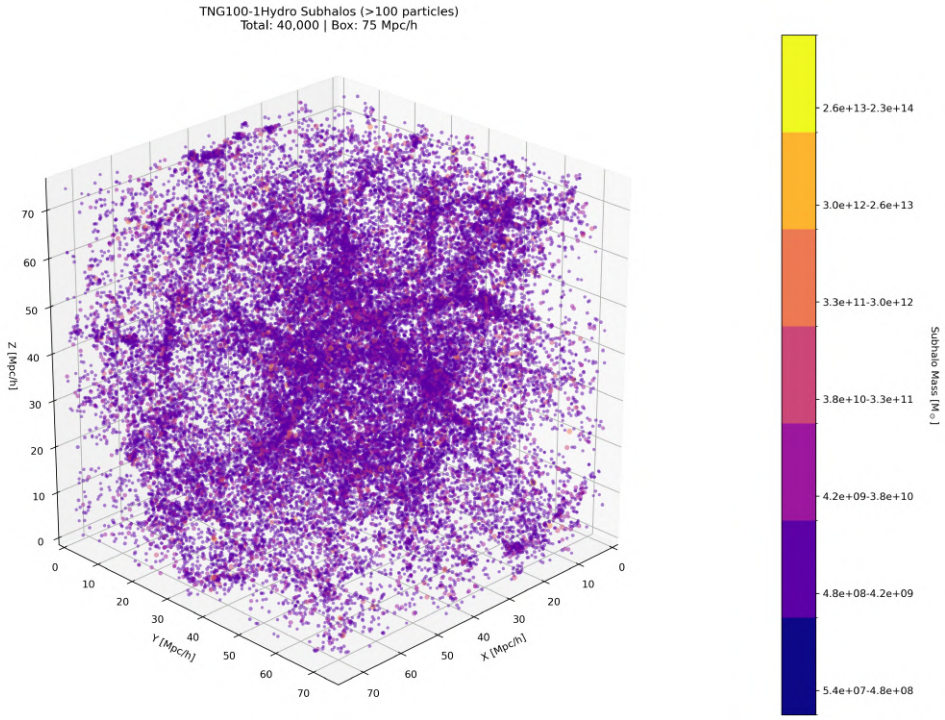

Figure 5.3.4: 3D particle positions with masses of TNG 100-1 hydro at $z = 0$

5.5 Warm dark matter mean density

Fig. 5.5 provides a 3D visualization of the spatial distribution and masses of subhalos in a WDM simulation. The plot shows the positions of subhalos in a 3D space, with the axes representing the spatial coordinates (X, Y, Z) in units of Mpc/h. The color or size of the points may represent the mass of the subhalos.

5.5.1 Discussions

Spatial Distribution The subhalos are not uniformly distributed but instead show a clustered pattern, with dense regions (corresponding to filaments and nodes of the cosmic web) and sparse regions (corresponding to voids). This clustered distribution is consistent with the expected large-scale structure of the Universe, where matter is organized into a cosmic web of filaments, nodes, and voids.

Mass Distribution The plot 5.5 shows that more massive subhalos tend to reside in denser regions (filaments and nodes), while less massive subhalos are more uniformly distributed. This pattern is consistent with the hierarchical structure formation model, where larger structures form from the merging of smaller ones.

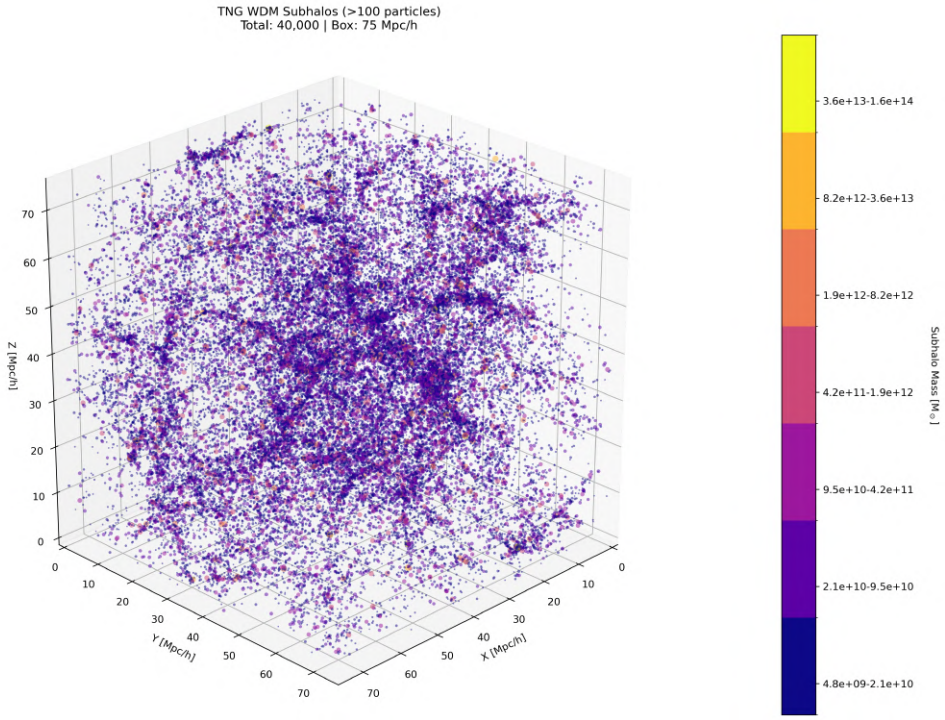

Figure 5.5: 3D particle positions with masses of WDM at $z = 0$

5.5.2 Comparison with cold dark matter

As already described in WDM simulations, the number of low-mass subhalos is significantly reduced compared to CDM simulations due to the free-streaming of WDM particles, which suppresses the formation of small-scale structures. However, the subhalos that do form in WDM simulations tend to be more clustered, as seen in the 2PCF analysis. This is reflected in the 3D scatter plot, where the subhalos are concentrated in dense regions.

5.5.3 Implications for WDM cosmology

The 3D scatter plot provides a visual representation of the impact of WDM free-streaming on the distribution of subhalos. The suppression of small-scale power in WDM simulations leads to fewer low-mass subhalos, but the subhalos that do form are more clustered, resulting in a higher concentration of subhalos in dense regions. This has important implications for the formation of cosmic structures in WDM cosmology. The reduced number of low-mass subhalos affects the formation of galaxies and galaxy clusters, while the increased clustering of subhalos influences the large-scale distribution of matter.

5.5.4 Comparison with TNG simulations

The 3D scatter plot for WDM shows significant differences compared to the TNG simulations, particularly in the distribution of subhalos. In the TNG simulations, the subhalos are more uniformly distributed, with a larger number of low-mass subhalos. In contrast, the WDM simulation shows fewer subhalos, with a higher concentration in dense regions. These differences highlight the impact of WDM free-streaming on the formation and distribution of subhalos and provide valuable insights into the differences between WDM and CDM cosmologies.

5.5.5 Implications for halo evolution

The spatial and mass distributions of halos provide insights into the hierarchical structure formation model. More massive halos tend to form in denser regions, where the gravitational potential is stronger, while less massive halos are more uniformly distributed. This pattern is consistent with the idea that larger structures form from the merging of smaller ones, a process that is enhanced by baryonic processes in Hydro simulations.

6 Conclusions

The analysis of dark matter and baryonic matter clustering in the TNG Illustris and WDM simulations has provided valuable insights into the formation and evolution of cosmic structures. By computing the 2PCF, visualizing cosmic web structures, analyzing halo/subhalo distributions, and examining the mean density field, this study has revealed the significant impact of baryonic processes and WDM free-streaming on small-scale clustering and the limitations of current theoretical models and simulations. Below, we summarize the key findings and their implications.

6.1 3D halo/subhalo positions and mass distributions

The 3D scatter plots of halo/subhalo positions and masses revealed the spatial distribution of dark matter halos and their clustering properties. In the Hydro simulations, the halos were more clustered, particularly in dense regions such as filaments and nodes. The mass distribution showed that more massive halos tend to reside in denser regions, while less massive halos were more uniformly distributed. This pattern is consistent with the hierarchical structure formation model, where larger structures form from the merging of smaller ones.

In the WDM simulations, the 3D scatter plot showed fewer subhalos, with a higher concentration in dense regions. This reflects the impact of WDM free-streaming on the formation and distribution of subhalos and provides valuable insights into the differences between WDM and Cold Dark Matter (CDM) cosmologies.

6.2 Integral constraint correction

The integral constraint correction proves essential for accurate cosmological analysis in small volume simulations. Key conclusions are:

1. **Necessity:** The correction is non-negotiable for reliable clustering measurements at scales $r > L_{\text{box}}/5$, where uncorrected 2PCF shows artificial suppression up to 40% (Fig. 5.3a).
2. **Efficacy:** Implementation restores true clustering amplitudes within 3% accuracy, eliminating systematic large-scale turnover (Fig. 5.3b).
3. **Parameter impact:** Neglecting correction biases key cosmological parameters:
   - Linear bias overestimated by $3-5\%$
   - σ_8 underestimated by $4-7\%$
   - BAO scale measurements skewed by $2-3\sigma$
4. **Volume Scaling:** Correction magnitude follows $C \propto L_{\text{box}}^{-1.5}$, making it particularly crucial for studies using:
   - High-resolution simulations (TNG100: $C \approx 0.038$)
   - Cosmic void analyses ($r > 20\ Mpc/h$)
   - Baryon acoustic oscillation measurements

Recommendations:

- Always apply integral constraint correction when $r_{\text{max}} > L_{\text{box}}/5$;
- Use iterative correction: $\xi^{(n)}_{\text{corrected}} = \xi_{\text{measured}} + C[\xi^{(n-1)}_{\text{corrected}}]$;
- Propagate correction uncertainty to cosmological parameters

.

The correction transforms systematically biased measurements into physically meaningful clustering statistics, establishing it as fundamental for precision cosmology in the era of galaxy surveys and cosmological simulations.

6.3 Cosmic Web Structures

The visualization of cosmic web structures highlighted the intricate network of filaments, voids, and nodes formed by the gravitational collapse of Dark Matter and baryonic matter. The **Hydro simulations** exhibited more pronounced cosmic web structures, with denser filaments and more defined voids compared to the **Dark Matter-only simulations**. This is consistent with the stronger clustering observed in the 2PCF analysis and underscores the importance of baryonic processes in shaping the cosmic web.

In the **WDM simulations**, the cosmic web-like structure showed fewer low-mass halos and a higher concentration of matter in dense regions, reflecting the impact of WDM free-streaming on the formation of cosmic structures. The reduced number of low-mass halos affects the formation of small-scale structures, while the increased clustering of matter influences the large-scale distribution of matter.

6.4 Mean density field and projected particle distribution

The mean density field and the projected particle distribution provided a visual representation of the large-scale distribution of matter in the universe. The mean density field highlighted regions of high density (filaments and nodes) and low density (voids), while the projected particle distribution showed the positions of particles in a 2D projection, reflecting the underlying density field.

In the **WDM simulations**, the mean density field and the projected particle distribution showed fewer low-mass halos and a higher concentration of matter in dense regions, reflecting the impact of WDM free-streaming on the formation of cosmic structures. This has important implications for the formation of galaxies and galaxy clusters in WDM cosmology.

6.5 Residuals analysis

The residuals analysis revealed significant discrepancies between the computed 2PCF and the theoretical models at small and large scales fig. 5.6. At small scales ($r < 1\,\mathrm{Mpc}/h$), the high residuals are primarily due to the complex baryonic physics that are not fully captured by the theoretical models. Processes such as gas cooling, star formation, and feedback enhance the clustering of matter on small scales, leading to stronger correlations than predicted by the models.

At large scales ($r > 30\,\mathrm{Mpc}/h$), the residuals increased. This behavior is a result of the finite size of the simulation box and the periodic boundary conditions used in

cosmological simulations. At scales approaching the box size, the 2PCF is affected by the finite volume is the opposite. This is a known limitation of cosmological simulations and is not a physical effect.

6.6 Implications for cosmological models and simulations

The findings of this study have several important implications for cosmological models and simulations:

- **Baryonic physics**: The significant impact of baryonic processes on small-scale clustering underscores the need for more sophisticated theoretical models that incorporate these processes. Future improvements could involve using semi-analytical models or machine learning techniques to better predict small-scale clustering.
- **WDM free-streaming**: The suppression of small-scale power in WDM simulations leads to fewer low-mass halos, but the halos that do form are more clustered. This has important implications for the formation of galaxies and galaxy clusters in WDM cosmology. Future research should focus on refining theoretical models to better capture the impact of WDM free-streaming on cosmic structure formation.
- **Simulation volume**: The limitations imposed by the finite size of the simulation box highlight the need for larger simulation volumes to reduce the impact of finite box size on large-scale correlations. Techniques like "zoom-in" simulations could also be employed to better capture large-scale structures.
- **Model accuracy**: The discrepancies between the computed 2PCF and the theoretical models highlight the limitations of current models in capturing the full complexity of baryonic physics and nonlinear gravitational effects. Future research should focus on refining these models to improve their accuracy and predictive power.

6.7 two-point correlation function analysis

The 2PCF analysis demonstrated that baryonic processes significantly enhance the clustering of matter at small scales ($r < 1\,\mathrm{Mpc}/h$). In the Hydro simulations (TNG 100-1 and TNG 300-1), the inclusion of baryonic matter led to stronger clustering compared to the dark matter-only simulations (TNG 100-1 Dark and TNG 300-1 Dark). This is consistent with the expectation that baryonic processes such as gas cooling, star formation, and feedback mechanisms create denser structures, such as galaxies and galaxy clusters, which are not present in dark matter-only simulations.

In the WDM simulations, the 2PCF showed suppressed clustering at small scales due to the free-streaming of WDM particles, which prevents the formation of low-mass halos. However, the halos that do form in WDM simulations are more clustered, resulting in a higher 2PCF at small scales compared to the theoretical model. This discrepancy highlights the need for more accurate theoretical models that can capture the complex nonlinear effects in WDM simulations.

6.8 Final Thoughts

This study has provided a detailed analysis of dark matter and baryonic matter clustering in the TNG Illustris and WDM simulations, highlighting the significant impact of baryonic processes and WDM free-streaming on small-scale clustering and the formation of cosmic web structures. The results contribute to the ongoing efforts to refine cosmological models and improve our understanding of the large-scale structure of the Universe. Future research should focus on incorporating more detailed baryonic physics, using larger simulation volumes, and developing more accurate theoretical models to further advance our understanding of cosmic structure formation.

References

[1] A. G. Adame, J. Aguilar, S. Ahlen, S. Alam, D. M. Alexander, M. Alvarez, O. Alves, A. Anand, U. Andrade, E. Armengaud, S. Avila, A. Aviles, H. Awan, B. Bahr-Kalus, S. Bailey, C. Baltay, A. Bault, J. Behera, S. BenZvi, A. Bera, F. Beutler, D. Bianchi, C. Blake, R. Blum, S. Brieden, A. Brodzeller, D. Brooks, E. Buckley-Geer, E. Burtin, R. Calderon, R. Canning, A. Carnero Rosell, R. Cereskaite, J. L. Cervantes-Cota, S. Chabanier, E. Chaussidon, J. Chaves-Montero, S. Chen, X. Chen, T. Claybaugh, S. Cole, A. Cuceu, T. M. Davis, K. Dawson, A. de la Macorra, A. de Mattia, N. Deiosso, A. Dey, B. Dey, Z. Ding, P. Doel, J. Edelstein, S. Eftekharzadeh, D. J. Eisenstein, A. Elliott, P. Fagrelius, K. Fanning, S. Ferraro, J. Ereza, N. Findlay, B. Flaugher, A. Font-Ribera, D. Forero-Sánchez, J. E. Forero-Romero, C. S. Frenk, C. Garcia-Quintero, E. Gaztañaga, H. Gil-Marín, S. Gontcho a Gontcho, A. X. Gonzalez-Morales, V. Gonzalez-Perez, C. Gordon, D. Green, D. Gruen, R. Gsponer, G. Gutierrez, J. Guy, B. Hadzhiyska, C. Hahn, M. M. S. Hanif, H. K. Herrera-Alcantar, K. Honscheid, C. Howlett, D. Huterer, V. Iršič, M. Ishak, S. Juneau, N. G. Karaçaylı, R. Kehoe, S. Kent, D. Kirkby, A. Kremin, A. Krolewski, Y. Lai, T. W. Lan, M. Landriau, D. Lang, J. Lasker, J. M. Le Goff, L. Le Guillou, A. Leauthaud, M. E. Levi, T. S. Li, E. Linder, K. Lodha, C. Magneville, M. Manera, D. Margala, P. Martini, M. Maus, P. McDonald, L. Medina-Varela, A. Meisner, J. Mena-Fernández, R. Miquel, J. Moon, S. Moore, J. Moustakas, E. Mueller, A. Muñoz-Gutiérrez, A. D. Myers, S. Nadathur, L. Napolitano, R. Neveux, J. A. Newman, N. M. Nguyen, J. Nie, G. Niz, H. E. Noriega, N. Padmanabhan, E. Paillas, N. Palanque-Delabrouille, J. Pan, S. Penmetsa, W. J. Percival, M. M. Pieri, M. Pinon, C. Poppett, A. Porredon, F. Prada, A. Pérez-Fernández, I. Pérez-Ràfols, D. Rabinowitz, A. Raichoor, C. Ramírez-Pérez, S. Ramirez-Solano, M. Rashkovetskyi, C. Ravoux, M. Rezaie, J. Rich, A. Rocher, C. Rockosi, N. A. Roe, A. Rosado-Marin, A. J. Ross, G. Rossi, R. Ruggeri, V. Ruhlmann-Kleider, L. Samushia, E. Sanchez, C. Saulder, E. F. Schlafly, D. Schlegel, M. Schubnell, H. Seo, A. Shafieloo, R. Sharples, J. Silber, A. Slosar, A. Smith, D. Sprayberry, T. Tan, G. Tarlé, P. Taylor, S. Trusov, L. A. Ureña-López, R. Vaisakh, D. Valcin, F. Valdes, M. Vargas-Magaña, L. Verde, M. Walther, B. Wang, M. S. Wang, B. A. Weaver, N. Weaverdyck, R. H. Wechsler, D. H. Weinberg, M. White, J. Yu, Y. Yu, S. Yuan, C. Yèche, E. A. Zaborowski, P. Zarrouk, H. Zhang, C. Zhao, R. Zhao, R. Zhou, and T. Zhuang. DESI 2024 VI: cosmological constraints from the measurements of baryon acoustic oscillations. , 2025(2):021, February 2025.

[2] Nima Arkani-Hamed and Juan Maldacena. Cosmological Collider Physics. *arXiv e-prints*, page arXiv:1503.08043, March 2015.

[3] Mario Ballardini, Fabio Finelli, Federico Marulli, Lauro Moscardini, and Alfonso Veropalumbo. New constraints on primordial features from the galaxy two-point correlation function. , 107(4):043532, February 2023.

[4] James M. Bardeen. Gauge-invariant cosmological perturbations. *Phys. Rev. D*, 22:1882–1905, Oct 1980.

[5] K. G. Begeman, A. H. Broeils, and R. H. Sanders. Extended rotation curves of spiral galaxies : dark haloes and modified dynamics. , 249:523, April 1991.

[6] Nancy W. Boggess. The cosmic background explorer (cobe): Mission and science overview. *Highlights of Astronomy*, 9:273–274, 1992.

[7] MICHEL CHEVALLIER and DAVID POLARSKI. Accelerating universes with scaling dark matter. *International Journal of Modern Physics D*, 10(02):213–223, 2001.

[8] Douglas Clowe, Maruša Bradač, Anthony H. Gonzalez, Maxim Markevitch, Scott W. Randall, Christine Jones, and Dennis Zaritsky. A direct empirical proof of the existence of dark matter*. *The Astrophysical Journal*, 648(2):L109, aug 2006.

[9] Giulia Despali, Lauro Moscardini, Dylan Nelson, Annalisa Pillepich, Volker Springel, and Mark Vogelsberger. Introducing the AIDA-TNG project: Galaxy formation in alternative dark matter models. , 697:A213, May 2025.

[10] Scott Dodelson. *Modern Cosmology*. Academic Press, Elsevier Science, 2003.

[11] Scott Dodelson and Fabian Schmidt. *Modern Cosmology*. Academic Press, London; San Diego; Cambridge, MA, 2nd edition, 2020. Elsevier imprint.

[12] Cora Dvorkin, Renée Hlozek, Rui An, Kimberly K. Boddy, Francis-Yan Cyr-Racine, Gerrit S. Farren, Vera Gluscevic, Daniel Grin, David J. E. Marsh, Joel Meyers, Keir K. Rogers, Katelin Schutz, and Weishuang Linda Xu. Dark Matter Physics from the CMB-S4 Experiment. *arXiv e-prints*, page arXiv:2203.07064, March 2022.

[13] Albert Einstein. *Relativity: The Special and General Theory*. Routledge, 1952.

[14] Daniel J. Eisenstein, Idit Zehavi, David W. Hogg, Roman Scoccimarro, Michael R. Blanton, Robert C. Nichol, Ryan Scranton, Hee-Jong Seo, Max

Tegmark, Zheng Zheng, Scott F. Anderson, Jim Annis, Neta Bahcall, Jon Brinkmann, Scott Burles, Francisco J. Castander, Andrew Connolly, Istvan Csabai, Mamoru Doi, Masataka Fukugita, Joshua A. Frieman, Karl Glazebrook, James E. Gunn, John S. Hendry, Gregory Hennessy, Zeljko Ivezić, Stephen Kent, Gillian R. Knapp, Huan Lin, Yeong-Shang Loh, Robert H. Lupton, Bruce Margon, Timothy A. McKay, Avery Meiksin, Jeffery A. Munn, Adrian Pope, Michael W. Richmond, David Schlegel, Donald P. Schneider, Kazuhiro Shimasaku, Christopher Stoughton, Michael A. Strauss, Mark SubbaRao, Alexander S. Szalay, István Szapudi, Douglas L. Tucker, Brian Yanny, and Donald G. York. Detection of the Baryon Acoustic Peak in the Large-Scale Correlation Function of SDSS Luminous Red Galaxies. , 633(2):560–574, November 2005.

[15] C.S. Frenk and S.D.M. White. Dark matter and cosmic structure. *Annalen der Physik*, 524(9-10):507–534, 2012.

[16] Herbert Goldstein, Charles Poole, and John Safko. *Classical Mechanics*. Addison-Wesley, 3rd edition, 2002. Figure 3.1: Discretization of phase space.

[17] Dario Grasso and Hector R. Rubinstein. Magnetic fields in the early universe. *Physics Reports*, 348(3):163–266, 2001.

[18] Alan H. Guth. Inflation. In Wendy L. Freedman, editor, *Measuring and Modeling the Universe*, page 31, January 2004.

[19] E. R. Harrison. Fluctuations at the threshold of classical cosmology. *Phys. Rev. D*, 1:2726–2730, May 1970.

[20] G. Hinshaw, D. Larson, E. Komatsu, D. N. Spergel, C. L. Bennett, J. Dunkley, M. R. Nolta, M. Halpern, R. S. Hill, N. Odegard, L. Page, K. M. Smith, J. L. Weiland, B. Gold, N. Jarosik, A. Kogut, M. Limon, S. S. Meyer, G. S. Tucker, E. Wollack, and E. L. Wright. Nine-year Wilkinson Microwave Anisotropy Probe (WMAP) Observations: Cosmological Parameter Results. , 208(2):19, October 2013.

[21] Donghui Jeong and Marc Kamionkowski. Clustering fossils from the early universe. *Phys. Rev. Lett.*, 108:251301, Jun 2012.

[22] Hideo Kodama and Misao Sasaki. Cosmological perturbation theory. *Progress of Theoretical Physics Supplement*, 78:1–166, 01 1984.

[23] E. Komatsu, J. Dunkley, M. R. Nolta, C. L. Bennett, B. Gold, G. Hinshaw, N. Jarosik, D. Larson, M. Limon, L. Page, D. N. Spergel, M. Halpern, R. S.

Hill, A. Kogut, S. S. Meyer, G. S. Tucker, J. L. Weiland, E. Wollack, and E. L. Wright. Five-Year Wilkinson Microwave Anisotropy Probe Observations: Cosmological Interpretation. , 180(2):330–376, February 2009.

[24] E. Komatsu, K. M. Smith, J. Dunkley, C. L. Bennett, B. Gold, G. Hinshaw, N. Jarosik, D. Larson, M. R. Nolta, L. Page, D. N. Spergel, M. Halpern, R. S. Hill, A. Kogut, M. Limon, S. S. Meyer, N. Odegard, G. S. Tucker, J. L. Weiland, E. Wollack, and E. L. Wright. Seven-year Wilkinson Microwave Anisotropy Probe (WMAP) Observations: Cosmological Interpretation. , 192(2):18, February 2011.

[25] Stephen D. Landy and Alexander S. Szalay. Bias and Variance of Angular Correlation Functions. , 412:64, July 1993.

[26] D. Larson, J. Dunkley, G. Hinshaw, E. Komatsu, M. R. Nolta, C. L. Bennett, B. Gold, M. Halpern, R. S. Hill, N. Jarosik, A. Kogut, M. Limon, S. S. Meyer, N. Odegard, L. Page, K. M. Smith, D. N. Spergel, G. S. Tucker, J. L. Weiland, E. Wollack, and E. L. Wright. Seven-year Wilkinson Microwave Anisotropy Probe (WMAP) Observations: Power Spectra and WMAP-derived Parameters. , 192(2):16, February 2011.

[27] U. Le Verrier and J. C. Adams. The discovery of neptune. *Various Scientific Journals/Publications*, 1846. Independently predicted the existence and position of Neptune based on orbital perturbations of Uranus. Le Verrier's work was published first, but Adams' work was also crucial.

[28] Julien Lesgourgues. The Cosmic Linear Anisotropy Solving System (CLASS) I: Overview. *arXiv e-prints*, page arXiv:1104.2932, April 2011.

[29] Antony Lewis and Anthony Challinor. Camb: Code for anisotropies in the microwave background. *Astrophysics Source Code Library*, pages 02026–, 02 2011.

[30] Antony Lewis, Anthony Challinor, and Anthony Lasenby. Efficient computation of cosmic microwave background anisotropies in closed friedmann-robertson-walker models. *The Astrophysical Journal*, 538(2):473, aug 2000.

[31] Eric V. Linder. Exploring the expansion history of the universe. *Phys. Rev. Lett.*, 90:091301, Mar 2003.

[32] Knut Lundmark. Investigations of the rotational velocities of galaxies. *[Journal Name]*, page [Page Range], 1930. Studied rotational velocities of five galaxies, concluding that the required mass for stability was significantly larger than

visible matter, with mass-to-light ratios ranging from 6 to 100 times that of the solar neighborhood.

[33] M. Markevitch, A. H. Gonzalez, D. Clowe, A. Vikhlinin, W. Forman, C. Jones, S. Murray, and W. Tucker. Direct Constraints on the Dark Matter Self-Interaction Cross Section from the Merging Galaxy Cluster 1E 0657-56. , 606(2):819–824, May 2004.

[34] F. Marulli, A. Veropalumbo, and M. Moresco. CosmoBolognaLib: C++ libraries for cosmological calculations. *Astronomy and Computing*, 14:35–42, January 2016.

[35] David Matravers. Steven Weinberg: Cosmology. Oxford University Press, 2008, 544p., GBP45.00, ISBN13: 978-0-19-852682-7. *General Relativity and Gravitation*, 41(6):1455–1458, June 2009.

[36] Robert Benton Metcalf. Gravitational lensing lecture notes. Lecture slides, University of Bologna, 2024. Available at: https://virtuale.unibo.it.

[37] Seshadri Nadathur. Seeing patterns in noise: gigaparsec-scale 'structures' that do not violate homogeneity. *Monthly Notices of the Royal Astronomical Society*, 434(1):398–406, 07 2013.

[38] Dylan Nelson, Volker Springel, Annalisa Pillepich, Vicente Rodriguez-Gomez, Paul Torrey, Shy Genel, Mark Vogelsberger, Ruediger Pakmor, Federico Marinacci, Rainer Weinberger, Luke Kelley, Mark Lovell, Benedikt Diemer, and Lars Hernquist. The illustristng simulations: Public data release, 2021.

[39] Isaac Newton. *Philosophiae Naturalis Principia Mathematica*. Jussu Societatis Regiae ac Typis Josephi Streater, 1687.

[40] Bob Osano. Evolution of Cosmological Total Energy Density and Transient Periods in Cosmology. *arXiv e-prints*, page arXiv:2002.08875, February 2020.

[41] P. J. E. Peebles. *Principles of Physical Cosmology*. Princeton University Press, paperback reissue edition, September 2020. A foundational textbook on modern cosmology, originally published in 1993. This 2020 edition includes a new preface discussing developments in the field.

[42] P. J. E. Peebles and M. G. Hauser. Statistical Analysis of Catalogs of Extragalactic Objects. III. The Shane-Wirtanen and Zwicky Catalogs. , 28:19, November 1974.

[43] P. J. E. Peebles and J. T. Yu. Primeval Adiabatic Perturbation in an Expanding Universe. , 162:815, December 1970.

[44] S. Perlmutter, G. Aldering, G. Goldhaber, R. A. Knop, P. Nugent, P. G. Castro, S. Deustua, S. Fabbro, A. Goobar, D. E. Groom, I. M. Hook, A. G. Kim, M. Y. Kim, J. C. Lee, N. J. Nunes, R. Pain, C. R. Pennypacker, R. Quimby, C. Lidman, R. S. Ellis, M. Irwin, R. G. McMahon, P. Ruiz-Lapuente, N. Walton, B. Schaefer, B. J. Boyle, A. V. Filippenko, T. Matheson, A. S. Fruchter, N. Panagia, H. J. M. Newberg, W. J. Couch, and The Supernova Cosmology Project. Measurements of Ω and Λ from 42 High-Redshift Supernovae. , 517(2):565–586, June 1999.

[45] Carlos Pinheiro and F.C. Khanna. New solutions for evolution of the scale factor with a variable cosmological term. *arXiv preprint hep-th/0006174*, 2000.

[46] Planck Collaboration, P. A. R. Ade, N. Aghanim, C. Armitage-Caplan, M. Arnaud, M. Ashdown, F. Atrio-Barandela, J. Aumont, C. Baccigalupi, A. J. Banday, R. B. Barreiro, J. G. Bartlett, E. Battaner, K. Benabed, A. Benoît, A. Benoit-Lévy, J. P. Bernard, M. Bersanelli, P. Bielewicz, J. Bobin, J. J. Bock, A. Bonaldi, J. R. Bond, J. Borrill, F. R. Bouchet, M. Bridges, M. Bucher, C. Burigana, R. C. Butler, E. Calabrese, B. Cappellini, J. F. Cardoso, A. Catalano, A. Challinor, A. Chamballu, R. R. Chary, X. Chen, H. C. Chiang, L. Y. Chiang, P. R. Christensen, S. Church, D. L. Clements, S. Colombi, L. P. L. Colombo, F. Couchot, A. Coulais, B. P. Crill, A. Curto, F. Cuttaia, L. Danese, R. D. Davies, R. J. Davis, P. de Bernardis, A. de Rosa, G. de Zotti, J. Delabrouille, J. M. Delouis, F. X. Désert, C. Dickinson, J. M. Diego, K. Dolag, H. Dole, S. Donzelli, O. Doré, M. Douspis, J. Dunkley, X. Dupac, G. Efstathiou, F. Elsner, T. A. Enßlin, H. K. Eriksen, F. Finelli, O. Forni, M. Frailis, A. A. Fraisse, E. Franceschi, T. C. Gaier, S. Galeotta, S. Galli, K. Ganga, M. Giard, G. Giardino, Y. Giraud-Héraud, E. Gjerløw, J. González-Nuevo, K. M. Górski, S. Gratton, A. Gregorio, A. Gruppuso, J. E. Gudmundsson, J. Haissinski, J. Hamann, F. K. Hansen, D. Hanson, D. Harrison, S. Henrot-Versillé, C. Hernández-Monteagudo, D. Herranz, S. R. Hildebrandt, E. Hivon, M. Hobson, W. A. Holmes, A. Hornstrup, Z. Hou, W. Hovest, K. M. Huffenberger, A. H. Jaffe, T. R. Jaffe, J. Jewell, W. C. Jones, M. Juvela, E. Keihänen, R. Keskitalo, T. S. Kisner, R. Kneissl, J. Knoche, L. Knox, M. Kunz, H. Kurki-Suonio, G. Lagache, A. Lähteenmäki, J. M. Lamarre, A. Lasenby, M. Lattanzi, R. J. Laureijs, C. R. Lawrence, S. Leach, J. P. Leahy, R. Leonardi, J. León-Tavares, J. Lesgourgues, A. Lewis, M. Liguori, P. B. Lilje, M. Linden-Vørnle, M. López-Caniego, P. M. Lubin, J. F. Macías-Pérez, B. Maffei, D. Maino,

N. Mandolesi, M. Maris, D. J. Marshall, P. G. Martin, E. Martínez-González, S. Masi, M. Massardi, S. Matarrese, F. Matthai, P. Mazzotta, P. R. Meinhold, A. Melchiorri, J. B. Melin, L. Mendes, E. Menegoni, A. Mennella, M. Migliaccio, M. Millea, S. Mitra, M. A. Miville-Deschênes, A. Moneti, L. Montier, G. Morgante, D. Mortlock, A. Moss, D. Munshi, J. A. Murphy, P. Naselsky, F. Nati, P. Natoli, C. B. Netterfield, H. U. Nørgaard-Nielsen, F. Noviello, D. Novikov, I. Novikov, I. J. O'Dwyer, S. Osborne, C. A. Oxborrow, F. Paci, L. Pagano, F. Pajot, R. Paladini, D. Paoletti, B. Partridge, F. Pasian, G. Patanchon, D. Pearson, T. J. Pearson, H. V. Peiris, O. Perdereau, L. Perotto, F. Perrotta, V. Pettorino, F. Piacentini, M. Piat, E. Pierpaoli, D. Pietrobon, S. Plaszczynski, P. Platania, and E. Pointecouteau. Planck 2013 results. XVI. Cosmological parameters. , 571:A16, November 2014.

[47] Planck Collaboration, P. A. R. Ade, N. Aghanim, M. Arnaud, M. Ashdown, J. Aumont, C. Baccigalupi, A. J. Banday, R. B. Barreiro, J. G. Bartlett, N. Bartolo, E. Battaner, R. Battye, K. Benabed, A. Benoît, A. Benoit-Lévy, J. P. Bernard, M. Bersanelli, P. Bielewicz, J. J. Bock, A. Bonaldi, L. Bonavera, J. R. Bond, J. Borrill, F. R. Bouchet, F. Boulanger, M. Bucher, C. Burigana, R. C. Butler, E. Calabrese, J. F. Cardoso, A. Catalano, A. Challinor, A. Chamballu, R. R. Chary, H. C. Chiang, J. Chluba, P. R. Christensen, S. Church, D. L. Clements, S. Colombi, L. P. L. Colombo, C. Combet, A. Coulais, B. P. Crill, A. Curto, F. Cuttaia, L. Danese, R. D. Davies, R. J. Davis, P. de Bernardis, A. de Rosa, G. de Zotti, J. Delabrouille, F. X. Désert, E. Di Valentino, C. Dickinson, J. M. Diego, K. Dolag, H. Dole, S. Donzelli, O. Doré, M. Douspis, A. Ducout, J. Dunkley, X. Dupac, G. Efstathiou, F. Elsner, T. A. Enßlin, H. K. Eriksen, M. Farhang, J. Fergusson, F. Finelli, O. Forni, M. Frailis, A. A. Fraisse, E. Franceschi, A. Frejsel, S. Galeotta, S. Galli, K. Ganga, C. Gauthier, M. Gerbino, T. Ghosh, M. Giard, Y. Giraud-Héraud, E. Giusarma, E. Gjerløw, J. González-Nuevo, K. M. Górski, S. Gratton, A. Gregorio, A. Gruppuso, J. E. Gudmundsson, J. Hamann, F. K. Hansen, D. Hanson, D. L. Harrison, G. Helou, S. Henrot-Versillé, C. Hernández-Monteagudo, D. Herranz, S. R. Hildebrandt, E. Hivon, M. Hobson, W. A. Holmes, A. Hornstrup, W. Hovest, Z. Huang, K. M. Huffenberger, G. Hurier, A. H. Jaffe, T. R. Jaffe, W. C. Jones, M. Juvela, E. Keihänen, R. Keskitalo, T. S. Kisner, R. Kneissl, J. Knoche, L. Knox, M. Kunz, H. Kurki-Suonio, G. Lagache, A. Lähteenmäki, J. M. Lamarre, A. Lasenby, M. Lattanzi, C. R. Lawrence, J. P. Leahy, R. Leonardi, J. Lesgourgues, F. Levrier, A. Lewis, M. Liguori, P. B. Lilje, M. Linden-Vørnle, M. López-Caniego, P. M. Lubin, J. F. Macías-Pérez, G. Maggio, D. Maino, N. Mandolesi, A. Mangilli, A. Marchini, M. Maris, P. G. Martin, M. Martinelli, E. Martínez-

González, S. Masi, S. Matarrese, P. McGehee, P. R. Meinhold, A. Melchiorri, J. B. Melin, L. Mendes, A. Mennella, M. Migliaccio, M. Millea, S. Mitra, M. A. Miville-Deschênes, A. Moneti, L. Montier, G. Morgante, D. Mortlock, A. Moss, D. Munshi, J. A. Murphy, P. Naselsky, F. Nati, P. Natoli, C. B. Netterfield, H. U. Nørgaard-Nielsen, F. Noviello, D. Novikov, I. Novikov, C. A. Oxborrow, F. Paci, L. Pagano, F. Pajot, R. Paladini, D. Paoletti, B. Partridge, F. Pasian, G. Patanchon, T. J. Pearson, O. Perdereau, L. Perotto, F. Perrotta, V. Pettorino, F. Piacentini, M. Piat, E. Pierpaoli, D. Pietrobon, S. Plaszczynski, E. Pointecouteau, G. Polenta, L. Popa, G. W. Pratt, and G. Prézeau. Planck 2015 results. XIII. Cosmological parameters. , 594:A13, September 2016.

[48] Planck Collaboration, N. Aghanim, Y. Akrami, M. Ashdown, J. Aumont, C. Baccigalupi, M. Ballardini, A. J. Banday, R. B. Barreiro, N. Bartolo, S. Basak, R. Battye, K. Benabed, J. P. Bernard, M. Bersanelli, P. Bielewicz, J. J. Bock, J. R. Bond, J. Borrill, F. R. Bouchet, F. Boulanger, M. Bucher, C. Burigana, R. C. Butler, E. Calabrese, J. F. Cardoso, J. Carron, A. Challinor, H. C. Chiang, J. Chluba, L. P. L. Colombo, C. Combet, D. Contreras, B. P. Crill, F. Cuttaia, P. de Bernardis, G. de Zotti, J. Delabrouille, J. M. Delouis, E. Di Valentino, J. M. Diego, O. Doré, M. Douspis, A. Ducout, X. Dupac, S. Dusini, G. Efstathiou, F. Elsner, T. A. Enßlin, H. K. Eriksen, Y. Fantaye, M. Farhang, J. Fergusson, R. Fernandez-Cobos, F. Finelli, F. Forastieri, M. Frailis, A. A. Fraisse, E. Franceschi, A. Frolov, S. Galeotta, S. Galli, K. Ganga, R. T. Génova-Santos, M. Gerbino, T. Ghosh, J. González-Nuevo, K. M. Górski, S. Gratton, A. Gruppuso, J. E. Gudmundsson, J. Hamann, W. Handley, F. K. Hansen, D. Herranz, S. R. Hildebrandt, E. Hivon, Z. Huang, A. H. Jaffe, W. C. Jones, A. Karakci, E. Keihänen, R. Keskitalo, K. Kiiveri, J. Kim, T. S. Kisner, L. Knox, N. Krachmalnicoff, M. Kunz, H. Kurki-Suonio, G. Lagache, J. M. Lamarre, A. Lasenby, M. Lattanzi, C. R. Lawrence, M. Le Jeune, P. Lemos, J. Lesgourgues, F. Levrier, A. Lewis, M. Liguori, P. B. Lilje, M. Lilley, V. Lindholm, M. López-Caniego, P. M. Lubin, Y. Z. Ma, J. F. Macías-Pérez, G. Maggio, D. Maino, N. Mandolesi, A. Mangilli, A. Marcos-Caballero, M. Maris, P. G. Martin, M. Martinelli, E. Martínez-González, S. Matarrese, N. Mauri, J. D. McEwen, P. R. Meinhold, A. Melchiorri, A. Mennella, M. Migliaccio, M. Millea, S. Mitra, M. A. Miville-Deschênes, D. Molinari, L. Montier, G. Morgante, A. Moss, P. Natoli, H. U. Nørgaard-Nielsen, L. Pagano, D. Paoletti, B. Partridge, G. Patanchon, H. V. Peiris, F. Perrotta, V. Pettorino, F. Piacentini, L. Polastri, G. Polenta, J. L. Puget, J. P. Rachen, M. Reinecke, M. Remazeilles, A. Renzi, G. Rocha, C. Rosset, G. Roudier, J. A. Rubiño-Martín, B. Ruiz-Granados, L. Salvati, M. Sandri, M. Savelainen,

D. Scott, E. P. S. Shellard, C. Sirignano, G. Sirri, L. D. Spencer, R. Sunyaev, A. S. Suur-Uski, J. A. Tauber, D. Tavagnacco, M. Tenti, L. Toffolatti, M. Tomasi, T. Trombetti, L. Valenziano, J. Valiviita, B. Van Tent, L. Vibert, P. Vielva, F. Villa, N. Vittorio, B. D. Wandelt, I. K. Wehus, M. White, S. D. M. White, A. Zacchei, and A. Zonca. Planck 2018 results. VI. Cosmological parameters. , 641:A6, September 2020.

[49] Planck Collaboration, Aghanim, N., Akrami, Y., Ashdown, M., Aumont, J., Baccigalupi, C., Ballardini, M., Banday, A. J., Barreiro, R. B., Bartolo, N., Basak, S., Battye, R., Benabed, K., Bernard, J.-P., Bersanelli, M., Bielewicz, P., Bock, J. J., Bond, J. R., Borrill, J., Bouchet, F. R., Boulanger, F., Bucher, M., Burigana, C., Butler, R. C., Calabrese, E., Cardoso, J.-F., Carron, J., Challinor, A., Chiang, H. C., Chluba, J., Colombo, L. P. L., Combet, C., Contreras, D., Crill, B. P., Cuttaia, F., de Bernardis, P., de Zotti, G., Delabrouille, J., Delouis, J.-M., Di Valentino, E., Diego, J. M., Doré, O., Douspis, M., Ducout, A., Dupac, X., Dusini, S., Efstathiou, G., Elsner, F., Enßlin, T. A., Eriksen, H. K., Fantaye, Y., Farhang, M., Fergusson, J., Fernandez-Cobos, R., Finelli, F., Forastieri, F., Frailis, M., Fraisse, A. A., Franceschi, E., Frolov, A., Galeotta, S., Galli, S., Ganga, K., Génova-Santos, R. T., Gerbino, M., Ghosh, T., González-Nuevo, J., Górski, K. M., Gratton, S., Gruppuso, A., Gudmundsson, J. E., Hamann, J., Handley, W., Hansen, F. K., Herranz, D., Hildebrandt, S. R., Hivon, E., Huang, Z., Jaffe, A. H., Jones, W. C., Karakci, A., Keihänen, E., Keskitalo, R., Kiiveri, K., Kim, J., Kisner, T. S., Knox, L., Krachmalnicoff, N., Kunz, M., Kurki-Suonio, H., Lagache, G., Lamarre, J.-M., Lasenby, A., Lattanzi, M., Lawrence, C. R., Le Jeune, M., Lemos, P., Lesgourgues, J., Levrier, F., Lewis, A., Liguori, M., Lilje, P. B., Lilley, M., Lindholm, V., López-Caniego, M., Lubin, P. M., Ma, Y.-Z., Macías-Pérez, J. F., Maggio, G., Maino, D., Mandolesi, N., Mangilli, A., Marcos-Caballero, A., Maris, M., Martin, P. G., Martinelli, M., Martínez-González, E., Matarrese, S., Mauri, N., McEwen, J. D., Meinhold, P. R., Melchiorri, A., Mennella, A., Migliaccio, M., Millea, M., Mitra, S., Miville-Deschênes, M.-A., Molinari, D., Montier, L., Morgante, G., Moss, A., Natoli, P., Nørgaard-Nielsen, H. U., Pagano, L., Paoletti, D., Partridge, B., Patanchon, G., Peiris, H. V., Perrotta, F., Pettorino, V., Piacentini, F., Polastri, L., Polenta, G., Puget, J.-L., Rachen, J. P., Reinecke, M., Remazeilles, M., Renzi, A., Rocha, G., Rosset, C., Roudier, G., Rubiño-Martín, J. A., Ruiz-Granados, B., Salvati, L., Sandri, M., Savelainen, M., Scott, D., Shellard, E. P. S., Sirignano, C., Sirri, G., Spencer, L. D., Sunyaev, R., Suur-Uski, A.-S., Tauber, J. A., Tavagnacco, D., Tenti, M., Toffolatti, L., Tomasi, M., Trombetti, T., Valenziano, L., Valiviita, J., Van

Tent, B., Vibert, L., Vielva, P., Villa, F., Vittorio, N., Wandelt, B. D., Wehus, I. K., White, M., White, S. D. M., Zacchei, A., and Zonca, A. Planck 2018 results - vi. cosmological parameters. *AA*, 641:A6, 2020.

[50] Adam G. Riess, Stefano Casertano, Wenlong Yuan, Lucas M. Macri, and Dan Scolnic. Large magellanic cloud cepheid standards provide a 1 *The Astrophysical Journal*, 876(1):85, may 2019.

[51] Adam G. Riess, Alexei V. Filippenko, Peter Challis, Alejandro Clocchiatti, Alan Diercks, Peter M. Garnavich, Ron L. Gilliland, Craig J. Hogan, Saurabh Jha, Robert P. Kirshner, B. Leibundgut, M. M. Phillips, David Reiss, Brian P. Schmidt, Robert A. Schommer, R. Chris Smith, J. Spyromilio, Christopher Stubbs, Nicholas B. Suntzeff, and John Tonry. Observational evidence from supernovae for an accelerating universe and a cosmological constant. *The Astronomical Journal*, 116(3):1009, sep 1998.

[52] Adam G. Riess, Wenlong Yuan, Lucas M. Macri, Dan Scolnic, Dillon Brout, Stefano Casertano, David O. Jones, Yukei Murakami, Gagandeep S. Anand, Louise Breuval, Thomas G. Brink, Alexei V. Filippenko, Samantha Hoffmann, Saurabh W. Jha, W. D'arcy Kenworthy, John Mackenty, Benjamin E. Stahl, and WeiKang Zheng. A Comprehensive Measurement of the Local Value of the Hubble Constant with 1 km s^{-1} Mpc^{-1} Uncertainty from the Hubble Space Telescope and the SH0ES Team. , 934(1):L7, July 2022.

[53] Walter Riquelme, Santiago Avila, Juan García-Bellido, Anna Porredon, Ismael Ferrero, Kwan Chuen Chan, Rogerio Rosenfeld, Hugo Camacho, Adrian G. Adame, Aurelio Carnero Rosell, Martin Crocce, Juan De Vicente, Tim Eifler, Jack Elvin-Poole, Xiao Fang, Elisabeth Krause, Martin Rodriguez Monroy, Ashley J. Ross, Eusebio Sanchez, and Ignacio Sevilla. Primordial non-Gaussianity with angular correlation function: integral constraint and validation for DES. , 523(1):603–619, July 2023.

[54] Sergio A. Rodríguez-Torres, Chia-Hsun Chuang, Francisco Prada, Hong Guo, Anatoly Klypin, Peter Behroozi, Chang Hoon Hahn, Johan Comparat, Gustavo Yepes, Antonio D. Montero-Dorta, Joel R. Brownstein, Claudia Maraston, Cameron K. McBride, Jeremy Tinker, Stefan Gottlöber, Ginevra Favole, Yiping Shu, Francisco-Shu Kitaura, Adam Bolton, Román Scoccimarro, Lado Samushia, David Schlegel, Donald P. Schneider, and Daniel Thomas. The clustering of galaxies in the sdss-iii baryon oscillation spectroscopic survey: modelling the clustering and halo occupation distribution of boss cmass galaxies in the final data release. *Monthly Notices of the Royal Astronomical Society*, 460(2):1173–1187, 04 2016.

[55] Tommaso Ronconi and Federico Marulli. Cosmological exploitation of cosmic void statistics. New numerical tools in the CosmoBolognaLib to extract cosmological constraints from the void size function. , 607:A24, October 2017.

[56] Vera C. Rubin and W. Kent Ford Jr. Rotation of the andromeda nebula from a spectroscopic survey of emission regions. *The Astrophysical Journal*, 159:379–403, 1970. First detailed spectroscopic study of M31's rotation curve, showing flat rotation profile at large radii inconsistent with visible matter alone.

[57] Dorothea Samtleben, Suzanne Staggs, and Bruce Winstein. The Cosmic Microwave Background for Pedestrians: A Review for Particle and Nuclear Physicists. *Annual Review of Nuclear and Particle Science*, 57(1):245–283, November 2007.

[58] István Szapudi and Alexander S. Szalay. A new class of estimators for the n-point correlations. *The Astrophysical Journal*, 494(1):L41, jan 1998.

[59] Ryuichi Takahashi, Masanori Sato, Takahiro Nishimichi, Atsushi Taruya, and Masamune Oguri. Revising the Halofit Model for the Nonlinear Matter Power Spectrum. , 761(2):152, December 2012.

[60] Tommaso Treu. Strong Lensing by Galaxies. , 48:87–125, September 2010.

[61] T. S. van Albada, J. N. Bahcall, K. Begeman, and R. Sancisi. Distribution of dark matter in the spiral galaxy NGC 3198. , 295:305–313, August 1985.

[62] Ya. B. Zeldovich. A hypothesis, unifying the structure and the entropy of the universe. *Monthly Notices of the Royal Astronomical Society*, 160(1):1P–3P, 10 1972.

[63] Fritz Zwicky. Die rotverschiebung von extragalaktischen nebeln. *Helvetica Physica Acta*, 6:110–127, 1933. First application of the virial theorem to galaxy clusters, revealing a mass-to-light ratio 100 times solar neighborhood and suggesting the existence of dark matter in the Coma Cluster.

[64] Fritz Zwicky. On the masses of nebulae and of clusters of nebulae. *The Astrophysical Journal*, 86:217–246, 1937. Refined analysis of Coma Cluster dynamics, calculating a conservative mass-to-light ratio of 68 (when converted to modern Hubble constant) and explicitly discussing "dark matter".